CRESST Dark Matter Search with Cryogenic Calorimeters

Dissertation
an der Fakultät für Physik
der Ludwig-Maximilians-Universität
München

vorgelegt von

Cristina Cozzini

aus Milano, Italien

angefertigt am

Max-Planck-Institut für Physik
— Werner-Heisenberg-Institut —

München
20. Januar 2003

1. Gutachter: Prof. Dr. Walter Blum

2. Gutachter: Prof. Dr. Gerhard Graw

Tag der mündlichen Prüfung: 22. Mai 2003

Kurzfassung

Das CRESST Experiment im Gran Sasso Untergrundlabor sucht nach Dunkle Materie in Form von schwach wechselwirkenden massiven Teilchen (WIMPs) über elastische Streuung an Kernen.

Die erste Phase von CRESST benutzte 262 g Saphir Kristalle als Absorber. Ein niedriger Untergrund, eine Langzeitstabilität des kryogenen Aufbaus, sowie eine niedrige Schwelle und eine hohe Sensitivität für leichte WIMPs wurden damit erreicht. In einer sehr stabilen Messung von 1.5 kg Tagen, wurden ein Untergrund besser als 1 Ereignis/kg/keV/Tag über 20 keV und eine Schwelle von 580 eV erreicht. Saphir Detektoren sind besonders geeignet, um leichte WIMPs mit spinabhängiger Wechselwirkung zu messen. Die Ergebnisse verbessern existierende Limits in diesem Bereich.

Die zweite Phase von CRESST benutzt szintillierende Kristalle als Absorber. In einem Szintillator wird nach einer Energiedeposition neben Phononen auch Szintillationslicht erzeugt. Kernrückstöße erzeugen weniger Licht als voll ionisierende Wechselwirkungen. Die gleichzeitige Messung des Phononen- und Lichtsignals ermöglicht eine Identifizierung der Wechselwirkung. Erste Messungen mit 300g $CaWO_4$ Detektor Modulen wurden im Aufbau am Gran Sasso durchgeführt. Trotz einiger technischer Probleme war eine Charakterisierung der Detektoren möglich, die das große Potential der Ereignisdiskriminierung aufzeigt.

Introduction

The main physics goal of the CRESST (Cryogenic Rare Event Search using Superconducting Thermometers) Dark Matter experiment is the direct detection of Weakly Interactive Massive Particles (WIMPs) via their elastic scattering off the nuclei in the target absorber. WIMP-nucleus scattering event rates are expected to be less than one event per day and per kg of detector mass. It is therefore of crucial importance to suppress signals due to radioactivity which would hide or mimic (in the case of neutrons) the WIMP signal. Consequently the CRESST set-up is a low background facility operating at the Gran Sasso Underground Laboratories. Since the energy transferred to a nucleus is very small (below a few tens of keV), the energy threshold of nuclear recoils is another crucial point in a Dark Matter search. CRESST uses cryogenic detectors consisting of a dielectric target crystal with a superconducting thermometer evaporated onto one surface. An energy deposit in the absorber creates phonons which thermalize in the thermometer. When the film is held at a temperature between its normal to superconducting phase transition a small temperature change results in a relatively large change of the resistance of the film, which thus functions as a very sensitive thermometer. Using very low energy excitations, the phonons, very low energy thresholds as well as an excellent energy resolution are achievable. Furthermore practically the entire energy of nuclear recoils is converted into phonons. This leads to a quenching factor close to one for nuclear recoils, which is a clear advantage compared to all other techniques.

The subject of this thesis are the measurements performed at the Gran Sasso low background facility and the analysis of the acquired data. After an introduction to the Dark Matter problem and to the aims of direct detection experiments, the CRESST facility at the Gran Sasso Underground Laboratories is described, focusing the attention on the main sources of radioactive background. CRESST detector principles are then introduced and the physics potentials of sapphire calorimeters and $CaWO_4$ scintillating crystals are discussed. Finally before presenting the measurements and the obtained results, an overview of the analysis methods developed and applied in this work is given.

In this work a complete characterisation of CRESST Phase I detectors is accomplished. CRESST Phase I used 262 g sapphire calorimeters of $40\times40\times41$ mm^3. In a measurement lasting about three months and acquiring ~ 15 kg days of data a low radioactive background is achieved and the long term stability of operation of CRESST detectors necessary for a Dark Matter search is demonstrated. The reliability of the monitoring and the calibration procedure are investigated with a dedicated run. A 5% systematic shift to the higher energies in the extrapolation procedure of the calibration to the region of interest for Dark Matter is determined. Since it is the threshold region which mostly affects Dark Matter limits, this tendency to shift events to higher energies puts CRESST Phase I WIMP limits on the conservative side. In a very stable run of 1.51 kg

days of data, a background level below 1 count/kg/keV/day above 20 keV and a very low energy threshold of 580 eV are achieved. This run is used to set Phase I Dark Matter limits. Sapphire detectors are especially sensitive for low-mass WIMPs with spin dependent interaction and improve on existing limits in this region.

The limitation of Phase I is the residual background. Besides this the WIMP-nucleus cross section for spin independent interaction is proportional to m_N^2, with m_N the mass of the target nucleus. Therefore heavier nuclei are favoured for this interaction. The main goal of CRESST Phase II is the active discrimination of electron recoils caused by ionising radiation from nuclear recoils caused by neutrons and WIMPs and to provide improved sensitivity for high mass WIMPs. This can be achieved with the simultaneous measurement of the phonon and scintillation light using a scintillator with high mass target nuclei as an absorber. Nuclear recoils produce much less light than electron recoils and by measuring the ratio of scintillation light and phonon signal, the type of interaction can be identified. A first 6 g proof of principle detector module using $CaWO_4$ as a scintillator and a small cryogenic calorimeter to detect the emitted light, achieved a rejection efficiency for electron recoils of better than 99.7% above 15 keV. This prototype has now been scaled up to a full 300 g detector module, which will be the basic unit of the 10 kg CRESST Phase II detector.

In this work, first measurements with 300 g CRESST Phase II detector modules are performed at the Gran Sasso set up and analysed. So far due to technical problems or to an unexpected high count rate, no Dark Matter data have been taken. The acquired spectra are discussed and a preliminary characterisation of the detector behaviour is obtained. Particular attention is devoted to the investigation of the radioactive contaminants present in the measured $CaWO_4$ crystals provided by different suppliers.

Contents

Chapter 1

Introduction to the Dark Matter problem

A considerable experimental effort is in progress throughout the world to elucidate the yet unknown nature of the missing matter of the universe, the so called Dark Matter. Many candidates are currently favoured to contribute to the Dark Matter. The CRESST Dark Matter search is an experiment dedicated to directly detect one of these candidates, generically denominated Weakly Interactive Massive Particle (WIMP). This chapter introduces arguments which motivate Dark Matter searches and reviews the main candidates, focusing the attention on the motivations for the existence of WIMPs. Subsequently the underlying physics principles of the direct detection of these particles via their elastic scattering off nuclei are presented. Finally the leading direct detection experiments currently in operation and their results are discussed.

1.1 Cosmological motivation

Our present understanding of the universe is based upon the successful hot big bang theory, which is rooted in both theoretical and observational robust foundations (for an introductory review see [GB99a]). The theoretical framework is based on general relativity and the idea that the geometry of space-time is determined by the energy content of the universe. As it was later confirmed by Penzias and Wilson with the detection of the Cosmic Microwave Background, the universe at large scales is homogenous and isotropic. The metric satisfying these assumptions is the Friedmann-Robertson-Walker (FRW)metric [Oli97], which in co-moving coordinates is given by

$$ds^2 = -dt^2 + a^2(t)\left[\frac{dr^2}{(1-kr^2)} + r^2(d\theta^2 + \sin^2\theta d\phi)\right] \tag{1.1}$$

This equation is characterised by two quantities, a scale factor $a(t)$, which determines the physical size of the universe and a constant k which characterises the *spatial curvature* of the universe ($k = 0, +1, -1$ for a spatially flat, closed or open Universe). As it was observed in 1930 by E.P.Hubble, the light spectra of distant galaxies are shifted towards the red band, indicating that they are receding at a velocity proportional to their distance from us [Tur00b]. This is due to the expansion of the universe, i.e. the scale factor today is larger than when photons were emitted by the observed galaxies. In the context of the FRW metric, the expansion of the universe is characterised by the *Hubble rate of expansion* $H(t) = \dot{a}(t)/a(t)$. The present value H_0 of the Hubble parameter can be written as

$$H_0 = h \cdot 100 \text{ km s}^{-1} \text{ Mpc}^{-1} \tag{1.2}$$

where $h = 0.65 \pm 0.15$, encompassing recent observational determinations of the Hubble constant [Ber00a].

Describing the universe as a fluid, an observer comoving with the fluid would see the universe around him as isotropic. The equations of motion of a perfect fluid with isotropic pressure p and energy density ρ in an expanding universe yield the Friedmann equation

$$\left(\frac{\dot{a}}{a}\right)^2 + \frac{k}{a^2} = \frac{1}{3} 8\pi G_N \rho_{tot} \tag{1.3}$$

where G_N is Newton's gravitational constant and ρ_{tot} is the total average density of the universe, which takes into account matter, radiation and vacuum energy contributions. One might also write:

$$H^2 \equiv \left(\frac{\dot{a}}{a}\right)^2 = \frac{1}{3} 8\pi G_N \rho - \frac{k}{a^2} + \frac{\Lambda}{3} \tag{1.4}$$

where Λ is the cosmological constant and is treated here as a different form of matter. This term is associated with the vacuum energy of quantum field theory and is consistent with the Einstein equations.

Defining the *critical density*[RR93]

$$\rho_c = \frac{3H^2}{8\pi G_N} \tag{1.5}$$

such that in the absence of the cosmological constant $\rho = \rho_c$ for $k = 0$, the cosmological density parameter is then defined by

$$\Omega_{tot} \equiv \frac{\rho}{\rho_c}. \tag{1.6}$$

The Friedmann equation can then be rewritten as

$$(\Omega_{tot} - 1)H^2 = \frac{k}{a^2} \tag{1.7}$$

so that $k = 0, +1, -1$ corresponds to $\Omega_{tot} = 1, \Omega_{tot} > 1, \Omega_{tot} < 1$.

Though big bang theory nicely predicts the observed relative abundances of light elements, and the predicted age of the universe is compatible with the age of the oldest known objects, it suffers from problems concerning the initial conditions. In fact, it assumes but does not explain a finite baryon density, i.e. the matter-antimatter asymmetry, the extraordinary flatness and smoothness of the universe on very large scales and the origin of primordial density perturbation that gave rise to cosmic structures (galaxies, clusters, super-clusters) [Pri96].

The solution to these problems comes from the cosmological inflation, a period of exponential expansion in the early universe. The inflaton field has associated with it a large potential energy density, which drives the exponential expansion. This superluminal expansion implied that regions that had been in causal contact moved outside the horizon of each other explaining the large scale homogeneity and isotropy [GB99b]. In particular a generic prediction from inflation is thus that the universe is very close to flat, i.e. $k = 0$. Then at the present time $t = t_0$

$$\Omega_0 \equiv \Omega_{tot}(t_0) = 1 \tag{1.8}$$

The contribution to Ω_0 of visible matter associated with stars and hot gas in galaxies is quite small, $\approx 0.003 - 0.01$. On larger scales of galactic halos or small groups of galaxies this is in the range of $0.02 - 0.1$. On galaxy clusters scales it appears that the contribution to the density parameter may be as large as 0.3 [Oli97]. The matter content of the universe seems to be higher than the maximum amount of baryonic matter implied by big bang nucleosynthesis (BBN) [Pri96]. As will be discussed in the next paragraphs there are convincing arguments for the existence of a large amount of non-luminous, i.e. Dark Matter and its nature is one of the most outstanding questions in standard cosmology.

1.1.1 Observational evidence for Dark Matter

The presence of large amounts of non-luminous components in the Universe has been identified along the years by different means and on different scales [For02]. The most convincing observational evidence is found on the scale of galactic halos and comes from the observed flat rotation curves of galaxies. Spiral galaxies consist of a central bulge and a very thin disk which is stabilised against gravitational collapse. The observations of the Doppler shift of spectral lines can be used to obtain their rotation curves, i.e. the orbital velocity of the disk as a function of the radius [Raf97]. The observed rotation curves rise linearly from the centre outward until they reach a certain plateau value and remains flat out to the largest measured radii. Assuming Newtonian dynamics[1] this was completely unexpected

---

[1] Non-Newtonian theories have also been proposed to explain the mass discrepancy of spiral galaxies, most notably the MOdified Newtonian Dynamics (MOND) model [Mil83], [San96]. This theory postulates that Newton's laws should be modified for very small accelerations in

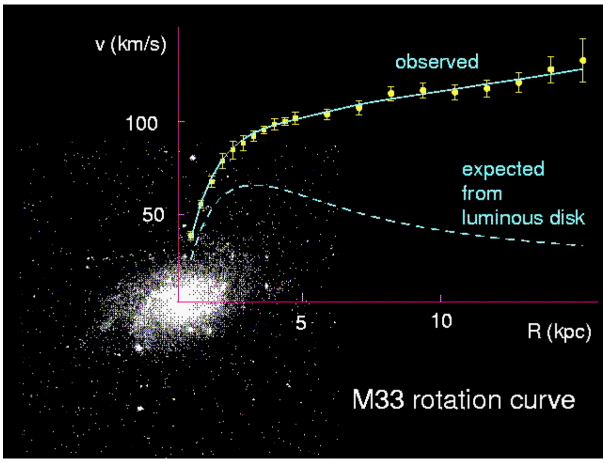

Figure 1.1: Observed rotation curve of the nearby dwarf spiral galaxy M33, superimposed on its optical image [Kha02]

since the observed surface luminosity falls off exponentially with radius

$$I(r) = I_0 e^{-r/r_D} \tag{1.9}$$

where r_D is the disk scale length. Therefore one would expect that most of the galactic mass is concentrated within a few disk lengths, such that the rotation velocity is determined by the Keplerian orbit

$$v_{rot} = (GM/r)^{1/2} \propto r^{-1/2} \tag{1.10}$$

where M is the total mass of the galaxy and G Newton's constant. No such behaviour is observed. This evidence is supported by systematic optical studies of many spiral galaxies and the most convincing observations come from radio emission of neutral hydrogen in the disk. Its 21 cm line emission can be observed to much larger galactic radii than optical tracers. An example of the measured rotation curve compared with the expected one is shown in fig. 1.1. The difference to the rotation curve which is expected from the luminous material is ascribed to the gravitational effect of Dark Matter [Raf97].

Galactic rotation curves are not the only observational indication for the existence of Dark Matter. There is mounting evidence for dark matter in galaxies and clusters of galaxies coming from X-ray observation of these objects. In fact galaxy clusters are the most powerful X-ray sources in the sky. The emission is extended over the entire cluster and thus reveals the presence of a hot plasma ($T = 10^8 - 10^9 K$) where X-rays are produced by electron bremsstrahlung[Raf97].

---

the limit $a << a_0$. For $a_0 \approx 10^{-8}$ cm s^{-2} this approach is surprisingly successful in explaining a broad range of Dark Matter phenomena related to dwarf galaxies, spiral galaxies and galaxy clusters, with the result that the need for any Dark Matter disappears. Unfortunately, MOND lacks a relativistic formulation so that it cannot be applied on cosmological scales [Raf97].

The detailed profiles of the temperature and density of the hot X-ray gas have been mapped out. By assuming hydrostatic equilibrium these measurements allow to determine the overall mass distribution in the cluster necessary to bind the gas. The result is that the mass in the hot gas is between 10% and 20% [Whi95] of the total predicted cluster mass while the visible mass contributes only 1% of the total [Oli97].

In the last few years a third piece of evidence has been gathered that also points to a very large amount of Dark Matter in clusters. Galaxy clusters gravitationally lens the light emitted by quasars and other galaxies in the background (see [Spi00]). The mapping of the mass distribution through the many arclets seen in a number of clusters indicates matter density estimates in agreement with measurements of hot gas in the clusters [Sad99].

1.1.2 Three Dark Matter problems

In terms of the density parameter, determinations of the matter contribution, both baryonic and non-baryonic have not yet converged. However there is a remarkable preference for values around 0.3 (for reviews see[Fre99],[Sch97], [Pri00], [Gro00]). As we have seen inflation theory favours $\Omega_{tot} = 1$ and indeed we now have direct evidence from high red-shift supernovae and CMB anisotropies measurements that $\Omega_{tot} = 1.02\pm^{0.06}_{0.05}$[dB02]. These results are pointing towards a flat universe whose energy is dominated by a vacuum component (cosmological constant, quintessence) together with a Dark Matter component. The current view might be summarised as shown in picture 1.2. As illustrated in the picture, be-

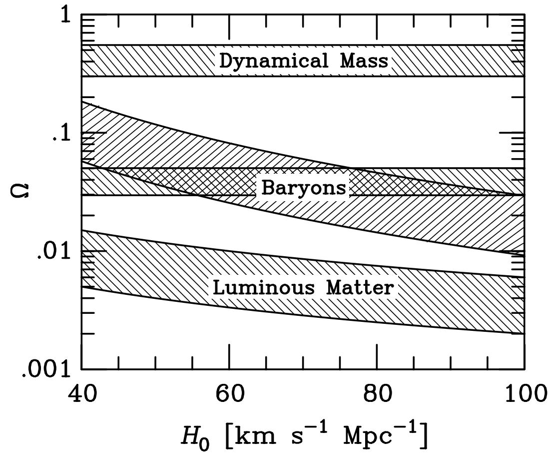

Figure 1.2: Summary of knowledge of Ω as function of the Hubble expansion parameter. The lowest band is luminous matter; the horizontal band is the galactic halo matter component, crossing the BBN determination of the density of baryons. The upper region is the estimate of dynamical mass component. Gaps in between illustrate the Dark Matter problems[GB99a].

tween the fraction predicted by BBN and the visible stars and diffuse gas there is a huge fraction which is in the form of *dark baryons.* The gap between the BBN baryon band and the mass inferred from cluster dynamics constitutes the standard Dark Matter problem, but there is still a third dark matter problem, i.e. the unfilled region which would constitute around 60% of the energy density, from dynamical mass to nowadays critical density $\Omega_0 = 1$. As mentioned above, one possibility could be that the universe is dominated by a diffuse vacuum energy, i.e. a cosmological constant. We are therefore facing the presence of *three dark components*[For02, Tur00a]:

- dark baryons
- dark non-baryonic matter
- dark energy

such that

$$\Omega_0 = \Omega_B + \Omega_{DM} + \Omega_\Lambda \tag{1.11}$$

where the baryon density Ω_B is given by the contribution of total baryonic matter including dark baryons. The total matter density Ω_M corresponds to the sum of $\Omega_B + \Omega_{DM}$. Ω_{DM} is further divided into the density of Hot Dark Matter, Ω_{HDM} and Cold Dark Matter, Ω_{CDM} depending on whether the non baryonic Dark Matter was relativistic (HDM) or non-relativistic (CDM) at the time they decoupled from thermal equilibrium after the big bang [2]. The reason for such a classification originates from the fundamentally different consequences for structure formation in the universe, like formation of superclusters and clusters of galaxies. HDM would form huge structures first (top-down approach), CDM vice versa [Ram01b]. N-body simulation of huge parts of the universe showed that structure formation cannot be understood with dominantly HDM (see [Pri97]). A consistent scenario results for a substantial CDM component and a rather negligible HDM component.

As previously mentioned, there is a strong consensus that a non-zero cosmological constant may be needed: the only known way to reconcile a low mass density with a flat universe is that an additional dark energy dominates the universe today. Its nature is unknown but it would have to resist gravitational collapse, otherwise it would have been detected; on the other hand if most of the energy of the universe resists gravitational collapse it is impossible for structure in the universe to grow. This dilemma can be solved if the hypothetical dark energy was negligible in the past and only recently became the dominant component. According to general relativity this would require that dark energy has a negative pressure [GB99a]. Recent cosmological observation find for the vacuum-energy component the value $\Omega_\Lambda = 0.71 \pm 0.11$, having used $h = 0.65 \pm 0.20$ [dB02].

---

[2] also an intermediate state called Warm Dark Matter has been proposed.

1.2 Dark Matter candidates

The inventory of Dark Matter candidates is rather huge. Whereas baryonic Dark Matter is in the form of relatively “standard” astrophysical objects, e.g. cold hydrogen clouds or compact objects such as neutron stars, brown dwarfs, or generally MAssive Compact Halo Objects (MACHOs) and even black holes, the nature of non-baryonic Dark Matter is still unknown and subject to speculations. The existence of dark (relativistic or not) non-baryonic matter and dark energy asks for extension of the standard model of fundamental interactions, since no known particle or field can explain either of these components. Candidates within the standard model are excluded, on the other hand those beyond the standard model have not yet been detected in particle physics experiments. Thus the direct or indirect detection of such particles would be a notable achievement both for particle experimental and theoretical physics.

1.2.1 Baryonic candidates

As illustrated in picture 1.2 an important fraction of the expected amount of baryonic matter is dark. Since Baryonic matter interacts with light, even if the baryons are non-luminous themselves, they would absorb light [Dol99]. This results in stringent observational upper limits on many plausible candidates [Spi00]. Thus they cannot be in the form of **hot diffuse gas** otherwise there would be a large X-ray flux; nor **cold gas** since it would absorb light and re-emit in the infrared. Baryons could otherwise have been processed in **stellar remnants**. This seems implausible since there is no trace of the normal stars from which they arise. **Neutron stars** or **black holes** in particular would typically form in a Supernova explosion and thus eject heavy elements into the galaxy, which would have been observed spectroscopically. They could be **white dwarfs**, i.e. stars not massive enough to reach the supernova phase. They are in fact end-states of stars with initial mass in the range of $0.8 - 8 M_\odot$, where $M_\odot$ is the solar mass. They are a good candidate since they form prolifically today. On the other hand they would produce too much light or too many metals and helium which has not been observed [Car94].

M-dwarfs are very dim stars in the the mass range $0.3 - 0.8 M_\odot$ but they are excluded as main candidates by background light limits: very long exposure images of the Hubble Space Telescope restrict the possible M-dwarf contribution to below 6% [Raf97]. Low mass hydrogen burning stars seem also to be excluded by source count rate and infrared measurements of other galaxy halos [Car94].

The most plausible alternatives are **brown dwarfs**, stars with mass $M \leq 0.08 M_\odot$ which never ignite hydrogen and thus shine even more dimly only from the residual energy due to gravitational contraction. The stellar mass function raises towards small masses (most stars are small) and thus one would expect significant numbers of such objects in the galaxy. Their existence has been very difficult to prove so far. However the brown dwarf scenario currently appears to be the most plausible [Car94].

All the objects mentioned above are collectively called MACHOs and may be identified through gravitational microlensing (see [Pac96]) by monitoring for example the brightness of stars in the Magellanic Clouds. The light from a distant star is deflected by the gravitational field of a massive object within the line of sight from the observer to the star, such that the star will appear brighter than in the absence of a deflector. This apparent brightening of the star due to the gravitational microlensing effect has specific signatures which allows to discriminate the presence of a MACHO against variable stars which constitute the background. Recent observation of microlensing events rule out MACHOs as the main constituent of the Dark Matter in the galaxy. The observed microlensing events may explain around 20% of the Dark Matter in the Milky Way or may be lensing objects in the Large Magellanic Cloud (LMC) [Alc00].

A final possibility are **primordial black holes**, which could have been created in the early universe even before baryons were formed and thus may be also classified as non-baryonic. Very low-mass black holes cannot form the bulk of Dark Matter as they would give rise to high energy gamma flashes which are not observed. Primordial black holes of about a solar mass could instead explain microlensing observations of MACHOs towards the LMC. The main objection against them is the lack of a plausible mechanism for forming them in the early universe. Instead very massive objects, such as an early population of stars of at least a hundred solar masses, could have rapidly formed black holes without contaminating the interstellar medium with metals. However observation of the radiation of the progenitor stars in the far infrared severely constrain this possibility. Even more massive black holes would disrupt the galactic disk [Sad99].

1.2.2 Non-Baryonic candidates

One of the most popular extensions of the standard model includes a new symmetry, called *supersymmetry*, which relates bosons, i.e. interactions mediators, with fermions, the constituents of matter. Supersymmetric (SUSY) theories introduce several possible Dark Matter candidates. SUSY particles have the same quantum numbers as their standard model partners apart from the spin and a new quantum number R, which distinguishes between “normal” matter and SUSY partners. It can be defined in terms of baryon, lepton and spin numbers as [Oli97]:

$$R = (-1)^{3B+L+2S} \tag{1.12}$$

It follows that R=1 for ordinary particles and R=-1 for SUSY particles. Assuming R-parity conservation, which is the usual minimal supersymmetric standard model (MSSM) assumption, this theory offers a variety of Dark Matter candidates such as the neutralino or sneutrino; the gravitino; the axino and others (for reviews see [Bet01] and [Spo02b]). Among these, the most interesting supersymmetric candidate is the neutralino, often referred to as the Lightest Supersymmetric Particle (LSP), which is also classified as the leading WIMP candidate.

Among the non-supersymmetric candidates the massive neutrino and the axion are the most direct possibilities. Assuming a “hot vs. cold” Dark Matter-categorisation scheme as introduced in 1.1.2, the leading HDM candidate is the light neutrino, while for CDM we find axions and WIMPs.

Neutrinos A light massive neutrino represents the simplest extension of the standard model. The recent results on the atmospheric and solar anomalies (see [Bet02]) strongly indicate that neutrinos do posses a mass: this also means that they could compose at least a fraction of the dark matter. However N-body simulations of structure formation indicate that a Universe dominated by light neutrinos (HDM) spoils the process of structure formation. In addition, there is a maximum number density of neutrinos allowed to be bound to the galaxy due to the Pauli exclusion principle. As this number must exceed the average density of the galactic Dark Matter ($\rho_{halo} = 0.3$ GeV cm^{-3} is the typical halo density), this turns into a lower limit, known as Tremaine-Gunn limit, on the required Dark Matter neutrino mass; for spiral galaxies this value is of about 20 eV [Raf97]. Therefore the hypothesis that light neutrinos could constitute the particle Dark Matter on all scales is ruled out. They could however still play a role as sub-dominant Dark Matter component in a flat CDM model; according to [Tur00a] $0.003 < \Omega_\nu < 0.15$.

Another possibility is that neutrinos have very large mass, of the order of a few GeV. To give a cosmologically interesting contribution to Ω in fact heavy neutrinos should have masses $m_\nu > 3$ GeV in order not to overclose the universe. In this mass range they would be non-relativistic and act as CDM candidates. This is however ruled out for Dirac neutrinos by accelerator and direct detection experiments up to the TeV range [Ber00a]. In the case of a Majorana neutrino its abundance in this mass range is too small to be cosmologically relevant [GB99a].

Axions Axions are very weakly interacting light bosons of an allowed mass range from 10^{-6} to 10^{-2} eV. The lower bound on the axion mass derives from cosmological arguments in order not to have an overclosed universe and the upper bound from SN1987A supernova dynamics [Raf00]. Axions arise as a solution of the CP problem in Quantum Chromo Dynamics (QCD) theory and are also a well motivated Dark Matter candidate. In fact they couple so weakly to matter that they never were in thermal equilibrium in the early universe and would behave today as a CDM candidate. There is no evidence that such particles exist, but the present laboratory and astrophysical limits on their parameters are such that, if they exist, they could well make up a significant portion of cosmic Dark Matter[Tur00a].

WIMPs The SUSY neutralino can be seen as a particular realization of a generic WIMP. These massive particles (GeV to TeV range) are assumed to carry a conserved quantum number which suppresses or forbids the decay into lighter particles. Such particles should have been copiously produced in the early universe through their weak interactions with other forms of matter and radiation. As the universe expanded and cooled, the number density of the WIMPs successively became too low for the annihilation process to keep up with the Hubble expansion rate. A relic population of WIMPs should thus exist, and it is very suggestive that the canonical weak interaction strength is just right to make the relic density fall in the right range to contribute substantially to Ω [Ber00a], [Jun96].

Neutralinos are spin 1/2 Majorana particles which are linear combinations of the SUSY partners of the photon, Z^0 and Higgs bosons, e.g. the photino, Z-ino and Higgsino [Jun96]. From accelerator searches lower limits on neutralino mass have been obtained, however these estimates are model dependent. Though for example LEP searches place limits $m_\chi > 17$ GeV [Ell97], there indeed exist parameter space in the MSSM where the neutralino mass may be as low as 2 GeV [Gab96]. It is therefore essential to have experiments which are sensitive enough to confirm or exclude the existence of neutralinos in this mass range.

Phase I of the CRESST Dark Matter Search is unique in being able to probe the low mass WIMP range due to its low energy threshold detectors, as will be discussed in detail in this thesis.

1.3 The direct detection of Dark Matter

The experiments to reveal the nature and abundance of particle dark matter can be divided in two conceptually different approaches: direct and indirect detection. The physics underlying the direct detection technique is the *elastic scattering* of a WIMP with a nucleus of the detector placed on the Earth and may be revealed by measuring the phonon, ionisation or scintillation signal [Ram99]. Else one may indirectly detect the products of annihilation of Dark Matter particles such as gamma rays, antiprotons or positron, in the galactic halo or in the Earth or Sun, in which case neutrinos could give an indirect signal [Ber00a].

The two quantities which are crucial to both direct and indirect detection of Dark Matter are the local Dark Matter density, ρ_0 and the velocity dispersion of Dark Matter particles $\bar{v} = \langle v^2 \rangle^{1/2}$. Detection rates which depend on annihilation processes occurring in the galactic halo are strongly affected by uncertainties in the matter distribution. Direct detection instead relies on local properties like the local Dark Matter density. Also the way Dark Matter particles behave in velocity space affects mostly direct detection, which relies on the energy transferred from the Dark Matter particle to the detector[For02].

In order for the galaxies to reach a constant outer rotation curve, the density profile of the Dark Matter halo must fall approximately proportional to r^{-2} in the relevant radius range. Such a profile resembles the density structure of an isothermal, self-gravitating system of particles which is characterised by a constant velocity dispersion. Dark Matter halos are therefore often approximated by the so-called *modified isothermal sphere* model. The radial density profile is taken to be:

$$\rho(r) = \frac{\rho_0}{1 + r^2/r_c^2} \tag{1.13}$$

where r_c is the core radius and ρ_0 is the central Dark Matter density [Bur95]. When tested by comparison with the Dark Matter distribution as derived from the measured rotation curve of dwarf spiral galaxies, the modified isothermal profile fits only the inner regions but rises too fast at large radii. The observed universal mass profiles are well represented by the following phenomenological density distribution:

$$\rho_{DM}(r) = \frac{\rho_0 r^3}{(r + r_0)(r^2 + r_0^2)} \tag{1.14}$$

where ρ_0 is the central density and r_0 a core radius [Bur95]. The very existence of a "core", i.e. a central region where the density is approximately constant, has been challenged by recent high resolution N-body simulation [Nav96]. The canonical values for the local Dark Matter density is $\rho_0 = 0.3$ GeV cm^{-3} though there is considerable uncertainty and model dependence in this estimate [Jun96]. For neutralino WIMPs as a dominant component of the halo this translates to about 3000 LSPs with mass $m_\chi = 100$ GeV per cubic meter [Ros00]. Assuming a typical galactic velocity of neutralinos of v/c$\approx 10^{-3}$ the flux of particles with this mass at the location of a detector at the Earth is roughly 10^9 m^{-2} s^{-1} [Ber00a].

The form of the halo distribution function presumably depends on the details of the collapse process which formed the galaxy. General dynamical arguments suggest that the WIMP velocities were thermalized by fluctuation in the gravitational collapse, a process known as *violent relaxation*. On this basis it can be assumed that WIMPs have an approximately Maxwell-Boltzmann speed distribution in the galactic rest frame (the halo is assumed to be non-rotating):

$$f(v)dv = 4\pi n_W \left(\frac{3}{2\pi\bar{v}^2}\right)^{3/2} v^2 exp\left(-\frac{3v^2}{2\bar{v}^2}\right) dv \tag{1.15}$$

where n_W is the local number density of WIMPs of mass m_W, defined as $n_W = \rho_0/m_W$[Fre88]. The velocity dispersion $\bar{v}$ is directly related to the asymptotic flat rotational velocity as $\bar{v} = \sqrt{3/2}v_\infty$. In our Galaxy, the rotational velocity appears to be already flat at the local position and therefore we set $v_\infty = v_\odot$. The experimental determination of the local rotational velocities $v_\odot = 230 \pm 50$ km s^{-1} (90% C.L.). The distribution is also truncated by an escape velocity $v_{esc} = 450 \div 650$ km s^{-1} (90% C.L.) [Bot97]. The canonical values for velocity dispersion is $\bar{v} = 270$ km s^{-1} [Jun96].

1.3.1 Theoretical event rates

The most important direct detection process is elastic scattering on nuclei, and the recoil energy can be measured by means of various experimental techniques with different nuclear species. As a first approach one may consider a stationary detector with infinite resolving power, an equal detection efficiency for nuclear recoils and electron recoils and consisting of a single type of nuclei. As introduced above, the rate in a detector depends on the density ρ_0 of WIMPs near the Earth and the velocity distribution of WIMPs near the Earth. The event rate per kilogram of detector mass, R, is qualitatively [Jun96]

$$R \approx \frac{n_W \sigma \langle v \rangle}{m_N} \tag{1.16}$$

where σ is the elastic scattering cross section, $\langle v \rangle$ is the average speed of the WIMP relative to the target and m_N is the target nuclei detector mass in kg. As will be shown in the next paragraphs, to derive the exact expression for the event rate one should take into account the WIMP velocity distribution in the halo and that the detector is located on Earth, in orbit around the Sun with the Solar system moving in the galaxy. Furthermore different target masses as well as instrumental resolution and threshold effects have to be considered. Besides these, the detection efficiency for nuclear recoils might be different from that for the background electron recoils and there is a form factor correction dependent on nuclear radius and recoil energy which also differs for spin-dependent and spin-independent (scalar) interactions [Lew96].

1.3.2 Nuclear form factors

The form factor parametrises the loss of coherence due to the finite size of the nucleus for the WIMP-nucleus interaction as the WIMP-energy increases. Both spin dependent (axial) and spin-independent (scalar) cross sections are modified at high momentum transfer q by form factors that reflect the spatial distribution of nucleons inside the nucleus. When the momentum transfer to the nucleus $q = \sqrt{2 m_N E_r}$ is such that the de-Broglie wavelength $\lambda = h/q$ is smaller that the size of the nucleus, the effective scattering cross-section decreases with increasing momentum.

While spin-independent form factors are simply related to nuclear densities, spin dependent cross sections reflect delicate aspects of nucleonic and nuclear structure [Eng92]. Spin-independent scattering is a coherent process and an analytic expression for the form factor can be derived. At non-zero momentum transfer the form factor is defined as as the Fourier transform of the nuclear matter distribution, which in this case has a well defined form. In contrast, in the spin dependent case the form factor calculations require significant effort since nuclear properties have to be calculated for each nucleus with an appropriate nuclear model. For discussion and explicit calculations, see [Jun96, Eng91].

The effective cross-section, either spin-dependent or spin-independent, is thus given by:

$$\sigma = \sigma_0 F^2(E_r) \tag{1.17}$$

Separation into the term σ_0 (zero momentum transfer cross section) containing all dependencies on the specific interaction and $F^2(E_r)$, dependent only on momentum transfer, is convenient in allowing model-independent results. However, in the case of spin dependent interactions, this correspond to considering contributions only from the unpaired nucleon (single particle model) or nucleons of the same type as the unpaired nucleon (odd group model) and has substantial errors for large masses [Lew96, Tov00].

The cross section at zero momentum transfer for the spin-independent WIMP-nucleus interaction is related to the mass of the target nucleus by the relationship

$$\sigma_{0si} \approx \mu^2 m_N^2 \tag{1.18}$$

indicating that, apart from the form factor, the interaction rate is higher for heavier nuclei.

In the case of spin-dependent interactions instead it is given by:

$$\sigma_{0sd} \approx \mu^2 C \lambda^2 J(J+1) \tag{1.19}$$

where $\lambda^2 J(J+1)$ is the nuclear spin factor and is usually estimated using the "odd-group" model. C is the squared hadronic matrix element for the odd nucleon in the nucleus [Jun96].

It is important to note that it is only for coherently interacting WIMPs that very massive nuclei are desirable since the interaction cross section scales as the nucleus mass squared. However in this case coherence loss must be considered. For particles with only spin-dependent interactions on the other hand, the most desirable detector nuclei are those that maximise energy loss, i.e. which match nuclear and WIMP masses. In this case relatively small nuclear masses are desirable [Fre88].

For the scattering of light WIMPs on light nuclei, such as can be expected with the CRESST sapphire detectors, the nuclear recoil energies are low enough that the form factor $F^2(E_r) \approx 1$.

1.3.3 Nuclear Recoil Quenching Factor

The detector sensitivity for a nuclear recoil event is a crucial point in a Dark Matter experiment. When a particle interaction occurs in an absorber the energy deposited is shared between nuclear recoils and electron recoils. Ionising particles such as α, β and γ radiation and heavy charged nuclei interact predominantly with atomic electrons, while neutrons and WIMPs interact predominantly via the nuclear channel.

The quenching factor is defined as the ratio of the signal amplitude from a nuclear recoil and from an electron recoil of the same energy. Conventional detectors that measure the ionisation or the excitation of the electrons inside the detector material such as Si, Ge and NaI detectors, have quenching factors much lower than unity [Ale97]. On the contrary the quenching factor is expected to be one for detectors which measure a thermal signal. In fact these detectors measure the heat released by the particle which is in principle independent of the interaction mechanism. However instances such as energy trapping or crystal defects could in principle deteriorate this value.

The nuclear recoil detection efficiency for cryogenic particle detectors has been measured using TeO_2 crystals (see[Ale97]) confirming a quenching factor compatible with unity.

1.3.4 Energy spectrum

As WIMP velocities are non-relativistic, the energy deposited in a detector, E_r, due to WIMP nucleus elastic scattering is:

$$E_r = \frac{m_\chi^2 m_N}{(m_\chi + m_N)^2} v^2 (1 - cos\theta) \tag{1.20}$$

where θ is the scattering angle in the centre of mass frame.

The differential rate for elastic WIMP-nucleus scattering is given by the equation [Jun96]:

$$\frac{dR}{dE_r} = N_T \frac{\rho_0 \sigma_0}{2 m_W \mu^2} F^2(E_r) \int_{v_{min}}^{v_{esc}} \frac{f_1(v)}{v} dv; \qquad v_{min} = \sqrt{\frac{E_r m_N}{2\mu^2}} \tag{1.21}$$

where N_T represents the number of targets, m_N the target nucleus mass, $\mu = (m_W m_N)/(m_W + m_N)$ the reduced mass, E_r the recoil Energy transferred to the nucleus defined above and $F(E_r)$ is the form factor defined in paragraph 1.3.2. The term $f_1(v)$is the velocity distribution of WIMPs assumed to be Maxwellian in the galactic rest frame as defined in 1.15. Evaluated in the Earth's rest frame (see [Fre88, Jun96]), this results in [Don98]

$$f_1(\vec{v}, \vec{v_E}) = \frac{1}{k} exp \left(- \frac{(\vec{v} + \vec{v_E})^2}{\vec{v}^2} \right) \tag{1.22}$$

where k is the normalisation factor and v_E the Earth velocity vector.

For simplicity assuming a pure Maxwellian distribution (avoiding motion of Earth and Sun), integrating over all detectable recoil energies (between E_{thr}, the Energy threshold of the detector, and $E_{max} = 2\mu^2 v^2/m_N$), for light WIMPs where $F(E_r) \sim 1$ the total event rate per kilogram is:

$$R = N_T \frac{\rho_0 \sigma_0}{m_W M_N} \frac{2}{\sqrt{\pi}} v_0 exp\left(\frac{-E_{thr} m_N}{2\mu^2 v_0^2}\right) \tag{1.23}$$

where $v_0 \approx 220$ km s^{-1} is the circular speed of the sun around the galactic centre.

Summarising, the main experimental requirements for direct detection techniques are [Ram99]:

- Energy threshold: as low as possible due to the quasi exponential decreasing signal as function of recoil energy. The relevant energy region is generally below 100 keV.
- Target mass: as high as possible due to the low cross section for WIMP-nucleus elastic scattering.
- Background: as low as possible, the aim being to progressively reduce or reject background events to allow a spectrum of rare nuclear recoil events to be observed.

As we shall see in Chap. 4 cryogenic detectors of the type used in the CRESST Dark Matter Search can achieve very low energy thresholds down to 500 eV making them ideal for WIMP detection.

1.3.5 Signatures for WIMP direct detection

As previously mentioned, standard assumptions for WIMP Dark Matter searches are that WIMPs are gravitationally bound to the galaxy, forming a spherical isothermal halo model with a local density of 0.3 GeV/cm^3 and a Maxwellian velocity distribution with a mean value of 232 km/s truncated at the escape velocity from the galaxy of 650 km/s.

There are three types of WIMP signatures: the detector material dependence, the annual modulation and the diurnal modulation. WIMP rates and spectral shapes depend on the target material, therefore experiments which use different target materials in the same set-up could identify a WIMP signal by comparing rates and spectra. However this would require a signal to background ratio larger than one. Due to the very low WIMP event rate only experiments with large detector masses, low energy threshold and nuclear recoil discrimination capability might in principle reach such a sensitivity. This is for example a physics potential for CRESST Phase II. Up to now no experiment was able to exploit such a signature.

With adequate event rate, i.e. with sufficiently low background and large detector masses[3], a positive evidence for a WIMP signal could be obtained from

---

[3] For an estimation of what can be defined a sufficient mass for different types of detectors, see reference [Ram02a].

the small annual modulation of the spectrum. This arises from the kinematics of the earth within the usually assumed non-rotating halo model [4]. As shown in fig. 1.3, the sun orbits the galaxy with a velocity of about 220 km s^{-1} (including the motion relative to the local standard of rest gives the indicated 232 km s^{-1}) and the Earth is orbiting the sun with a velocity of about 30 km s^{-1} with the orbital plane inclined at 60° respect to the galactic plane [Smi90]. Therefore the Earth sees a larger WIMP flux in June when its rotational velocity adds to the velocity of the sun, and by a smaller flux in December when the two velocities are in opposite directions. An annual modulation of the count rate by a few percent would then yeld a positive signature. Therefore, with this particular halo model assumption, the following features are required in order to verify the presence of a WIMP induced modulation [Ber00b]:

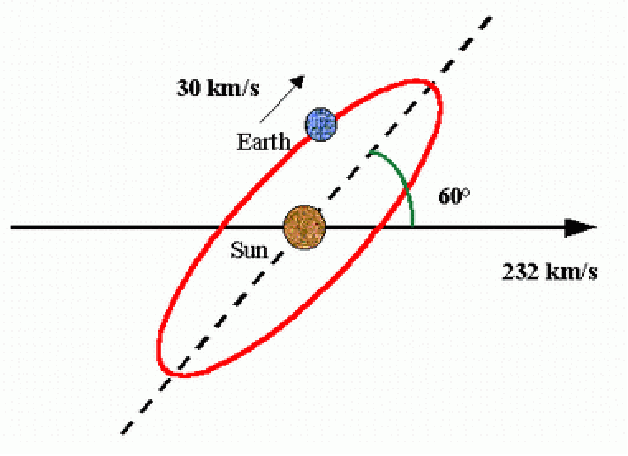

Figure 1.3: Kinematics of the Earth within the non-rotating WIMP halo

- the modulation follows a cosine-like behaviour;
- it has a period of one year;
- the maxima occur at $t_0 \sim$ 2 June ($\sim$152.5th day of the year);
- the measured modulated amplitude is $\sim 7\%$ in the region of maximal sensitivity.

Finally the most convincing evidence would arise from the directional asymmetry of the recoiling nuclei, given a direction sensitive detector. In this case the directionality is additionally modulated diurnally by the earth rotation about its axis. The diurnal modulation is much stronger than the annual modulation and in case of a positive signal would constitute the most sensitive proof.

---

[4] For the effect of different types of halo models on the expected WIMP signal, see[Kam98]

1.3.6 WIMP exclusion limits

Constraints on the WIMP interaction cross section are set by calculating the upper limit of the theoretical event rate, which is incompatible with the observed event rate. Any set of parameters which produces a theoretical event rate exceeding this limit is then excluded to a given confidence level (typically 90% C.L.). In experiments without background subtraction such as CRESST Phase I , the expected signal is on top of a background spectrum of unknown shape and no information can be extracted from the shape itself of the observed energy spectrum. However any set of WIMP parameters (mass and cross-sections) which would produce more events than observed at some confidence level, can be excluded at that confidence level independently of any assumption on the background shape.

So far there is no standard procedure in the literature for extracting upper limits. As a first step the theoretical WIMP recoil spectrum must be convoluted with experimental resolution and then for any given WIMP mass compared with the observed spectrum applying criteria which would produce 90% exclusion limits. Several groups use the so called *optimal interval method*, see [Bau99]. Given a WIMP mass this method selects the energy bins giving the most stringent limit on the cross section. It has been shown that this method actually produces exclusion limits which have a lower degree of confidence than 90% and hence are erroneously tight [Gre02, Ang02b].

For CRESST Phase I results, two other different methods have been developed to extract upper limits, the fit method and the Monte Carlo method [Ang02b]. In the fit method the spectrum is fitted with an empirical function B using a maximum likelihood method with Poissonian statistics in each bin. Without a WIMP signal the best fit B_0 simply describes the background. With a WIMP signal S as calculated for fixed WIMP masses and a free cross section parameter, the background function is redefined to $B^1 = B_0 - S$. In case S>B, then $B^1 = 0$. In other words, B^1 is not allowed to have negative values, avoiding in any sense a background subtraction. The likelihood function calculated from the background function is then used to set a 90% C.L. limit. For σ_0 such that $S < B_0$ in each bin, the likelihood is unchanged. For increasing σ_0, when $S > B_0$ in some energy bin, then B^1 is limited at 0 and the likelihood L starts to decrease. The σ_0 excluded at 90% C.L. is obtained when $\ln L = \ln L_0 - 1.28^2/2$ is reached, where L_0 is the maximum likelihood of the best fit B_0. The Monte Carlo (MC) method starts from the same empirical fit function and uses the fit function B_0 as the Poisson mean in each bin to generate a large number of synthetic MC spectra. The functional form B is then fit to each synthetic data set and the σ_0 is found for which $S = B$ in one energy bin for that data set. The 90 % C.L. upper limit is that σ_0 which is above 90% of the values determined from all synthetic data sets.

The results of these three methods are shown in picture 1.4. Other methods are suggested in reference [Gre02]. These correct for the bias of the optimal bin method and have been shown to give consistent result with those obtained with the MC method[Ram01a].

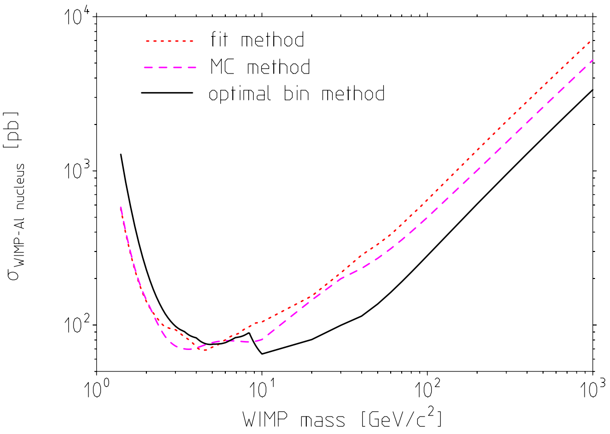

Figure 1.4: Comparison of the different methods to extract exclusion limits at 90% C.L. for the WIMP$-^{27}$Al spin-dependent σ_0 limit [Ang02b].

1.4 Current Direct Detection Experiments

There are different types of detection techniques, ranging from the rather well known germanium semiconductors technique, scintillator detectors at room temperature and cryogenic detectors to the superheated Freon droplet detection technique or direction sensitive projection chambers. For extended reviews see [Mor01, Loi02, Ram02b].

Classical Germanium detectors Semiconductor detectors are characterised by an excellent energy resolution, a well-proven technology and a very high purity level. On the other hand the restricted choice of detector materials (Ge and Si), the microphonic noise at low energies, the lack of discrimination capability between electron and nuclear recoils and the high costs for large detector masses are intrinsic limitations of such a technique.

The **Heidelberg-Moscow** Experiment was originally designed to search for neutrinoless double-beta decay using classical Ge detectors. Due to the available high purity of Ge and a substantial work on low background conditions they achieved the lowest background (0.05 counts/kg/keV/day above 15 keV) of any Dark Matter search without background rejection. Presently the collaboration operates a dedicated Dark Matter experiment in the Gran Sasso laboratories in a well-type set-up (**HDMS**) using a 200 g p-type Ge detector surrounded by a 2 kg veto detector. Photons or neutrons interacting in the inner detector have a considerable probability to generate a coincident signal in the veto detector and thus be discarded. In the **GENIUS** project proposed by the same group 100 kg of un-encapsulated Ge crystals shall be surrounded by a large volume of highest purity liquid nitrogen to assure a radio-pure surrounding as well as a shielding. A test facility has recently been approved.

The **IGEX** detector is situated in the Cafranc tunnel in the Pyrenees and consists of a 2 kg Ge crystal enriched to 86% in ^{76}Ge. They have a lower energy threshold than the above experiments and reached the highest sensitivity ($\sigma_{\chi-n} \sim 7\times10^{-6}$pb for coherent interaction) of all experiments using classical Ge detectors (see fig. 1.6).

Classical Scintillators Several WIMP searches make use of scintillation detectors, mostly NaI(Tl) or liquid Xenon detectors. In spite of their poorer energy resolution and intrinsic radio-purity if compared to Ge detectors, they have the advantage of a wide choice of target materials, well established detection technique, low costs and hence the possibility of using large detector masses. Furthermore, their main advantage for WIMP searches is their intrinsic pulse shape discrimination capability to distinguish nuclear from electron recoil.

The **DAMA** collaboration is operating ~100 kg of NaI crystals each viewed by two photomultiplier tubes (PMTs) in the Gran Sasso underground laboratories and has collected within four years ~ 58000 kg·days of statistics. The non-zero spin of the sodium nucleus makes these detectors also sensitive to axial coupling. The DAMA group observed an annual modulation in their count rate (see fig.1.5) which they claim to be compatible in phase and amplitude with a signal from WIMPs of 52^{+10}_{-8} GeV mass and WIMP-nucleon cross section of $(7.2^{+0.4}_{-0.9})\times10^{-6}$ pb [Ber00b]

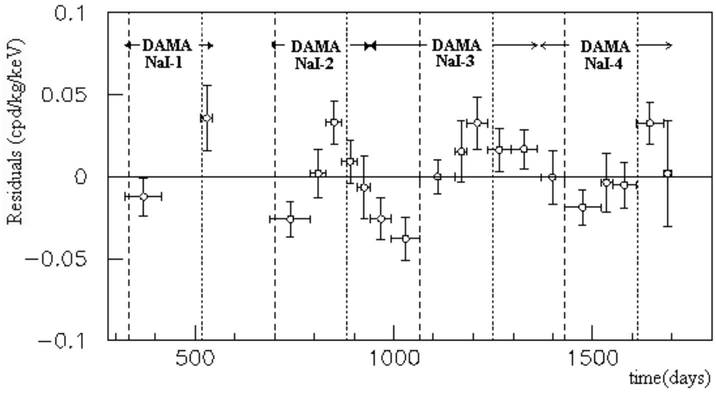

Figure 1.5: Annual modulation of the count rate as observed by the DAMA collaboration over a period of four years.

The **UKDMC** group is using liquid xenon scintillator detectors. The **ZEPLIN-I** experimental set-up consists of a 4 kg prototype mounted in the Boulby mine in the UK. The scintillator is viewed by three PMTs which allow, by triple coincidence, to reject spurious events in or near the PMTs. A liquid scintillator Compton veto and a lead shield complete the set-up. The ZEPLIN group is presently developing an even more efficient background rejection technique that allows discrimination on an event-by-event basis. The technique exploits ionisation occurring in the liquid Xe in addition to scintillation. In this two-phase liquid and gas detector ionisation electrons are extracted from the liquid into the gas phase, where they are accelerated and generate electroluminescence that is registered as a delayed signal by the same PMTs that are viewing the liquid Xe. Since nuclear recoils generate much less ionisation than electron recoils the secondary signal is much smaller for nuclear than for electron recoils. A one ton project is hoped to cover a large fraction of the WIMP parameter space [Spo02a].

The **ELEGANT** V and VI experiments based in the Japanese Oto Cosmo Observatory are employing, besides a 730 kg NaI crystal array, 7.2 kg of CaF_2 scintillator. The ^{19}F nucleus offers a non-zero spin and a very advantageous spin factor which makes it particularly sensitive for axial coupling. Unfortunately both materials in these experiments are not of the highest purity.

Cryogenic detectors, which will be discussed in detail in the following chapters, are generally operated at temperatures from 10 mK to 100 mK. They are using phonons as principal excitations and detect them as temperature pulses. Phonons offer two advantages as compared to ionisation and scintillation: first, the entire energy of nuclear recoils is transformed into phonons, whereas ionisation and scintillating detectors have relatively high quenching factors. Second, the excitation energy of phonons, typically meV, is roughly three orders of magnitude lower than that of electron-hole pairs or scintillation photons. These two advantages result in a considerably lower energy threshold as well as a high energy resolution. Combining phonon detection with either ionisation or scintillation measurements allows very efficient event-by-event background rejection. Another advantage, in common with scintillators, is the flexibility in the choice of the target material.

ROSEBUD, up to now using low threshold sapphire and Ge cryogenic detectors, are now studying phonon-scintillation detectors and have obtained interesting results with ~ 50 g $CaWO_4$ and BGO crystals.

The **CDMS** collaboration operates Ge and Si cryogenic detectors with both superconducting thin films and NTD Ge thermistors as temperature sensors [Abr02]. Additionally, ionisation charges are drifted to thin film electrodes on the crystal surfaces and provide efficient electron recoil discrimination. With one 100 g Si and four 165 g Ge detectors run in 1998 and 1999 CDMS could investigate a large part of the 3σ allowed region of the DAMA evidence, excluding the DAMA most likely parameter set at $> 99.9\,\%$ CL [Abr02]. The experiment is situated in a shallow underground site in Stanford and suffers from muon induced neutron events. Therefore a neutron subtraction is required to derive the stringent Dark Matter limits. Within the year 2002 the experiment plans to move to the Soudan deep underground lab.

The **EDELWEISS** collaboration is using 320 g Ge detectors similar to those of CDMS, with NTD Ge phonon sensors and aluminium thin film charge collection electrodes, split on one crystal surface into a central electrode defining a fiducial volume and an outer ring electrode to reject events due to radioactive impurities near the detector circumference. The detectors are operated at ~ 20 mK in the Modane underground lab in the French-Italian alps. In data taking runs in the years 2000 and 2002 (12.1 kg·days fiducial) no nuclear recoil events were observed in the relevant energy range. A Dark Matter limit has been derived that excludes the DAMA central value at 99.94 % CL [Ben02]. At present this is the most sensitive limit of all Dark Matter searches for WIMP masses above 35 GeV. For an upgrade of the experiment to ~ 30 kg a large volume reversed dilution refrigerator has been developed. The present limits of both the CDMS and EDELWEISS experiments are shown in fig. 1.6, together with the IGEX Ge diode limit and the allowed region of the DAMA WIMP candidate.

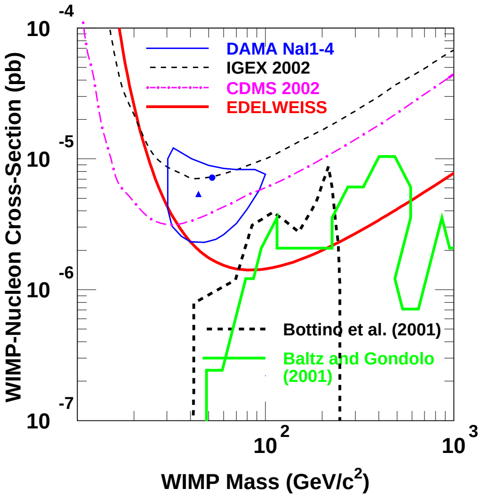

Figure 1.6: Exclusion limits of some of the presently most sensitive direct WIMP searches. The region above each curve in the parameter space WIMP-nucleon cross section vs. WIMP mass has been excluded by the respective experiments. The closed contour corresponds to the $3\,\sigma$ allowed region of the DAMA experiment, its central value is represented by the full circle. The regions in the lower half delimited by the bold lines represent the parameter space predicted by different SuSy model calculations [Ben02].

CRESST, CDMS and EDELWEISS expect, after upgrading their respective experiments to $\sim 10-30$ kg detector mass and improving background rejection efficiencies, very similar sensitivities of about 10^{-8} pb in the relevant WIMP mass range, thus testing a significant part of MSSM models.

Other techniques The **PICASSO** and **SIMPLE** experiments are testing superheated Freon (CF_2Cl_2) droplets immersed in a gel matrix as target material. A nuclear recoil inside a droplet above a certain threshold energy evaporates the droplet. The formation of a bubble can be registered as an acoustic pulse by a piezoelectric transducer. The threshold energy can be adjusted by varying the temperature. The advantage of this concept is, besides relative simplicity and cost efficiency, that the superheated droplets are insensitive to electron recoils due to their much lower dE/dx (energy dissipation per track length) such that the radioactive background problem essentially does not exist for these detectors, with the exception of alpha contaminants and nuclear fission.

The **DRIFT-I** detector in the Boulby mine consists of a low pressure CS_2 time projection chamber that allows imaging of recoil tracks [Spo02a]. Beside a low sensitivity to electron recoils, the track length provides a means for discrimination. A problem is the low target density ($\sim 180\,\mathrm{g}$ in the $1\,\mathrm{m}^3$ DRIFT-I detector), i.e. the large volume required for a large-scale experiment. However, the convincing evidence that would arise from the observation of a modulation of recoil directions as expected from WIMP interactions seems attractive enough to pursue this development.

Chapter 2

The CRESST dark matter search

The aim of CRESST is the search for WIMP Dark Matter particles via their elastic scattering off the target nuclei in an absorber, sapphire crystals for CRESST Phase I and $CaWO_4$ scintillating crystals for CRESST Phase II. As discussed in the previous chapter the energy deposited in a detector by a WIMP-nucleus elastic scattering is very small and the relevant energy range is below a few tens of keV. Furthermore due to the small WIMP-nucleus cross section event rates are expected to be less than one event per day and per kg of detector mass. It is therefore of crucial importance to suppress signals due to radioactivity which would hide (as e.g. gamma, beta and alpha interactions), or mimic (in the case of neutrons) the WIMP signals.

In this chapter the main sources of radioactive background and a characterisation of the CRESST set-up in the Gran Sasso underground laboratories are presented.

2.1 Sources of background radiation

Rare event searches are currently limited by radioactive background signals due to cosmic rays, natural or induced radioactivity. Furthermore in very low-background experiments the materials used for constructing the detectors might themselves be a source of background. Therefore careful selection of radio-pure materials for the experiment set-up is mandatory. The shielding against cosmic radiation is achieved by installing the set-up in a deep underground site and against environmental radioactivity by means of high Z and high density materials (usually lead) and very radio-pure materials like copper. For WIMP searches, particular attention must be devoted to neutrons. Since they scatter off nuclei they cannot be distinguished from a WIMP signal. Therefore a neutron moderator is finally needed to complete the set-up. Here the main sources of radioactive background are mentioned, for a complete review see [Heu95].

2.1.1 Cosmic radiation

Primary cosmic radiation is mainly composed of a hadronic component (protons 92.4%; α particles 6.7% and heavier nuclei $< 1\%$) and a leptonic component of electrons and neutrinos. Hadrons have a very high interaction probability with atmospheric atoms (thickness $\sim$ 1000 g$\cdot$cm^{-2}). For example protons have an interaction length of about 90 g$\cdot$ cm^{-2}, while α particles and heavier nuclei collide after an even smaller thickness [Gai90]. This translates into a very fast degradation of primary radiation and only a very small fraction will reach the Earth surface.

Secondary cosmic radiation at sea level is composed of about 70% muons, $\sim$ 30% electrons and of $< 1\%$ of protons and neutrons. Muons are the most penetrating component and they contribute mostly to produce radioactive background in low-counting facilities. They loose energy by ionisation and can contribute to the detector background in different ways: by depositing energy in traversing the detector itself; by producing energetic electrons which induce secondary electrons and gamma radiation; by interacting with materials surrounding the detectors followed by X, γ and neutrons emission. Furthermore neutrons produced by muons through spallation processes in turn produce radioactive nuclei.

Cosmogenic radionuclides are produced by the interaction of cosmic rays with atoms in the atmosphere through spallation processes or neutron capture. The most relevant radionuclides to environmental radioactivity are: ^{3}H, ^{14}C, ^{7}Be and ^{22}Na.

2.1.2 Environmental Radioactivity

Besides cosmogenic radionuclides, the main contribution to environmental radioactivity is due to primordial radionuclides and to radioisotopes man-made in the last decades.

Primordial radionuclides are survivor isotopes of the original synthesis of matter in the solar system.The most important ones are ^{40}K, ^{87}Rb and radionuclides belonging to natural radioactive chains [Eis87]. **Potassium** is present in nature in three different isotopes of which only ^{40}K is β unstable with a half-life of 1.3×10^{9} y. Despite its low isotopic abundance (0.012%) it is one of the most relevant contributors to natural radioactivity. Potassium is in fact a very common element to be found in rocks and soil. It is furthermore solvable in water and it is a fundamental element for biological equilibrium of plants and animals. **Rubidium** is present in nature as ^{85}Rb and ^{87}Rb, of which only the second is radioactive with 4.8×10^{10} y half-life time. It is a pure β emitter and has 27.8% isotopic abundance.

Finally there are four natural **radioactive decay chains**: Uranium, Thorium, Actinium and Neptunium decay chains. Their half-lives are of the order of the Earth age and their activity is observable still today. This is not the case for the neptunium chain whose progenitor, ^{241}Pu, has a half life of 14 years and the longest lived element of the chain ^{237}Np has an half life of 2.14×10^{6} y which is relatively short when compared to the age of the Earth. It is therefore now extinguished and the only surviving element is ^{209}Bi, a stable isotope. Uranium and Thorium are usually present in nature with an abundance ranging from a few to several tens of p.p.m. (parts per million), depending on the type of rocks. Uranium is commonly found in four different isotopes with mass numbers 230, 234, 235 and 238.

^{238}U is the progenitor of the Uranium chain and has 99.28% isotopic abundance. It is usually in secular equilibrium with ^{234}U which belongs to the same decay chain and has 0.0058% isotopic abundance. Also ^{230}U belongs to the same family and has very short life time ($t_{1/2} = 20.8$ days). The main contribution of this chain to natural radioactivity is due to **Radon** and its daughters. ^{222}Rn comes from ^{226}Ra α decay. This is widely distributed in rocks and soil. Being chemically very active and having 1.620 y half life time it might give rise to a breaking from the secular equilibrium in the radioactive chain. Furthermore ^{222}Rn is a noble gas and it degasses from materials containing Radium, consequently breaking the equilibrium. The ^{222}Rn half life time (3.38 days) is long enough for this gas to diffuse through the rock and into the air or groundwater. The ^{222}Rn decay is followed by several α and β emitters with short lives (from $\sim 10^{-4}$ seconds to some minutes) till the ^{210}Pb isotope with 22 years half life time. As will be described in the following paragraphs, ^{210}Pb is the main contaminant of low background shielding lead. Radon daughters are originally positively charged, so they either stick to aerosols or they remain in form of ions and free atoms. The distribution of these radionuclides is therefore strongly dependent on pressure and ventilation. The deposition of dust particles on materials is favoured when they have electrostatic charged surfaces, as it usually happens in the case of plastic and glass.

^{235}U is the progenitor of the Actinium decay chain and is also the main radionuclide used in artificial fission processes. It has 0.71% isotopic abundance and therefore is less relevant to natural radioactivity than the Uranium chain.

^{232}Th is the main constituent of natural Thorium ($\sim$ 100% isotopic abundance). Though the total activity of the Thorium chain is about one third compared to the Uranium chain, its abundance is about four times more and thus both chains give about the same contribution to natural radioactivity.

Among the man-made radionuclides, mainly originated from weapon tests or nuclear power plant accidents, the most important are ^{90}Sr and ^{137}Cs. They are both β emitters and relatively long lived: 20.8 y and 30.2 y half life time, respectively. The β decay of ^{137}Cs is accompanied by a 661.6 keV γ emission line. Another radionuclide which is relevant for low background experiments is ^{60}Co. It is a β emitter with 5.12 years half life time and is present in all modern steel. It decays to ^{60}Ni emitting two characteristic cascade γ lines of 1.173 and 1.332 MeV.

2.1.3 Radioactivity at L.N.G.S.

The CRESST facility is located at the Laboratori Nazionali del Gran Sasso, in the motorway tunnel of the Gran Sasso mountain at an average depth of 3.5×10^5 g$\cdot$cm^{-2} of standard rock[1]. The rock overburden offers on one side an efficient shield against cosmic rays, on the other side it is itself source of radioactivity due to the presence of natural radionuclides as explained above. Thanks to its mean thickness of ~3700 m.w.e.[2] (with a minimum value of 3150 m.w.e) the flux of the most penetrating component of the cosmic rays, muons, is reduced by a factor $\sim 10^{-6}$ to about 1 m^{-2} h $^{-1}$. Only cosmic ray muons of more than ~1 TeV can reach the underground laboratories [dGS]. Gran Sasso rock has an average density of 2.71±0.05 g cm^{-3} and is mainly calcareous but also elements as Aluminium, Silicium, Magnesium and organic sediments are present. In table 2.1 and in table 2.2 the chemical composition of the rock and the relative weight of the single elements are reported.

Type of Rock	Chemical Composition	% Weight
Dolomite	$CaCO_3$ (90%), $MgCO_3$ (10%)	50
Dolomitic limestone	$CaCO_3$ (50%), $MgCO_3$ (50%)	29
Silicium limestone	$CaCO_3$ (72%), SiO_2 (8%), Si, Al, K compounds (20%)	8
Carsic formation	$CaCO_3$	9
Detritus	$CaCO_3$ (49%), $MgCO_3$ (1%), Si, Al, K compounds (50%)	3

Table 2.1: Chemical composition of Gran Sasso rock

Element	Relative Weight (%)
H	0.03
C	12.17
O	50.77
Mg	8.32
Al	0.63
Si	1.05
K	0.10
Ca	26.89

Table 2.2: Relative weight of the elements constituting the Gran Sasso rock.

---

[1] Conventional homogeneous material with Z=11 and A=22

[2] meter water equivalent

The activity of samples of rock coming from the different Laboratory halls has been measured and results are reported in table 2.3. The activity is rather low in Hall B and C while it is higher in Hall A. This is due to the different local composition of the rock. In particular in Hall A an infiltration of black marly rock has been found, which explains this difference in activity. The integral gamma flux calculated for all natural chains is $\sim 1\gamma$ cm^{-2}·s^{-1}[Arp92], while the activity due to ^{222}Rn with the present ventilation system and monitored near Hall C is of about 30÷Bq·m^{-3}. Phase I of CRESST was located in Hall B as shown in picture 2.1. Within one year after completion of Phase I the CRESST facility has been successfully moved to Hall A.

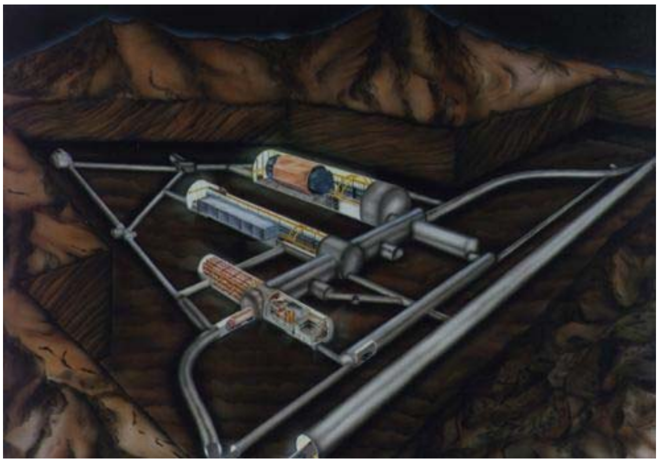

Figure 2.1: Planimetry of L.N.G.S. underground laboratories. Hall B is in the middle between the longest Hall C (the top cylinder in the figure) and Hall A, the present place of the CRESST setup.

Sample	Activity [Bq·kg^{-1}]			
	^{232}Th	^{238}U	^{40}K	^{214}Bi
Hall A Rock	8.8 ± 0.3	84.7 ± 8.4	224 ± 6	41.9 ± 0.6
Hall B Rock	0.25 ± 0.08	5.2 ± 1.3	5.1 ± 1.3	4.2 ± 0.3
Hall C Rock	0.27 ± 0.10	8.2 ± 1.7	2.9 ± 1.4	5.1 ± 0.2

Table 2.3: Activity of samples of rock from Hall A, B, and C of Gran Sasso underground laboratories.

Neutrons in an underground laboratory can originate from muon interactions in the last meters of rock and from spontaneous fission or (α,n) reactions due to natural radioactivity of the rock. The neutron flux in the Gran Sasso Halls has been measured by different groups with different techniques as reported in table 2.4. The integral flux calculated for energies above 1 MeV is consistent in both cases and is of the order of 10^{-6}cm^{-2} s^{-1}.

A		B	
Energy interval (MeV)	Neutron flux (10^{-6}cm^{-2}s^{-1})	Energy interval (MeV)	Neutron flux (10^{-6}cm^{-2}s^{-1})
$< 50 \times 10^{-9}$	1.07 ± 0.05		
$50 \times 10^{-9} \div 10^{-3}$	1.99 ± 0.05		
$10^{-3} \div 2.5$	0.53 ± 0.008	$1 \div 2.5$	0.14 ± 0.12
$2.5 \div 5$	0.18 ± 0.04	$2.5 \div 5$	0.13 ± 0.04
$5 \div 10$	0.04 ± 0.01	$5 \div 10$	0.15 ± 0.04
$10 \div 15$	$(0.7 \pm 0.2)10^{-3}$	$10 \div 15$	$(0.4 \pm 0.4)10^{-3}$
$15 \div 25$	$(0.1 \pm 0.3)10^{-6}$		

Table 2.4: Neutron fluxes measured in the given energy intervals.
A: measured in hall A with BF_3 counters [Bel85].
B: measured in hall C with proton recoil scintillators in an energy range > 1 MeV [Arn99].

Neutrons might scatter elastically or inelastically off the nuclei of the detecting medium. Elastic scattering dominates at energies below 1 MeV [The96], neutrons of these energies therefore constitute a dangerous source of background for Dark Matter searches. For example, using equation 1.20 for a neutron elastic scattering off an ^{27}Al nucleus, a maximum recoil energy of 10 keV is obtained for a 75 keV incident neutron, which would result in a fake signal. Inelastic scattering on the other hand, besides producing a target nuclear recoil, would excite the nucleus hence inducing a de-excitation gamma emission. The observed result from several inelastic scatterings would then be a gamma peak broadened by a distribution due to nuclear recoils [Mar00].

A neutron shield is presently in preparation to complete the CRESST Phase II set-up.

2.2 CRESST experimental setup

The CRESST Phase I experiment was designed to operate simultaneously four $40 \times 40 \times 41$mm^3 sapphire crystals of 262g each. The CRESST cryostat has been specially designed with a low background cold box housing the detectors well separated from a commercial ^{3}He/^{4}He dilution refrigerator (Oxford Instruments). The cooling power of the cryostat is then transferred to the detectors via a 1.5 meter copper cold finger (see[Büh96]). The cold-box, shown in fig. 2.2 consists of five concentric radiation shields of copper which surround the experimental volume and the cold finger: a room temperature vacuum can; a liquid nitrogen (77 K) thermal shield; a liquid helium (4 K) shield; 600 mK and finally 80 mK inner thermal shields. The cold finger is connected to the mixing chamber and

Figure 2.2: Picture taken while remounting the CRESST experiment in Hall A. The cold box together with the copper shielding is shown. The outer lead shielding was not yet mounted.

reaches at its bottom a base temperature of about 5 mK; the nitrogen and the helium shields are attached respectively to the liquid nitrogen and liquid helium dewar of the refrigerator. The cold finger and the shields are made of very radio-pure copper, have been welded using the electron beam technique and then electro-polished to remove residual surface contaminations and prevent further recontamination. Finally, low-radioactivity lead is used for the vacuum seals in some of the thermal radiation shields instead of indium which is the usual sealing material for cryogenic application but contains radioactive ^{115}In with 96% isotopic abundance.

A three-storey building (see fig. 2.3) houses the whole set-up with the exception of the helium recovery system and the Liquefier, located in the connecting tunnel between Hall C and B. On the third floor a working area for on-line control of the experiment as well as a small chemistry laboratory, a work-shop instrument storage and a flow box are located. The flow box is a room with a laminar ventilation system which prevents dust from whirling around. Here the detectors are prepared (cleaned, placed in their holders and bonded) before being mounted in the cryostat. On the ground floor a class 100 clean room encloses the passive shielding and most of the cryostat in order to allow clean conditions also while mounting the detectors. A Faraday cage extending over the first two floors surrounds the clean room and the top plate of the cryostat to eliminate external electromagnetic interferences. The cryostat is accessible from the second floor outside the clean room so that all the maintenance can be done without entering the lower level. The gas handling and pumping system necessary for the cryostat as well as the data taking system are placed outside the Faraday cage. The cryostat rests on air dampers to isolate it from vibrations of the floor and it is mechanically decoupled from the pumping system.

Figure 2.3: Three-Storey building of CRESST experiment

2.2.1 The passive shielding

Figure 2.4 shows a schematic view of the cryostat and the passive shieling. In the upper part the dewars for liquid helium and nitrogen are shown. A lead shield rests in-between the dilution refrigerator and the cold box, as well as on the outer part of the figure. Between the lead and the cold box, a Cu shielding is placed.

Lead is a high Z material and is superior to other shielding materials with regard to its background resulting from the interaction of neutrons and muons and from activation. Lead has in fact a high cross section for photo-electric absorption and muon capture compared to lighter elements and its low cross-section for neutron capture reduces the level of radio-isotopes which may be activated cosmogenically. It is therefore a highly effective material for γ shielding. On the other hand, due to the photo-electric absorption, Pb K-shell X-rays with energies of 72.8, 75.0, 89.4 and 84.7 keV may be emitted. Furthermore, it is quite a difficult procedure (and hence very expensive) to produce lead with a low ^{210}Pb concentration. Its β decay with a lifetime of 22.3 years and 63.5 keV transition energy is followed by β decay of ^{210}Bi to ^{210}Po with half-lifetime of 5.0 days and a transition energy of 1162.7 keV. This short chain ends with an α

decay of ^{210}Po to ^{206}Pb with a lifetime of 138.3 days and a transition energy of 5407.4 keV [Ale98]. ^{210}Bi energetic beta particles contribute to background by inducing Bremsstrahlung radiation and characteristic lead X-rays as mentioned above.

An inner layer of very radio-pure material is then usually added inside the lead shield, to absorb this radiation. This layer is usually made of very pure lead or copper. Despite its lower Z, copper has the advantage that it can be produced with high purity levels [Heu95]. Once copper has been electrolytically produced it is necessary to immediately store it underground. Cu has in fact the drawback of having a considerable neutron capture cross-section. Therefore its exposition to cosmic neutrons would result in the production of a significant amount of radioactive nuclei.

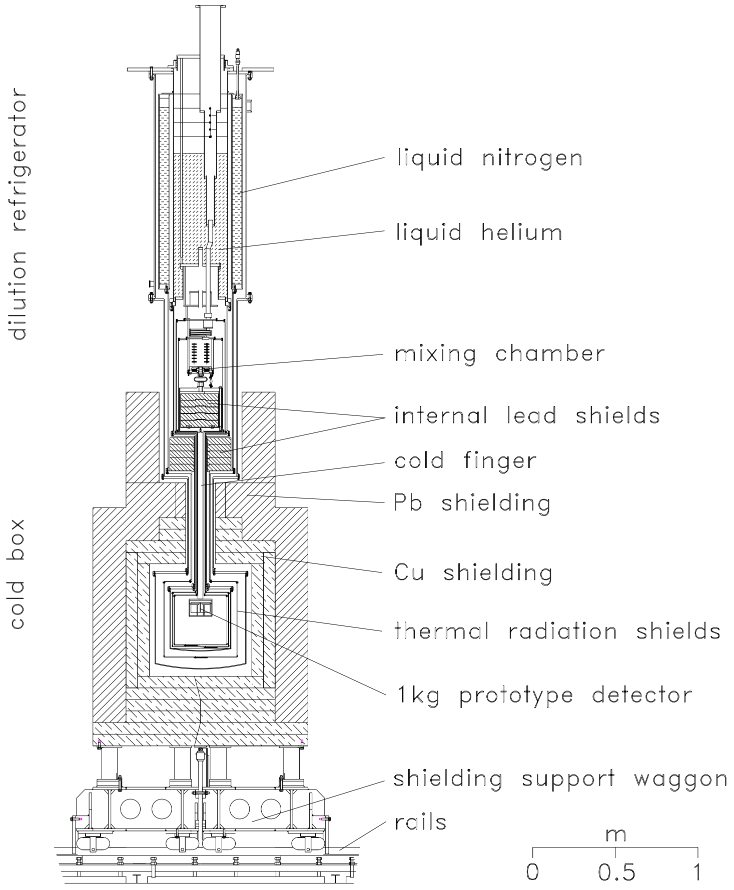

Figure 2.4: Schematic view of CRESST cryostat and passive shielding.

The CRESST shielding is composed of 14 cm of radio-pure copper directly enclosing the cold box, followed by 20 cm of Boliden Lead with a ^{210}Pb activity of 35 Bq/kg for a total mass of 24 tons. To block the line of sight of the detectors to the upper part of the cryostat, Plombum lead with a ^{210}Pb content of 3.6

Bq/kg is used. Finally, the entire shielding is enclosed in an air-tight Aluminium container which is constantly flushed with N_2 gas at a slight overpressure in order to prevent radon from penetrating the shielding.

2.2.2 The crystals and other materials

CRESST Phase I detector consist of 262 g sapphire crystals. The temperature rise in the sapphire absorber is measured using a Superconducting Phase-transition Thermometer (SPT), realized by evaporating a ~2000 Å layer of superconducting tungsten (see next chapter). Each thermometer is provided with small aluminium and gold pads for thermal and electrical connection. For Phase II detector modules a $CaWO_4$ scintillating absorber together with a CRESST type sapphire or silicon light detector are being developed. The module is enclosed in a reflective foil for a better light absorption. Each type of detector (both for Phase I and II) is housed in a copper holder thermally and electrically isolated from the cryostat base-plate and the crystals are held tight in their holder via Delrin tips.

Element	limit (ppb)		counts/(keV kg day)	
	SCT	CS	SCT	CS
U	0.04	0.02	<0.8	<0.4
Th	0.033	0.0023	<2.9	<0.2
K	900	1800	<1.7	<3.4
^{26}Al	10^{-6}	-	<0.006	-

Table 2.5: Upper limits of the Uranium, Thorium and Potassium (detection limits of the neutron activation analysis) and ^{26}Al content (accelerator mass spectroscopy limit) of sapphire crystals from Single Crystal Technology (SCT) and Crystal System (CS) and resulting continuum count rates in the range 0-25 keV (excluding X-ray lines). Conversion factors are: 1 mBq ^{238}U/kg := 81 ppt U; 1 mBq ^{232}Th/kg := 246 ppt Th; 1 mBq ^{40}K/kg := 32.3 ppt K. One ppm of natural K (10^{-6} g K per gram material) corresponds to 0.12 ppb of K40 [Büh96].

If any of these components contains radioactive contamination, in addition to gamma rays and bremsstrahlung photons, also alpha and beta particles, characteristic X-rays and Auger electrons would drastically affect the measured energy spectrum. Therefore special care must be taken in selecting and then handling these materials. The radio-purity of sapphire crystals from different suppliers was measured with the neutron activation technique as reported in table 2.5.

A low-background Germanium counting facility at the Gran Sasso underground laboratories has been used to measure potential contaminations in the sapphire, in different $CaWO_4$ crystals, in the reflective foil and other samples. It consists of several High Purity coaxial Germanium (HPGe) detectors of a relative efficiency[3] ranging from 84.8% to 119.9%. The results of these measurement are reported in the Appendix A.

---

[3] intrinsic efficiency relative to a standard Na(Tl) scintillator[IEE86]

Chapter 3

CRESST detectors

CRESST is a Cryogenic Rare Event Search using Superconducting Thermometers to measure the signal produced by a particle interaction in the absorber. The use of cryogenic detectors in WIMP searches have the advantage of having low energy threshold, excellent energy resolution and, as described in Chap.1, a quenching factor equal to one. This combination makes them unique in sensitivity for the detection of nuclear recoils that would result from a WIMP interaction. Moreover, as discussed in Chap. 2, the main limitation in a rare event search is the residual radioactive background. Therefore dramatic improvements in sensitivity are to be expected if the detector itself is able to discriminate between electron recoil (α, β, γ events) and nuclear recoil (WIMP and neutron events).

In this chapter the general detection principles of low temperature detectors are presented. A detailed description of the detectors employed for CRESST Phase I as well as an overview of the detector module developed for CRESST Phase II are then given in the chapter.

3.1 Cryogenic detectors

The detectors developed for CRESST consist of a dielectric target crystal with a small superconducting thermometer evaporated onto one surface. When the film is stabilised at a temperature between its superconducting to normal conducting phase, it functions as a highly sensitive thermometer. In a very simplified model of a calorimeter, the energy ΔE deposited in an absorber due to a particle interaction increases the absorber temperature of

$$\Delta T = \frac{\Delta E}{C}, \tag{3.1}$$

where C is the heat capacity of the absorber. In a dielectric material, due to the absence of conduction electrons, the heat capacity at low temperatures is dominated by the phonon system in which $C \sim (T/\Theta_D)^3$, where Θ_D is the Debye temperature. At mK temperatures this T^3 dependence renders the heat capacity of the absorber very small and results in a measurable rise in the temperature following a particle interaction. In an ideal model, an energy deposition is instantaneously followed by an increase of temperature which then relaxes back exponentially to its equilibrium value via a thermal link to a heat sink at a constant temperature T_B as shown in fig. 3.1. The thermal relaxation time is

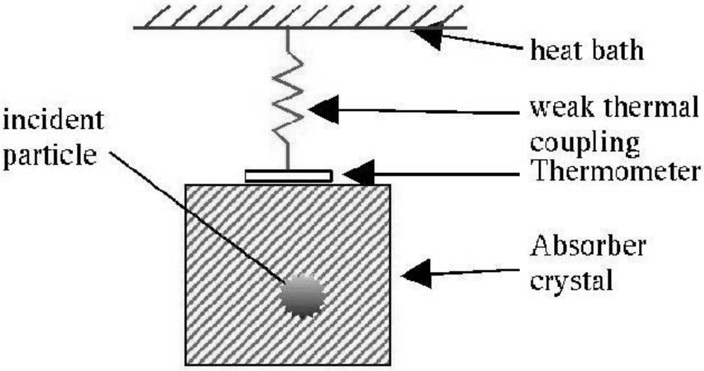

Figure 3.1: Schematic view of a calorimetric detector.

$$\tau = \frac{C}{G} \tag{3.2}$$

where C again is the heat capacity of the absorber and G the thermal coupling to the heath bath. In reality this simple model is not sufficient to describe the behaviour of the detectors. The rise time is not infinitely fast due to the different processes occurring between a particle interaction and the observed signal. The decay usually is not a simple exponential, but has two components with different time constants. These are commonly referred to as thermal (slower component) and non-thermal (faster) component. Moreover one has to consider the different phonon and electron systems within thermometer and absorber in order to determine a more accurate model for the signal evolution.

3.2 Model for pulse formation

The observed pulse shape depends on the various processes occurring in the real detector. After any event the different parts of the system will be out of equilibrium and will assume different temperatures. This will lead to heat flows until a new thermal equilibrium is established. The way the subsystems return to equilibrium values is determined by the thermal coupling between the systems. This finally influences the temperature of the electron system of the thermometer, the signal which is eventually measured. A detailed description of a theoretical model for the signal evolution for low temperature calorimeters is given in [Prö95]. In the following paragraphs this model is summarised.

3.2.1 Excitation and propagation of phonons in the absorber

Any energy deposition in the dielectric absorber, due to ionising radiation or to WIMP and neutron interaction will create high frequency phonons. Ionising radiation releases its energy in the electron channel, i.e. via inelastic interaction with the electrons. It first creates highly excited electrons which loose their energy by transfer to other electrons and/or by exciting electron hole pairs. Once the energy of the excited electrons is lower than twice the energy gap in the dielectric no further excitation of electron hole pairs is possible and within ~10ps the relaxation happens via emission of optical phonons. The relaxation through other channels (e.g. photons) is usually suppressed by the small density of states of these excitations. This process is however important in the case of scintillating crystals for the event discrimination. On a time scale of a few 100ps the high energy optical phonons decay into two acoustical phonons with about half the Debye frequency $\nu_D/2$, leading to an almost monoenergetic phonon distribution. For sapphire $\nu_D = k_b \Theta_D / h \sim 21.7$ THz.

The energy released in the nuclear branch, i.e. via elastic interactions with nuclei, excites instead non-thermal acoustic phonons in a broad frequency range either directly or via structural defects. The fraction of energy released via this channel, negligible for photon and electron interaction, becomes important for alpha and heavy ions and is dominant for WIMP and neutron interactions. These high frequency phonons excited via both channels are not in equilibrium and rapidly decay via anharmonic three phonon process with a decay rate $\Gamma \propto \omega^5$.

In a sapphire crystal, starting with a phonon population at half the Debye frequency (10.8 THz), numerical simulations show an initial very rapid (10μs) decrease of their mean energy down to about 600 GHz. After this all differences in the phonon spectrum caused by interactions via nuclear and electronic channels are washed out and phonons spread ballistically over the crystal. On a timescale of ms the frequency of the non thermal phonon population does not change significantly anymore, i.e. phonons are not thermalized on ms time scales. For comparison, 600 GHz corresponds approximately to the maximum of a 10K Planck distribution.

3.2.2 Transmission at interfaces

After a few surface reflections the non thermal phonons are uniformly distributed in the crystal. The time required can be estimated from crystal dimensions and the sound velocity averaged over directions and modes. For sapphire crystals this velocity is $v = 6490\mathrm{m/s}$. Since L=4 cm is the crystal dimension the time scale required in this case is $\mathrm{L}/v \sim 6\mu\mathrm{s}$ [Sis99]. This time is still much shorter than the rise time of the pulse, typically ~ms. Furthermore typical collection times of the thermometer are of the order of 100 μs. Therefore, the phonon population usually does not thermalize in the absorber.

If such high frequency phonons enter the thermometer they readily interact with the free electrons of the film. At very low temperatures the electrons and phonons of the thermometer are treated as thermally weakly coupled subsystems. Thus the electron system experiences a time dependent power input $P_e(t)$ due to the absorption of non thermal phonons which is the origin of the fast component of the signal. The absorption of high frequency phonons in the thermometer competes with their thermalization in the crystal. A fraction ϵ is thermalized in the thermometer and $(1-\epsilon)$ in the absorber.

Assuming that all the phonons transmitted into the thermometer are absorbed, the ideal collecting time is given by

$$\tau_0 = \frac{2V_a}{A < v_\perp \alpha >} \tag{3.3}$$

τ_0 = ideal collecting time
V_a = absorber volume
A = area of the absorber-thermometer interface
$v_\perp$ = phonon group velocity normal to the interface
α = transmission probability
$< ... >$ = average over modes and wave vectors of incident phonons

Numerical calculations for the interface sapphire crystal to tungsten strip yeld

$$< v_\perp \alpha >_{Al_2O_3 \rightarrow W} = 2548 m/s. \tag{3.4}$$

Given η the effective absorption probability of the high-frequency phonons transmitted into the thermometer then the thermalization rate in the film is

$$\tau_{film} = \frac{\tau_0}{\eta} \tag{3.5}$$

A value of η less than one is expected because the interaction of non-thermal phonons depends on their polarisation. Longitudinal high frequency phonons interact much stronger than transverse phonons with the electrons of the tungsten film. Neglecting the absorption of transverse phonons, $\eta = 0.29$ is calculated for transmission from sapphire to tungsten. Furthermore an incomplete absorption of longitudinal phonon modes may arise from an insufficient thickness of the thermometer.

The electron and thermal phonon subsystems in the thermometer are thermally coupled by $G_{ep} \propto \mathrm{T}^5$, and the thermal phonons in the thermometer are coupled to the thermal phonons in the crystal via the Kapitza coupling G_K. At very low temperatures $G_K >> G_{ep}$. Part of the energy thermalized by the electrons escapes via the thermal coupling of the thermometer to the heat bath, the rest flows back as thermal phonons into the crystal thus rising its temperature. The transmission of thermal phonons across the boundary between the thermometer and the absorber is governed by the Kapitza boundary conductance $G_K \propto \mathrm{T}^3$ between the thermal phonons in the thermometer and the absorber. For a sapphire-tungsten interface G_K/T^3 was numerically evaluated to 0.430 kW K^{-4} m^{-2}. At operating temperature $\sim$ 15 mK the thermal coupling of the tungsten film to the crystal is very weak, thus the dominant process is the relaxation of the thermometer to the heat bath.

The detector is thermally coupled to the heat sink via a gold bond wire. The coupling strength defines the thermal relaxation time $\tau = C/G$ of the thermometer and can be calculated with Wiedemann-Franz-Law which connects electric resistance R and thermal conductance G

$$G = \mathcal{L}T/R \tag{3.6}$$

where $\mathcal{L}$ is the Lorentz number (24.5 $\mathrm{nW\Omega/K^2}$).

The phonons in the absorber can be schematically seen as composed of two populations, the thermal and the high frequency phonons. In fig. 3.2 $P_a(t)$ represents a direct power input in the absorber due the thermalization of high frequency phonons by parasitic inelastic processes at the crystal surface. The thermal component of the pulse represents the temperature rise of the absorber seen by the thermometer.

Finally it can be shown that the initial power input into the thermometer can be written as

$$P_0 = \frac{\epsilon \Delta E}{\tau_{film}} \tag{3.7}$$

with ΔE is the energy deposited by the incident particle.

3.2.3 The calorimeter model

In fig. 3.2 a schematic representation of the thermal model is given. In this model it is assumed that the detector consists of three weakly coupled thermal subsystems, namely the electrons in the thermometer, the phonons in the thermometer and the phonons in the absorber. Each of them is characterised by its heat capacity C and its temperature T. They are thermally coupled via the respective coupling constants $G_{ab}, G_K, G_{ep}, G_{eb}$, and G_{ea} where

G_{ab} = direct coupling of the absorber to the heat bath via its mechanical mounting.
G_{ea} = effective coupling between the phonon system of the absorber and

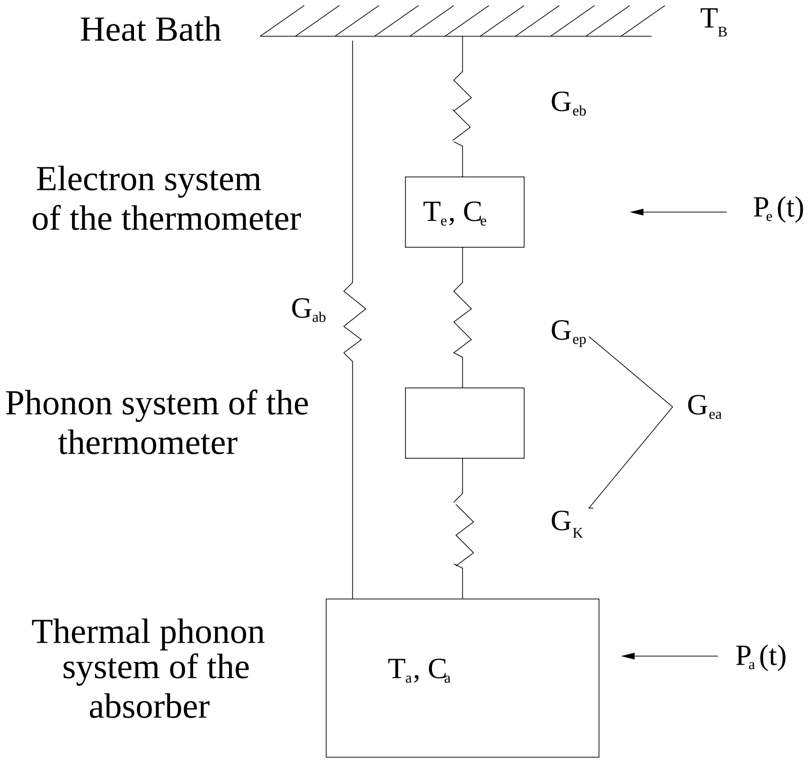

Figure 3.2: Thermal model of a calorimeter.

the electron system of the thermometer. Since the heat capacity of the phonon system of the thermometer is negligible one can replace the Kapitza coupling ($G_K \propto T^3$) between the two phonon systems and the electron-phonon coupling ($G_{ep} \propto T^5$) with

$$G_{ea} = \left(\frac{1}{G_{ep}} + \frac{1}{G_K} \right)^{-1} \tag{3.8}$$

As previously mentioned the non-thermal phonons will either be absorbed in the thermometer and heat the electrons at temperature T_e with a power input $P_e(t)$ or directly thermalize in the absorber and contribute to P_a. For a mathematical description the following assumptions are also made:

- the total deposited energy ΔE creates high frequency phonons directly after the interaction
- the energy density $\Delta E/V_a$ of high energy phonons has no spatial dependence
- assuming that the thermalization rate of this phonons is independent of their frequency the time dependent power inputs can be described by

$$P_e(t) = P_0 e^{-t/\tau_n}, \quad P_a(t) = \frac{1-\epsilon}{\epsilon} P_e(t) \tag{3.9}$$

where τ_n is the effective time constant for the thermalization of high frequency phonons and is given by the contribution of thermalization in the absorber $\tau_{crystal}$ and in the thermometer τ_{film} (defined in the previous section) and is given by

$$\frac{1}{\tau_n} = \lambda_n = \frac{1}{\tau_{film}} + \frac{1}{\tau_{crystal}} \tag{3.10}$$

The time constant τ_{film} is proportional to the volume V of the absorber and indirect proportional to A. $\tau_{crystal}$ is a property of the crystal and the crystal surface, and is expected to scale like $\tau_{crystal} \sim V/O$, where O is the surface area of the crystal.

- the thermal conductance of the absorber film is high enough that its temperature has no spatial dependence

The thermal model of figure 3.2 can be described by two coupled differential equations for the temperature T_e of the electrons in the thermometer and the temperature T_a of the phonons in the absorber:

$$\begin{aligned} C_e \frac{dT_e}{dt} + (T_e - T_a)G_{ea} + (T_e - T_b)G_{eb} &= P_e(t) \qquad (3.11) \\ C_a \frac{dT_a}{dt} + (T_a - T_e)G_{ea} + (T_a - T_b)G_{ab} &= P_a(t) \qquad (3.12) \end{aligned}$$

With the initial condition $T_a(t=0) = T_e(t=0) = T_b$ the equations have the following solution for the thermometer signal $\Delta T(t)$:

$$\Delta T_e(t) = \Theta(t)[A_n(-e^{-t/\tau_{in}} + e^{-t/\tau_n}) + A_t(e^{-t/\tau_t} - e^{-t/\tau_n})] \tag{3.13}$$

As specified before, the time between interaction in the absorber and the establishment of a homogenous distribution of non-thermal phonons was neglected. This is expressed by the step function $\Theta(t)$.

The time constants are:

$$\begin{aligned} \tau_{in} &= \frac{1}{\lambda_{in}} = \frac{2}{a + \sqrt{a^2 - 4b}} & \tau_t &= \frac{1}{\lambda_t} = \frac{2}{a - \sqrt{a^2 - 4b}} \\ a &= \frac{G_{ea} + G_{eb}}{C_e} + \frac{G_{ea} + G_{ab}}{C_a} & b &= \frac{G_{ea}G_{eb} + G_{ea}G_{ab} + G_{eb}G_{ab}}{C_e C_a} \end{aligned} \tag{3.14}$$

and the amplitudes:

$$A_n = \frac{P_0(\lambda_{in} - (G_{ab}/C_a))}{\epsilon(\lambda_t - \lambda_{in})(\lambda_{in} - \lambda_n)} \left(\frac{\lambda_t - G_{ab}/C_a}{G_{eb} - (C_e/C_a)G_{ab}} - \frac{\epsilon}{C_e} \right) \tag{3.15}$$

$$A_t = \frac{P_0(\lambda_t - (G_{ab}/C_a))}{\epsilon(\lambda_t - \lambda_{in})(\lambda_t - \lambda_n)} \left(\frac{\lambda_{in} - G_{ab}/C_a}{G_{eb} - (C_e/C_a)G_{ab}} - \frac{\epsilon}{C_e} \right) \tag{3.16}$$

In equation 3.13 τ_{in} is the intrinsic time constant of the thermometer and τ_t is the thermal relaxation time of the combined system.

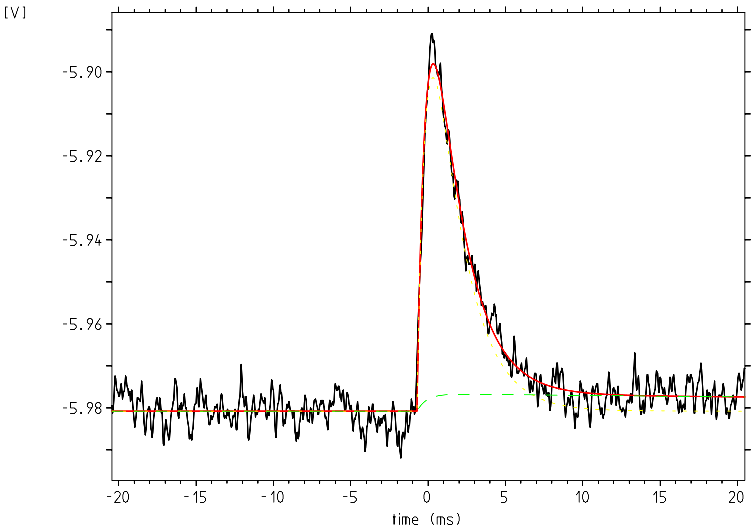

Figure 3.3: Thermal component (dashed line) and non-thermal component (dotted line). The solid line represents the fit of the pulse.

The physical interpretation of eq. 3.13 depends on the operating temperature of the detector, the strength of the coupling G_{eb} of the thermometer to the heat bath and the resulting ratio of τ_n and τ_{in}. In the case of a strongly coupled thermometer or at higher operating temperatures (the so called "bolometric mode") part of the energy flows to the heat sink before it is completely collected in the thermometer. In this case the pulse rises with τ_{in} and decays with τ_n. On the contrary, for low temperatures and weak coupling of the thermometers $\tau_n < \tau_{in}$ and the detector is in the calorimetric mode. This means that the relaxation time of the thermometer is long enough that the energy flux of the non-thermal phonons which have a life time τ_n can be integrated. τ_n is the life time of the non-thermal phonons in the absorber and shows up as the rise time of both components. A_n, τ_{in} describe the non-thermal component of the signal. It originates from the direct absorption of non-thermal phonons in the thermometer. A_t, τ_t represent the thermal component of the signal caused by temperature rise in the absorber as it is measured by the thermometer.

3.3 CRESST absorbers

CRESST Phase I employed sapphire crystals as absorber. Being a dielectric material with high Debye temperature ($\Theta_D = 1040.8$ K), small heat capacities can be achieved by operating it at very low temperatures. High Debye temperature means also high speed of sound (see for example [Ash76]). This results in a very high energy flow into the thermometer after a particle interaction (see equations 3.3, 3.5 and 3.7), hence a very sensitive detector with a low energy threshold is achievable.

The thermometers which detect the phonon signal consist of tungsten strips evaporated onto the surface of the crystal. The high melting point of sapphire (T_{melt} =2310 K) avoids inter-diffusion with the tungsten thermometer during the evaporation of the film which takes place at ~500 °C [Sis99]. Another important property of sapphire crystals as absorber is their radio purity. Sapphire (Al_2O_3) contains only stable isotopes ^{16}O (99.76% isotopic abundance), ^{17}O (0.04%), ^{18}O (0.2%) for the oxygen and 100% ^{27}Al for the aluminium. As reported in the previous chapter the radio purity of sapphire crystals was studied with neutron activation analysis and germanium gamma spectroscopy. The results are shown in tables 2.5 and A.1 and report only upper limits. Finally the presence of 100% ^{27}Al with a ground state nuclear spin of 5/2 makes this absorber fully sensitive to spin-dependent WIMP-nucleon interactions.

CRESST Phase II is using a scintillating crystal as absorber. Also in this case a particle interaction excites phonons, but a small amount of the deposited energy ($< 2\%$) is converted into scintillation light. Since nuclear recoils which result from WIMP or neutron interaction release less light than electron recoils one can identify the type of interaction via operating a cryogenic detector in coincidence with a light detector. The ratio of scintillation light and phonon signal then allows an event-by-event discrimination.

As a first step the light output of several scintillating crystals, i.e. BGO, BaF_2, $PbWO_4$ and $CaWO_4$ was studied, showing adequate light output at milli Kelvin temperature [Meu99]. $CaWO_4$ was eventually chosen due to its relatively large light output and high target nucleus mass. As discussed in Chap.1, this enhances the WIMP-nucleus scalar cross-section due to its A^2 dependence and will also enable CRESST Phase II to probe higher WIMP masses ($\geq$ 30 GeV) which are favoured by theory. Another selection criteria is its radio purity compared to other candidates. Depending on the manufacturer $CaWO_4$ showed good radio purity levels when investigated with gamma spectroscopy as shown in table A.2 However, due to his high Z $CaWO_4$ is characterised by a high self absorption. Therefore neither pure alpha or beta emitters nor low energy gamma radiation such as 46 keV gamma emission line of ^{210}Pb can be detected with germanium spectroscopy.

A first proof-of-principle detector with $CaWO_4$ as scintillating absorber operated together with a small sapphire detector to collect the emitted light gave the results shown in fig. 3.4. In this figure the scatter plot of the pulse height in the light detector versus the pulse height in the phonon detector is shown. The signal of the phonon detector measures the total energy deposited in the absorber, independent of the interaction, whereas the $CaWO_4$ light output due to electron recoils is quite high compared to nuclear recoils. The measured ratio is 7.4. The measured quenching factor for alpha particles of 3.6 is lower, which however still allows to discriminate α from neutron interactions. Finally a rejection factor of 98% was proven down to 10 keV, of 99.7% in the energy range between 15 and 25 keV and better than 99.9% above 25 keV, thus allowing a clear separation of the electron to the nuclear recoil band down to 10 keV [Meu99].

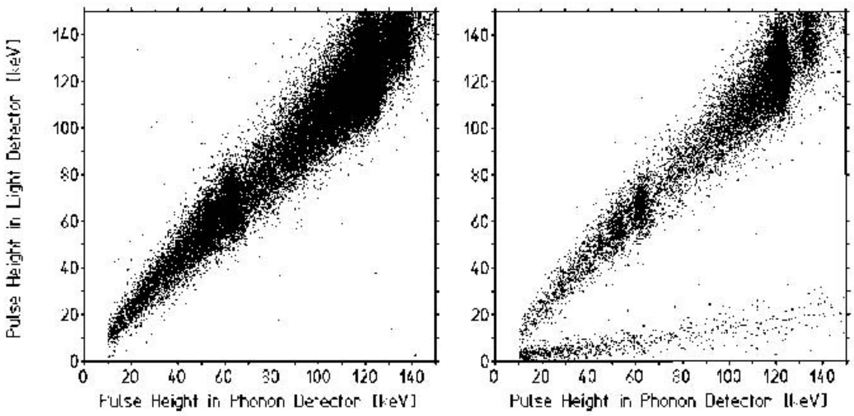

Figure 3.4: Scatter plot of the pulse height in the light detector versus the pulse height in the phonon detector for the proof-of-principle module. The signal of the phonon detector basically measures the total energy deposited in the absorber, independently of the interaction. The ratio of the phonon signal to light signal then allows to distinguish different types of events. A quenching factor for the light output of 7.4 was measured irradiating the crystal with 122 and 136 keV photons from a Co^{57} source together with ^{90}Sr β source (left picture) and then adding an Americium-beryllium neutron source (right picture) [Meu99].

A picture of the module developed for CRESST Phase II is shown in fig. 3.5. The light detector consists of either a sapphire or a silicon substrate (see[Fra02]) with a tungsten film evaporated onto its surface. In the case of sapphire an additional absorption layer has to be evaporated on the substrate in order to enhance the light absorption. To minimise light losses the whole module is enclosed in a special foil. This is characterised by a reflectivity at room temperature > 98% for wavelengths from 400 to 1000 nm for all incident angles and polarisations

[Fra02].

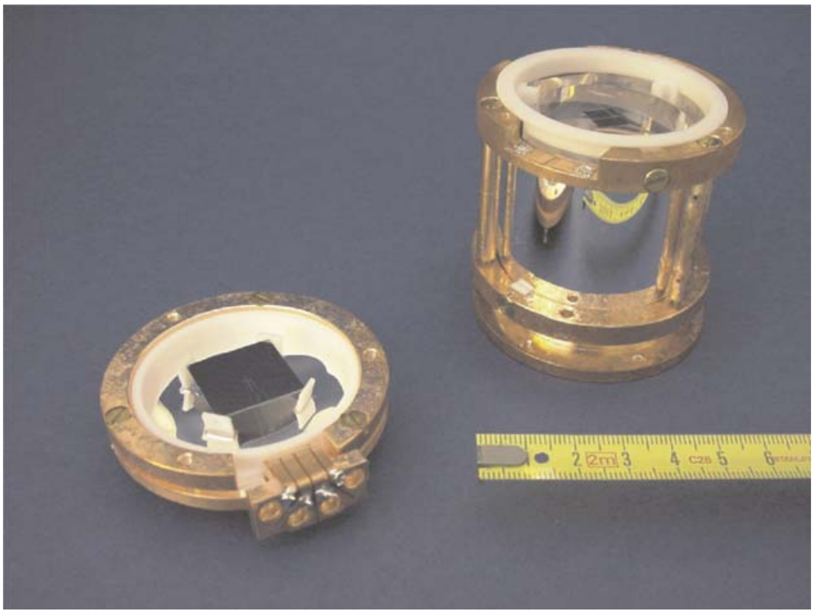

Figure 3.5: Picture of an open detector module for CRESST Phase II.

Compared to sapphire $CaWO_4$ has a few drawbacks. Tungsten films evaporated directly onto its surface have their normal-to-superconducting transition at 40-50 mK. An intermediate diffusion barrier of SiO_2 between the crystal surface and the tungsten must be added to lower the transition to ~15 mK [Fra02]. Another problem is the low speed of sound for the phonons. The Debye temperature calculated from elastic constants is $\Theta_D = 247$ K [Glu73]. Taking this value as an estimate for the mean phonon velocity the speed of sound results to be more than a factor 4.2 slower than in sapphire. The resulting lower energy flux (which would limit the achievable threshold) can however be compensated with a new thermometer design with phonon collectors [Ang02a]. As previously mentioned, its higher target nuclei mass and the event-by-event discrimination will allow CRESST Phase II to be about four orders of magnitude more sensitive in investigating WIMP-nucleus cross-sections than the actual limit set by the first phase.

3.4 CRESST Thermometers

The temperature rise which follows an energy deposition in the absorber is measured via Superconducting Phase-Transition Thermometers (SPT). CRESST SPTs consist of a thin superconducting tungsten strip evaporated onto the surface of the absorber. Typical dimensions are a thickness of $0.5 \div 2$ kÅ and an area of a few mm^2. As illustrated in fig. 3.6 in the transition of tungsten from the normal-conducting to the superconducting phase a small change in temperature results in a relatively large change in resistance and can be exploited to make an extremely sensitive thermometer. For sapphire detectors transition widths are ~1 mK. An energy deposition of 6 keV results in a temperature rise of about 40 μK while the detector is stabilised within a few μK.

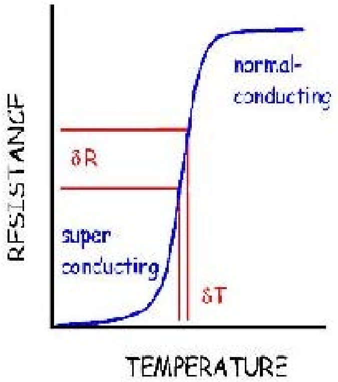

Figure 3.6: Schematic normal-conducting to superconducting phase transition curve.

The detector performance depends on the shape of the transition curve and the heat capacity of the thermometer at the operating point and can vary significantly from film to film. The width of transition defines the dynamic range while the sensitivity depends on its slope: the steeper the transition the more sensitive is the detector to a small energy deposition. The sensitivity however depends also on the read-out current: for high currents the sensitivity increases, on the other hand critical current effects and self heating in the film would broaden the transition hence setting a maximum. In fig. 3.7 the measured transition curves of a sapphire detector at Gran Sasso for different currents are shown.

The heat capacity of the thermometer is a crucial parameter for CRESST detectors which are mostly sensitive to non-thermal phonons. As previously introduced, these are efficiently absorbed by the free electrons in the thermometer and mainly thermalize there. This means that the temperature of the thermometer rises above that of the absorber and the contribution of this non-thermal component to the pulse amplitude is determined by the heat capacity of the thermometer and the absorbed energy. The heat capacity can be decreased by optimization of the film geometry. The reduction of the film size and thickness is however limited by the collection efficency of non-thermal phonons. In case of very small films, which are required for the light detector, the heat capacity of

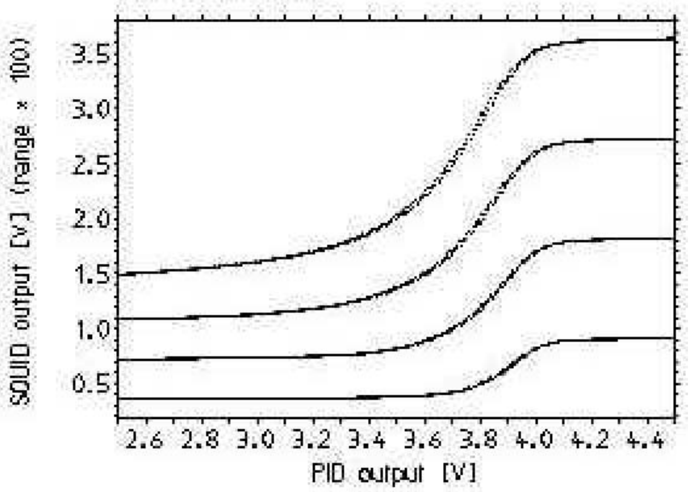

Figure 3.7: Measured temperature sweeps over the normal- to super-conducting phase transition of a sapphire detector for different bias currents of 2, 4, 6 and 8 μA from bottom to top.

gold bond wires would dominate and their thermal coupling strength G cannot be made sufficiently small. Therefore a further reduction of the heat capacity would rather result in a loss of sensitivity (see [Fra02]).

In general, in metals the electronic part of the heat capacity dominates at low temperature, while the phononic contribution is negligible at mK temperatures. The electronic specific heat depends linearly on the temperature. Considering then in particular a superconducting metal, the specific heat has a discontinuity at the critical temperature T_c. Well below the transition temperature it decreases exponentially, while its value in the transition region can be expressed by

$$C_{op} = C_e \left(2.43 - 1.43 \frac{R_{op}}{R_n} \right) . \tag{3.17}$$

This assumes that the ratio of actual resistance R_{op} to normal conducting resistance R_n can be taken as a measure of the fraction of the film in the superconducting phase.

3.4.1 Signal Read Out

The resistance change of a low impedance phase transition thermometer is measured via a SQUID readout scheme. As illustrated in fig. 3.8, a constant current I_0 branches between the tungsten thermometer on one side and a shunt resistor in series with the input coil of the SQUID on the other side. For the CRESST experiment 50mΩ shunt resistors are used. The current through the SQUID branch is given by:

$$I_s = I_0 \frac{R_f(T)}{R_f(T) + R_s} \tag{3.18}$$

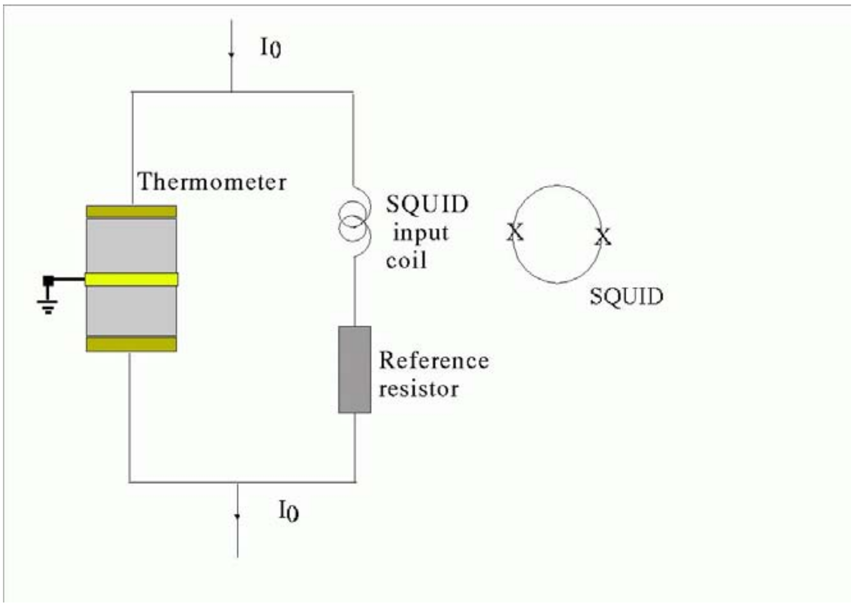

Figure 3.8: Readout circuit

I_s = steady current through the input coil
I_0 = Total current applied
R_f = film resistance
R_s = shunt resistance

Any change in resistance R_f will cause a change of the branching of the of the applied constant current I_0. Thus the increase of the current I_s due to an increase of R_f resulting from an energy deposition changes the magnetic flux coupled to the SQUID by the input coil. SQUIDs are devices which are very sensitive to any change of magnetic flux penetrating in their input loop: the input coil transforms the current into a magnetic flux Φ and this flux is then coupled into the SQUID loop (superconducting ring with two Josephson junctions). The SQUID response to a linearly changing input flux is oscillatory with a period of ϕ_0, where ϕ_0 represents a magnetic flux quantum, i.e. $\phi_0 = h/2e \sim 2 \times 10^{-15}$ Tm^2. To linearise the response an electronic feedback circuitry operates the SQUID in flux locked mode. This means that a separate feedback coil is used to keep the flux through the loop constant. This feedback current is the output signal of the SQUID electronics. When the SQUID is operated in a flux locked mode the relation between current I_s and output voltage V_s is linear following the relation:

$$V_s = \xi(\Phi + n\phi_0) \tag{3.19}$$

where Φ is the input magnetic flux and ξ the gain of the SQUID system. In this way the SQUID acts as a current meter and any ambiguity of the V- Φ relation which was present in the non-linearised case is avoided.

A limitation of this readout scheme is however the maximum rate of flux change which the feedback electronic of the SQUID system can compensate, the slew rate. Any signal exceeding the slew rate (either by too high amplitude or a too fast rise) can cause an offset in the SQUID response by a factor $\xi n \phi_0$ during readout, i.e. a flux quantum loss. Thus after an event exceeding the slew rate the base line of the SQUID will be different (n in eq. 3.19 has changed). This has to be taken into account when stabilising the detector temperature via the SQUID base line (see section 3.5.2).

The SQUIDs used for CRESST are commercially available DC-SQUID systems. The SQUIDs are mounted in the liquid He bath; to have a low Johnson noise, the shunt resistors are thermally coupled to the mixing chamber. The constant current is supplied by floating current sources, and the electrical connections from SQUIDs to the detectors are twisted pairs of superconducting wires.

3.5 Data acquisition system

A scheme of the data acquisition system described below can be seen in fig. 3.9. The detectors are housed in the copper holders which rest thermally and electrically insulated from the copper base plate, inside the cold box (see Chap. 2). Each holder is weakly thermally linked to the mixing chamber with a copper wire to obtain a thermal relaxation time of a few hundred seconds. This design acts as a thermal low pass filter for temperature fluctuation of the mixing chamber. The mixing chamber reaches a base temperature T_B of 6 mK. A carbon resistor (speer) and a heating resistor are used to regulate the temperature T_B of the mixing chamber. The speer is read out with a four point measurement technique with an AC resistance bridge (LR 700), which regulates with a PID[1] temperature controller the power input into the heating resistor. Having up to four detectors to be operated at the same time the temperature T_B has to be set below the lowest operating point of all detectors. The holders are the temperature reference for the single detectors. The $4 \times 4 \times 4.1$ cm^2 sapphire crystals rest thermally insulated on plastic stubs in their copper housing. Thermal contact between the holder and the detector is provided by 20μ Au wires bonded between an Au pad in the middle of the W thermometer and the copper holder.

The electrical connection is established by superconducting Al wires bonded from Al pads on both ends of the thermometer to isolated contact pads on the holder. The superconducting wires connecting the thermometer to the readout circuit are then screwed to the contact pads to avoid radioactive solder. The constant bias current I_0 for the detector readout is provided by voltage controlled floating current sources. The current source can be adjusted either with a potentiometer or controlled with an externally provided voltage to create a step function used for measuring phase transitions (see section 3.5.1) . The ground

---

[1] Proportional Integral Differential

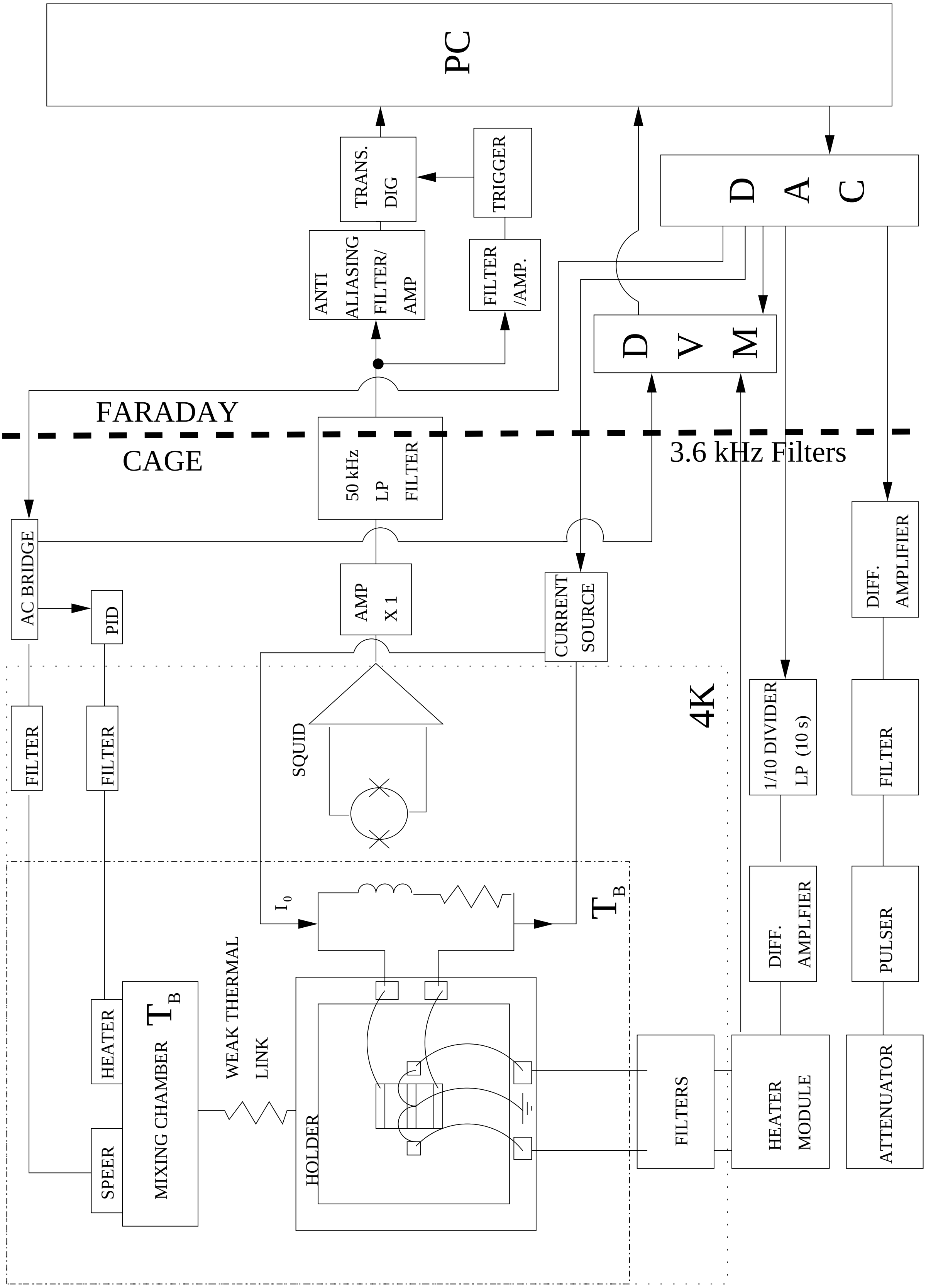

Figure 3.9: Block diagram of the data acquisition system (see text). The dashed-dotted line delimits the components working at the heat sink temperature T_B and the dotted line indicates the boundary of the cryostat.

connection of the readout circuit is given by the gold bonding wire which establishes the thermal connection. The SQUID sensors are located in the liquid helium bath at 4.2 K. The SQUID output signal is fed through a ×1 differential amplifier (resistance matching), leaves the Faraday cage through a 50kHz low-pass filter and is fanned into a trigger signal and the signal itself.

The trigger signal is shaped and AC-coupled to a trigger unit, which triggers the digitiser, while the signal first passes an anti-aliasing low pass filter (8 pole Bessel filter with cut-off at half the digitiser sampling frequency) and is then DC-coupled into the digitiser. For every triggered event the transient digitiser data is written to disk for off-line analysis, Chap. 4.1.

The time base is chosen such that on one side the full decay of the pulses of the slowest among the detectors is recorded, on the other side that a sufficient number of samples is taken during the rise of the signal. In the Dark Matter run (see Chap 4) a time base of 40μs was chosen, which provided about 20 samples in the rise time of the pulse. In every record the starting point of the pulse is set at one quarter of the record length ("pre-trigger" region). This region contains the value of the baseline of the SQUID; in the "post-trigger" region then the pulse is recorded. Each detector has its own independent trigger and data for each triggered event are written to disk. A dead time of $\sim$25 ms follows each trigger to allow time for the read-out and the next pre-trigger region. Pulses arriving within half of the post trigger region of the detector which triggered first are also recorded. The information about the time delay with respect to the first trigger is also provided, allowing an off-line study of coincident events (see 4.1.4).

Finally an Au wire bonded between small contact pads on the sapphire crystals (in the drawing 3.9 the little squares next to the thermometer) and the Au pad in the centre of the W thermometer serves as a heater to control the temperature of the detector and to inject electrical heater pulses (see section 3.5.3). In order to avoid cross-talk with the SQUID read-out circuit this heater is only in point-like contact with the thermometer via a bond spot. External connection with a heater module to the two small Al pads are used to apply a controlled voltage across the gold wire. This module consists of a summing amplifier followed by an analog square rooter and selectable resistors to define the heating current. Since the heating power depends on the square of the input current, the square rooter removes this dependence therefore linearising the relation. This is particularly important since the heater is used for stabilisation of the operating point and to send in test pulses. Without square rooter in fact the pulser energy would depend on the heating power offset. The applied heating power results from the sum of a constant contribution adjusted with a potentiometer on the heater module and an additional contribution regulated by a computer controlled Digital Analog Converter (DAC). The DAC output is provided by a software PID, the Control program. The voltage supplied via the potentiometer sets the coarse heating power for the chosen operating point and the control program stabilises the thermometer at the operating point. Test pulses with a rise time of 50 μs and a decay time of 500 μs are generated by a commercial Tail Pulse Module. The amplitude of the test pulses is controlled by an external voltage. This is created by the DAC in the data acquisition system, passed in the Faraday Cage via feed through filters and then decoupled from the ground of the acquisition system via a differential amplifier. A test pulser program set this voltage and then triggers the module at regular time intervals. To suppress the noise from the DAC it passes through 1/10 divider and a 10 s low pass filter. The signal fed into the differential amplifier, is filtered and then shaped with a tail pulse generator. Since one test pulse module generates the test pulses for all detectors, a pulse attenuator is used to adjust them according to the dynamic range and to the heater resistance of each detector.

3.5.1 Recording a transition curve

The performance of a cryogenic detector with SPT thermometer depends to a large extent on the shape of the transition curve, as mentioned in section 3.4. Since the bias current has a strong influence on the shape (the higher I_0 the less steep and often more linear the transition is), the first step for choosing a good operating point consists of recording transition curves for different bias currents. In fig. 3.7 the transition curves for different bias currents as function of PID output voltage are plotted. Given I_0 then the choice of a good operating point is a compromise between the need of having high sensitivity, which results from the steepness of the transition, and of a linear response. For this second step it is very useful to monitor the detector response to heater pulses of known injected amplitude in order to maximise the signal to noise ratio while checking that linearity of response is maintained over the widest possible energy range.

To record a transition curve means to measure the SQUID output for a fixed bias current I_0 as a function of the temperature around T_c (critical temperature). To avoid problems due to changes of the flux Quantum state of the SQUID, we switch the bias current from I_0 to$-I_0$ and take the half of the output step of the SQUID as the transition curve. The temperature sweep around T_c is controlled by fixing the heat sink temperature T_B and varying the heating current through the film heaters. T_B is chosen such that all four thermometers are in their superconducting phase just below the transition. The power through the heater is then swept up and down again around the T_c of each detector. An alternative way for a temperature sweep would be to vary the heat sink temperature via the bridge, having zero heating current through the film heaters. This would allow a simultaneous measurement of all transition curves and an absolute calibration of the temperature excursion caused by an energy deposition. However since the stabilisation of the detectors is done through the heater on the film, one would need to know what heating current a certain temperature corresponds to. Furthermore since the detectors have different T_c and are weakly linked to the mixing chamber (thus more subject to hysteresis phenomena on a short time scale) a measurement of the transition curve with the first method provides the information to choose a good operating point.

3.5.2 The control

Once the operating points have been chosen, each detector needs to be stabilised at this point independently. Since the SQUID output, i.e. the baseline, is also a measure of the temperature of the detector, this is the most sensitive measure for stabilisation. A software PID controller, the Control program, reads out baseline samples and regulates the voltage sent into the heater circuit. For the sapphire detectors the sampling rate was usually set at 0.2 Hz and the blocking time at 60 ms. If the time elapsed since the last trigger is less than the blocking time, it means that a pulse is occurring and the baseline sample is discarded. If the pulse exceeds the slew rate of the SQUID it can cause a so called flux quantum loss (see section 3.4.1). This results in a different SQUID output voltage for the same temperature and the computer might interpret it as a shift of the operating point and consequently regulating the heating power input definitively loosing the real operating point. It is however possible to overcome this problem via software since flux losses always cause an offset in the readout which is a multiple of ϕ_0. Therefore the control program compares the new sample with the old sample and if the difference is a multiple of ϕ_0 this jump in the baseline value is ignored.

3.5.3 The heater pulses

In order to achieve a long term stability and a full understanding of the detector performances, as required for a dark matter run, one needs to know the detector response function at any given time.

To monitor the detector response, heater pulses with the shape adjusted to create pulses similar to those of a particle interaction are sent at regular time intervals. Heater pulses of different pulse height covering the whole dynamic range are generated every 30 s. They are characterised by a rise time of about 20 μs and 1 ms decay time. This reproduces the non-thermal phonon behaviour.

The detector response function, i.e. the resulting pulse height as a function of the injected energy, is usually non linear. Heater pulses provide a means to extrapolate the calibration over the whole dynamic range as described in detail in Chap. 4.1.1.

Besides monitoring the stability and the energy calibration, heater pulses provide a measure of the trigger efficiency of each detector as function of the deposited energy. A relatively higher number of test pulses are injected near the detector threshold in order to be able to characterise the behaviour of the trigger efficiency, for example to determine by off-line analysis a threshold of 100% retention efficiency (see Chap. 4.1.2).

Since the sensitivity of a detector to low mass WIMPs strongly depends on the achieved threshold (see Chap. 1) the exact knowledge of the efficency is a crucial point for dark matter direct detection.

Chapter 4

CRESST Phase I: measurements and results

As outlined in Chap. 1 the main experimental requirement to be accomplished in a direct detection Dark Matter search are a low energy threshold, low background and high target mass. In this chapter measurements carried out in the Gran Sasso low-background facility (Chap. 2) with low energy threshold massive sapphire detectors are described. After an introduction to the data analysis methods, results of the first Gran Sasso measurements where a low background was achieved are presented.

In a Dark Matter experiment it is necessary to run the detectors in stable conditions over long periods of time (months). The attention is hence focused on the reliability of the calibration and monitoring methods used for CRESST which were studied with a dedicated run. Finally a very stable run characterised by a very low energy threshold which gave the best Dark Matter limits is presented. The energy spectrum measured in this run is discussed and used to derive limits on WIMP Dark Matter particles. As motivated throughout Chap.1 and in 3.3, sapphire detectors are especially sensitive for low-mass WIMPs with spin dependent interaction. CRESST Phase I results, presented here, improve existing limits in this region.

4.1 Data analysis

The data analysis for the CRESST experiment is completely performed off-line. Pulses exceeding a given threshold amplitude, are digitised and recorded to disk. Furthermore, as described in section 3.5, when more than one detector is operated, pulses occurring within half of the post trigger region of the first acquired pulse are recorded, together with the information about the time delay. .

In this section, the method developed to correctly evaluate the pulse height of the recorded pulses, which takes into account the non linear detector response, is presented. A reliable calibration procedure is then discussed, which extends the calibration performed with γ lines from a radioactive source down into the energy regions of interest for a Dark Matter search. Once the recorded spectrum is calibrated, the triggering efficiency down to very low energies and the energy threshold are precisely determined. Finally the monitoring of the stability of operation and correction for instabilities, and rejection criteria for spurious pulses are thoroughly discussed in the following paragraphs.

4.1.1 The calibration procedure

Pulse height evaluation

As a first step for a correct evaluation of the pulse height, each recorded pulse can be filtered in order to maximise its signal to noise ratio. There are several filtering methods. A rather simple algorithm is the so called moving average. Given a certain number of channels (chosen according to the time base and the length of the pulse) this algorithm calculates the average value among these channels and then moves the calculation by one channel at each step along the record. Then the pulse height is determined as the difference between the baseline value and the maximum value obtained after averaging. This simple method, quite quick and useful for a first look into the recorded pulses, is affected by two main problems. First if the noise superimposed on the pulse is rather high (as it is usually the case close to threshold), its height is overestimated. Second, near threshold this algorithm is not always able to correctly identify the pulse maximum. Since this is a crucial point to achieve a correct estimate of the energy threshold, a more accurate method is needed.

Another method superior in improving the signal to noise ratio, is the optimal filter (see [Pre93, Gat86]). However this method requires the signal shape to be independent of energy and both the signal and noise to be stationary in time. The signal should therefore obey a scaling law as [FF00]:

$$S = Ha(t) \tag{4.1}$$

where $a(t)$ describes an energy independent pulse shape and H is a factor proportional to the pulse height (or to its integral). Usually it is difficult to exactly match the shape of test and particle pulses. The test pulses are used to extrapolate the energy calibration from an energy which is high enough to pass the photons through the cold box to the energy range of interest for Dark Matter. In the case of non linear detector response, i.e. with pulse shapes changing with energy (as in the case for CRESST) the optimal filter spoils the extraction of pulse height as pulse shapes deviate from the averaged pulse used to construct the filter. Since non linearity is connected with the excursion on the transition curve, we need a method which reliably estimates the true pulse height independent of the signal shape. Therefore also in this case a more general method was considered for CRESST detectors.

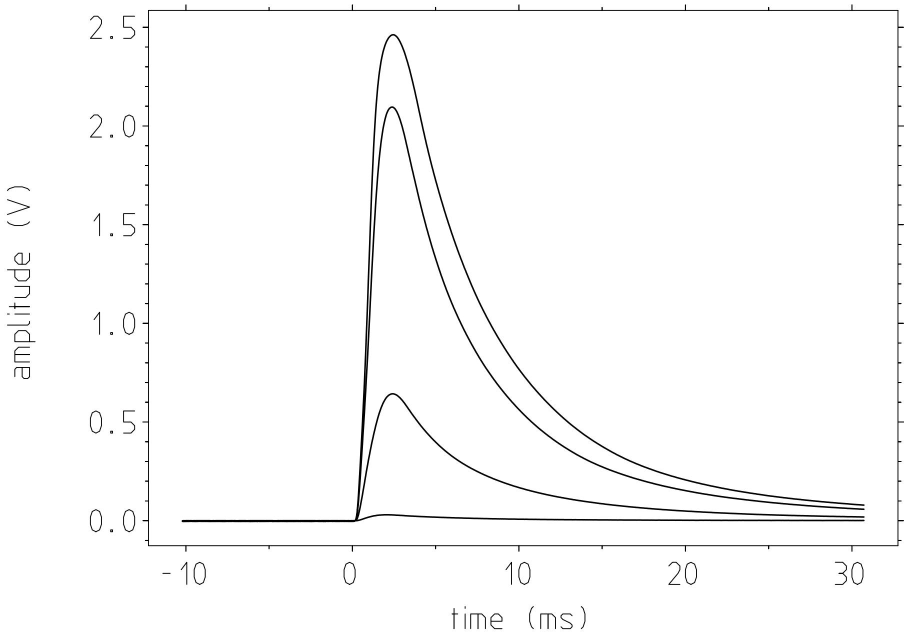

Figure 4.1: Heater Pulses templates of Run 17 (internal calibration run discussed in 4.2.4). The sequence shows the slight pulse shape changes with increasing injected voltage. The templates are obtained averaging recorded pulses for 0.2, 2, 6 and 8V injected amplitude respectively. The last heater pulse is at the end of the dynamic range and starts saturating.

The procedure elaborated for the sapphire detectors makes use of "template fits". In general this technique consists of selecting a set of pulses, for example from the calibration source, which are then averaged. The base line is then subtracted and the averaged signal is divided by its amplitude to arrive at a template for fitting all measured pulses. This method has several advantages. A fit gives more information about a pulse (not only its pulse-height) including the onset channel and the mean square deviation, therefore providing a tool to reject spurious pulses (see 4.1.3). Furthermore it avoids the bias of picking the highest point (due to noise fluctuations) of suitably filtered pulses, which systematically produce larger pulse amplitude values.

To overcome the problem of pulse shape changes with energy, heat pulses are used. As described in section 3.5.3, the test pulses are sent with a set of amplitudes throughout the entire dynamic range at regular time intervals. For each injected amplitude a separate template is made, averaging the recorded detector pulses as shown in fig. 4.1. The amplitudes of the test pulses are then determined by fitting them to the corresponding template. The calculated amplitudes are then plotted as a function of the injected energy (see fig. 4.3 and 4.4 in section 4.1.1) and fitted with a polynomial to provide an accurate detector response.

The calibration

CRESST sapphire detectors have been optimised to cover an energy interval ranging from a few hundred eV up to a maximum of about 200 keV.

To calibrate the energy scale a source is inserted via a removable plug in a machined channel through the bottom of the passive shielding. Via this channel a calibration with an external source can be carried out at any time during data taking without the need of opening the shielding or disturbing in any sense the set-up. The source is placed just below the cold box. The plate on which the detectors are mounted as well as the detectors holder are provided with holes to minimise the amount of material between source and detectors.

A ^{57}Co source is used for this purpose. This radioisotope has a half-life of 270.9 days and decays by electron capture to the stable isotope ^{57} Fe. As shown in fig. 4.2 this decay is characterised is by several gamma emission lines: 122 keV (85.6 % branching ratio), 136 keV (10.68 %) and 14.4 keV(9.16 %). The 122 and 136 keV lines are energetic enough to penetrate the cold box, while the 14.4 keV photons are fully absorbed.

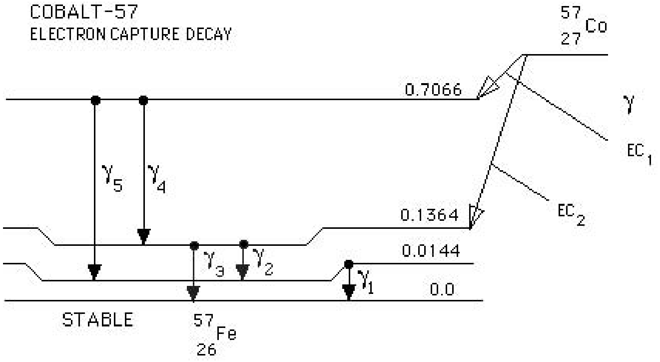

Figure 4.2: ^{57}Co decay scheme.

Together with the source also heat pulses of different amplitudes adjusted to cover the whole acquired spectrum are injected into the thermometer, as described in section 3.5.3. The heat pulses are distributed over the whole spectrum. Their amplitude is determined as described in the previous subsection and then plotted as a function of the injected voltage. As shown in fig. 4.3 a fit of these values with a polynomial function determines then the detector response over the whole dynamic range.

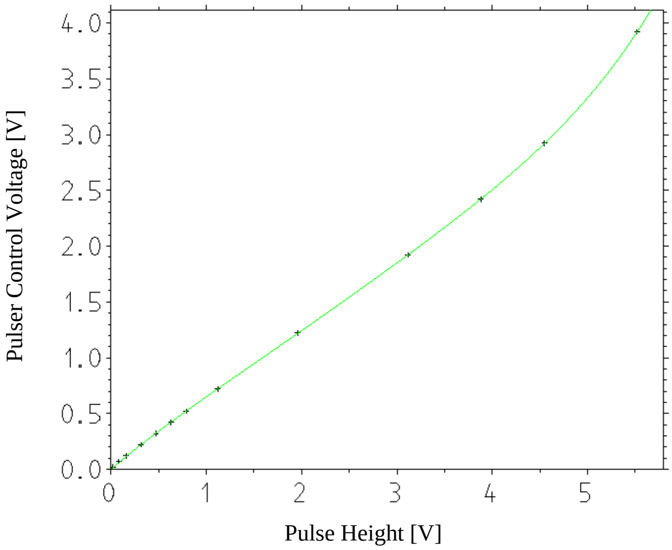

Figure 4.3: Example of an amplitude response function of a Sapphire detector. On the x axis the pulse-height of detector signals determined with a template fit is given while on the y-axis the pulser control voltage is plotted, which is proportional to the injected energy.

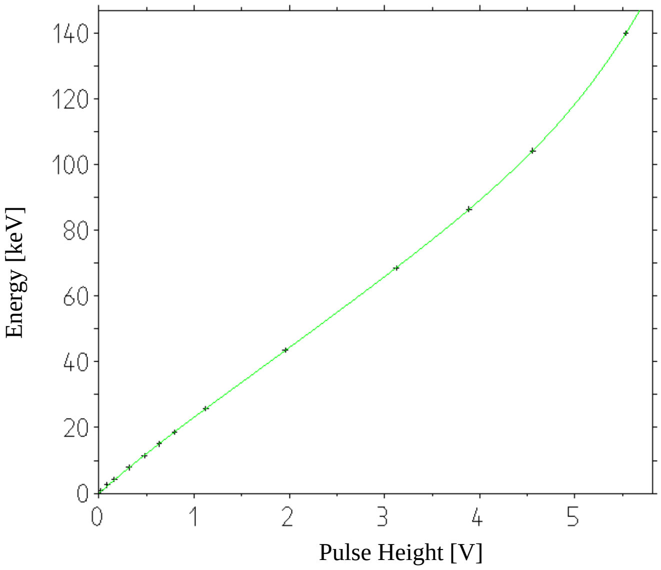

Figure 4.4: Response function of fig. 4.3 in terms of equivalent γ energy. On the x-axis again the pulse height of detector signals is given while the y-axis is now converted to energy. The scale factor between pulser control voltage and γ energy was determined by comparing the amplitudes of 122 keV pulses with that of neighbouring heater pulses.

A template is constructed by averaging pulses from the 122 keV peak. The measured pulse height associated to this emission line is determined fitting the pulses to this template. A comparison of the pulse heights from the 122 keV line and the neighbouring heater pulses provides an absolute calibration of the test pulses in terms of equivalent γ energy. In fig. 4.4 the same response function of 4.3 is plotted as a function of the deposited energy.

Once the response function is known, the energy of any particle pulse can be determined. Again the template fit procedure is used. The response function is used to convert the 122 keV template into energy in each time bin. For the particle events in the background measurements, the response function obtained in the calibration measurement is again used to convert the recorded events to energy in each time bin. After this procedure the obtained pulse shape is independent of energy, i.e. they are now linearised. In this case then the pulse amplitude provides directly the information about its energy, as shown in fig. 4.5. The energy can thus be determined by fitting a single similarly converted template (the 122 keV template from the calibration measurement) to the linearised pulses. Since in this case the pulses fulfil the requirement from the formula 4.1, the optimal filter technique can be also applied. The optimal filter is constructed using the linearised template from the calibration and randomly sampled baseline noise. This last method slightly may improve the energy resolution when compared to template fitting without introducing energy bias [Ang02b]. This way the source

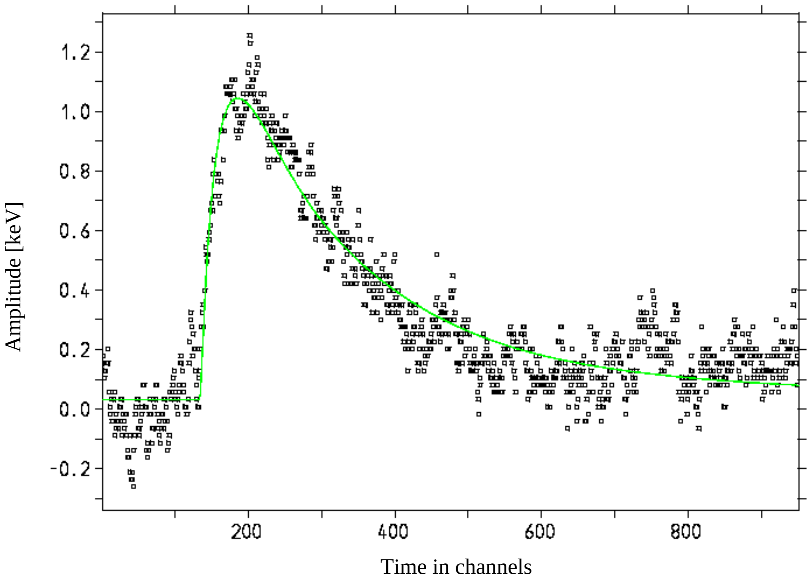

Figure 4.5: Example of fit of a low energy pulse (~1 keV) using a linearised template constructed by averaging pulses of the 122 keV emission line from a calibration source. Both the template and the pulse are converted into energy before fitting, using the procedure described in the text.

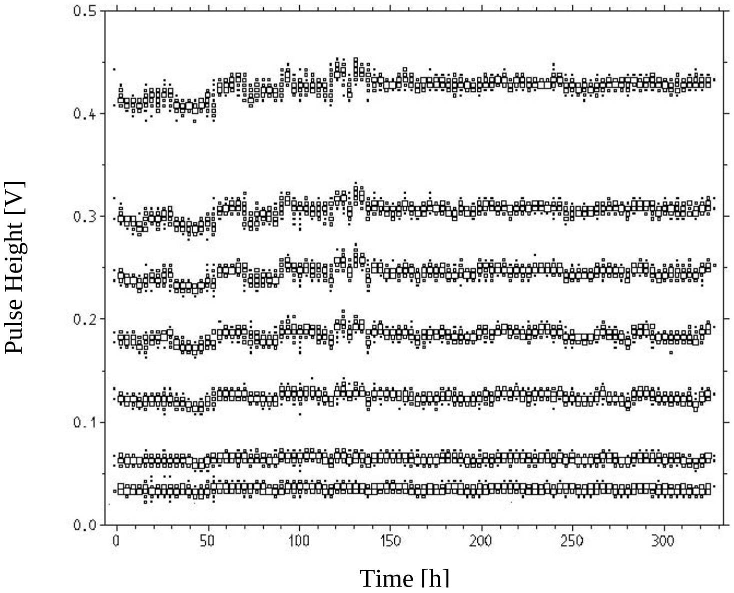

Figure 4.6: Heat pulses amplitudes over time.

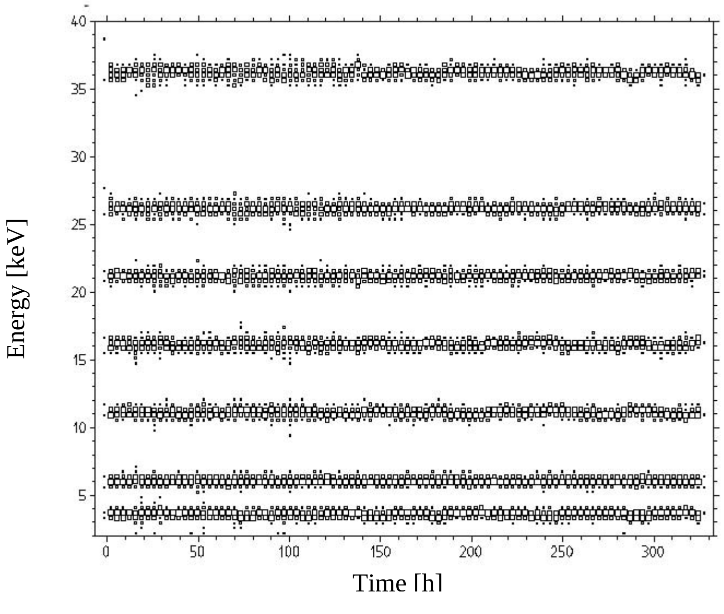

Figure 4.7: Heat pulses of figure 4.6 are here converted to energy and again plotted over time. Drifts due to changes of the operating point have disappeared.

provides the information about the energy scale while the heat pulses allow the extrapolation of the calibration to the whole dynamic range. A calibration of the whole spectrum is now obtained.

Heat pulses are also a powerful tool to recognise temperature drifts and correct for them. In case of a change of the operating point, the measured pulse height for a given injected voltage would consequently change as well. Therefore, once the source is removed, test pulses are constantly injected in order to monitor the detector operation. In fig. 4.6 the amplitude of several test pulses is plotted over time and the consequences of temperature drifts are shown. Due to the linear relation between energy and the pulser control voltage, these pulse-height changes provide the information for adjusting the coefficient of the response function. In figure 4.7 the same test pulses of the previous plot are now converted to energy and again plotted over time. Any fluctuation due to a drift of the operating point has disappeared.

In a Dark Matter run the calibration with a source is always done after all operating condition have been settled. Heat pulses are always injected, both with and without calibration source, during the whole run. Any time a slight change is implemented a new calibration is carried out. Usually the calibration is repeated at the end of the run to confirm the stability of detector operation.

Correction for pulser non-linearities

The calibration method described so far assumes that the pulser module is ideal, i.e. not affected by any offset and perfectly linear. In order to study and hence to avoid any systematic of this type, the actual heating power injected into the thermometer was monitored. As described in 3.5 the voltage amplitudes of the test pulses are set via software and sent through the DAC (see fig. 3.9) to the pulser module which generates the pulses. A heater module adds these pulses to the heating needed for stabilising the operating point and takes the square root of this sum. The output of the square rooter which is then fed to the detector is also recorded with the transient digitiser.

This set-up allows the detection of any possible pulser non-linearity. The energy ΔE injected by a heater pulse is then determined from the recorded heater voltage $U_H(t)$

$$E_{true} = \alpha \int_0^t U_H^2(t) - U_0^2 \tag{4.2}$$

U_0 is the constant voltage needed for stabilising the operating point onto which the heater pulse is superimposed. U_0 is determined from the pre-trigger range and α is a proportionality constant obtained calibrating with the 122 keV peak. The expected or linear energy is instead given by

$$E_{lin} = \frac{E}{V} A_{inj} \tag{4.3}$$

where E/V is the Energy scale factor per pulser control voltage determined from the calibration procedure and A_{inj} is the control voltage amplitude. To correct for any deviation of the actual injected energy from the nominal value the recorded output from the square rooter is used. Finally the difference $\Delta E = E_{true} - E_{lin}$ between the actual and the nominal energy for each test pulse value is obtained. The results are averaged and fitted as shown in fig. 4.8. This plot accounts for the pulser non-linearities, i.e. for the energy correction of the injected energy. As a final step this correction is included in the response function as obtained from the calibration, and the correct energy spectrum is obtained. The whole procedure of pulse height evaluation, calibration and correction for pulser non linearities has been checked with a dedicated run as will be described in 4.2.4.

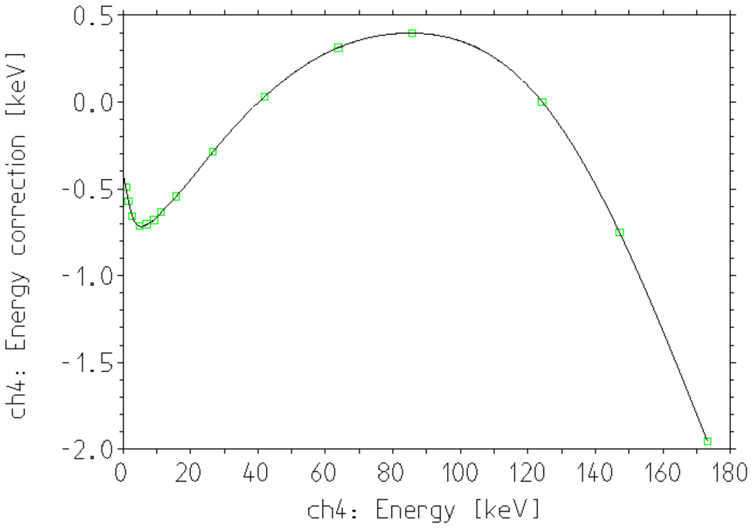

Figure 4.8: Results of pulser monitoring. Once the difference between the nominal and actual injected energy (see text) is calculated, the obtained values are averaged and fitted as function of the energy. The energy correction function is thus determined.

4.1.2 Software threshold and trigger efficiency

Another crucial point for a correct interpretation of the acquired spectrum in a Dark Matter analysis is the trigger efficiency. Again the heat pulses are essential to properly study it. In fact with the injection of several heat pulses with decreasing amplitudes down to threshold it is possible to study their retention efficiency and thus to know how many particle pulses may be lost at a certain energy. Knowing the number of injected pulses, the number of acquired test pulses defines the retention efficiency at that energy.

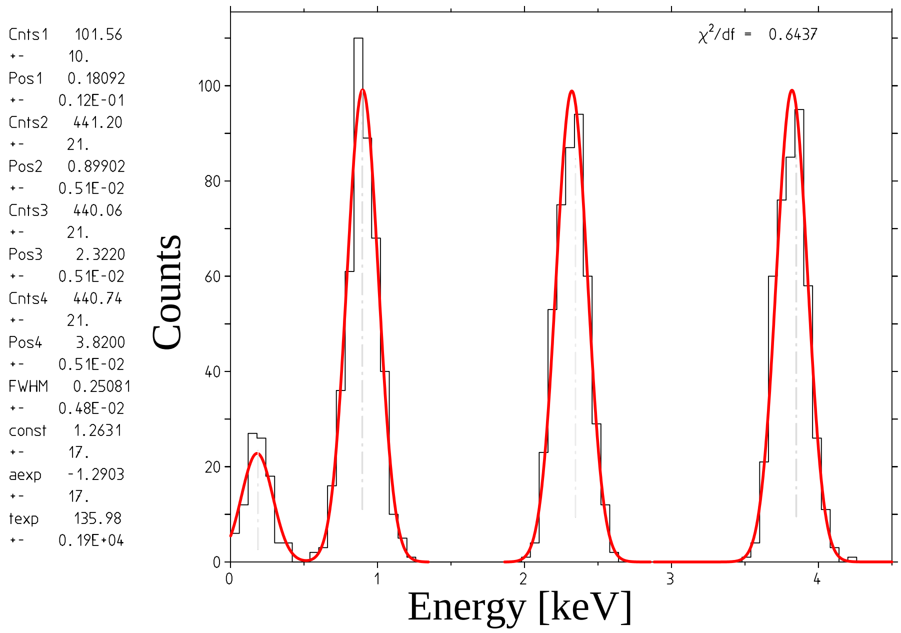

Figure 4.9: Acquired test pulses for four discrete injected energies. In the first peak (run 20, Chap.5) only 100 out of 440 pulses are seen. The second peak at 0.9 ± 0.05 keV shows 100% triggering efficiency. Therefore a software threshold of 1 keV with 100% triggering efficiency can be safely applied here.

To extract the Dark Matter limit a conservative approach has been adopted, setting a software threshold such that the retention efficiency at threshold is 100%. An example of this procedure is shown in fig. 4.9.

4.1.3 Rejection of spurious pulses

In a rare event search it is necessary to minimise or (when possible) eliminate all contributions to the acquired energy spectrum which are not due to the sought signals. Therefore a method able to distinguish particle events from spurious pulses and to discard them retaining all the good ones or strictly knowing the retention efficiency has to be developed.

Particle events are expected to have a time independent and Poissonian distribution. In fig. 4.10 all acquired data from the Dark Matter run (see also section 4.2.3) with neither cuts nor software threshold applied are plotted as a function of time. At least two bursts of event can be recognised here, the first after about 17 hours measuring time and the latter after 85 hours. They are irregularly distributed over time and have a counting rate excess up to four times the mean value. These types of events can be generated by mechanical vibrations or electronic noise on the baseline. In figure 4.11 typical events taken from the

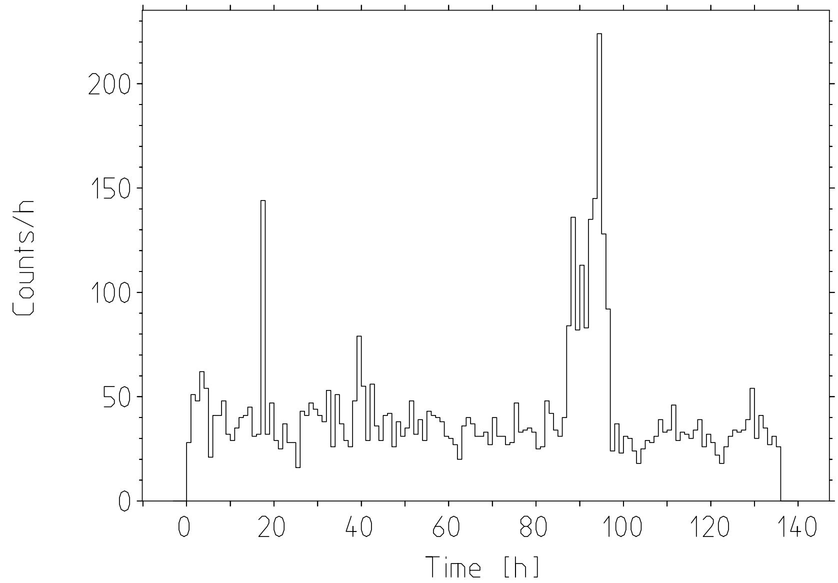

Figure 4.10: Run 16: event rate as a function of time before setting any software threshold or cuts.

first and the second bursts respectively are shown. These noise events lead to an undesired enhancement of the count rate close to threshold, which is particular disturbing when seeking for dark matter signals.

There are several ways to deal with these events. The most direct one would be not to consider measuring time records containing these bursts. However, besides a loss of measuring time, this method is not rigorously justifiable. An alternative is to apply a time filtering method [Bau99]. In this case the complete

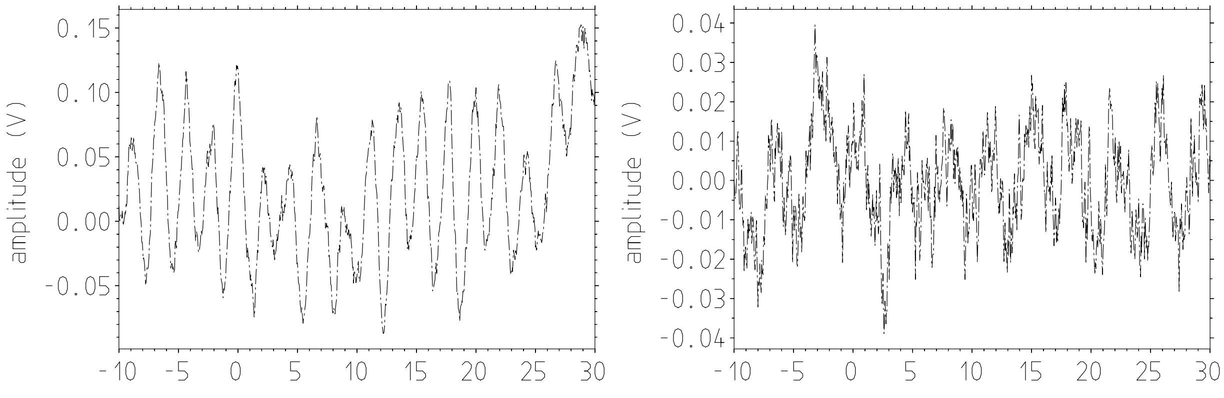

Figure 4.11: Example of noise events. The event on the left is a typical event from the first burst in the time distribution, while on the right an event from the second one is shown.

measuring time is divided into chosen time intervals (here for example 30 minutes) and the probability for N events to occur into one time interval is computed for the whole energy spectrum. The physical event distribution is Poissonian and the noise events lie far from its mean value. In fig. 4.12 the distribution per 30 min intervals of the uncut data shown in 4.10 is given. The cut is then set at

$$N =< n > +3\sigma \tag{4.4}$$

three standard deviation from the mean value $< n >$ of the Poisson distribution.

The method used to analyse the CRESST Phase I results rely exclusively on Pulse Shape Discrimination (PSD) and removal of coincident events (see next subsection). In CRESST Phase I detector nuclear recoil events and radioactive background are indistinguishable both in shape and in amplitude, given the same deposited energy. Therefore the γ radiation emitted by the radioactive source can be successfully used to calibrate a PSD method against noise events. The template fit as described in 4.1.1 provides a powerful method to discard spurious pulses. From the calibration source, good events are selected either from the 122 keV peak or from the Compton edge region usually choosing pulses from 35 to 40 keV (the Compton edge nominal value for ^{57}Co is 39.46 keV).

For each fitted pulse the deviation of its shape to that of the template is calculated and the value of the square root of the mean squared deviation, the RMS value, is obtained. Hence, plotting the logarithm of the RMS value over

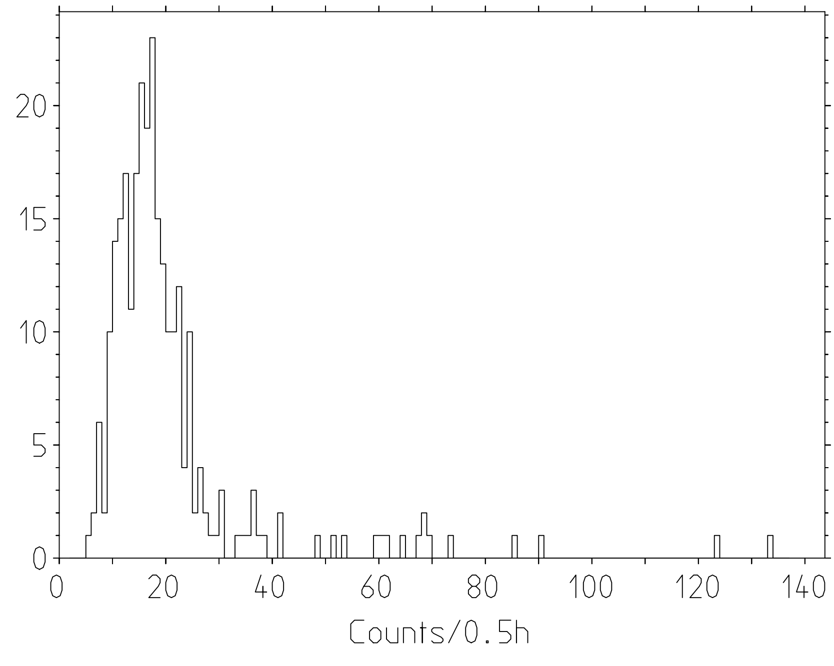

Figure 4.12: Distribution of the number of counts per 30 min intervals for the uncut data of fig. 4.10.

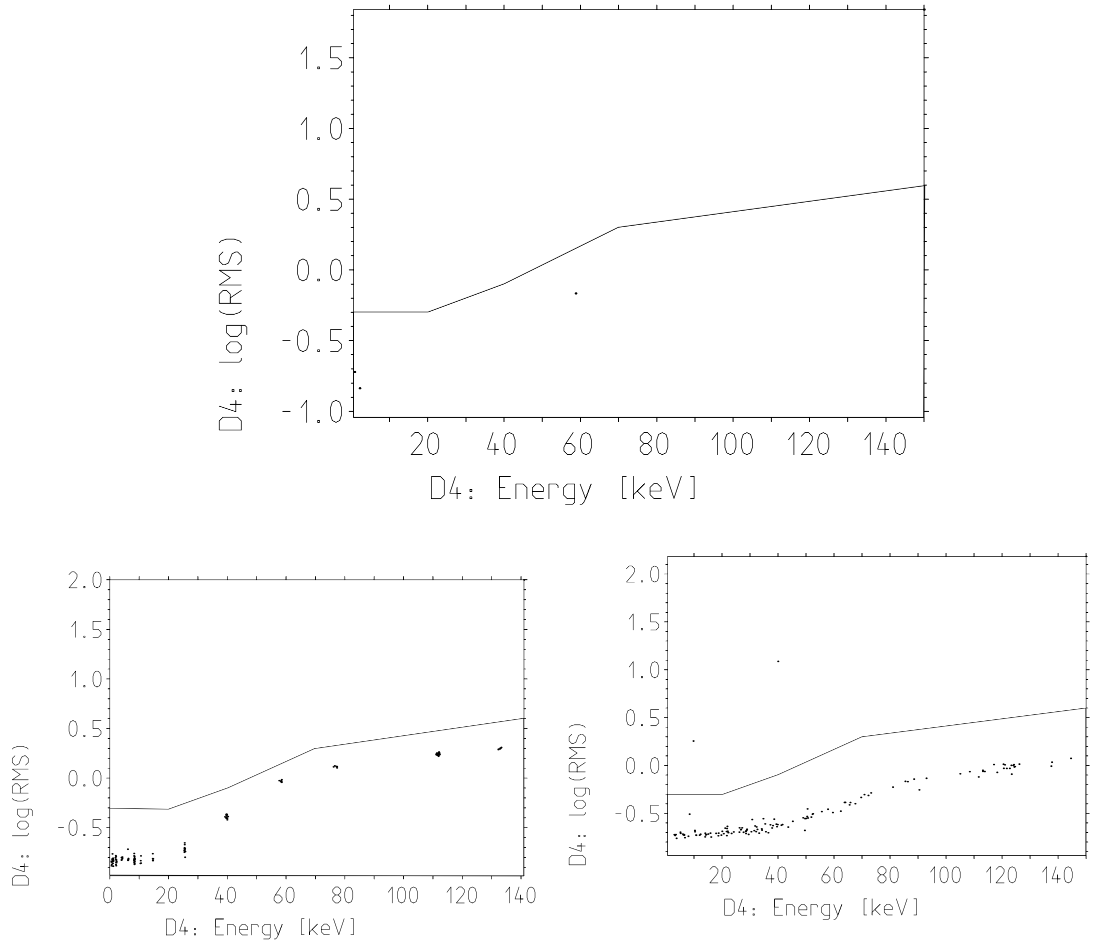

Figure 4.13: Logarithm of the RMS value as a function of the energy. The solid line indicates the RMS cut applied in run 16 (Dark Matter run). The event lying above this line show a distorted pulse shape as in the case of noise events or of saturated pulses. The efficiency of this cut was tested with heater pulses, resulting in only 1 out of 1032 of the 580 eV pulses being discarded (lower left figure). The same cut was applied also to the calibration measurement (lower right figure) showing that only 0.22% of the events were discarded.

the energy, a figure as shown in 4.13 is obtained. Events that lie far away from the resulting band can be discarded. To calibrate the retention efficiency, exactly the same cut is applied to both the calibration run and the test pulses.

After applying a software threshold and a proper RMS cut the same data set of figure 4.10 is now shown in fig. 4.14. On the left side the event rate is plotted in function of time and on the right side their Poissonian behaviour is shown.

To extract Dark Matter limits a very conservative RMS cut has been applied such that the retention efficiency was 100% over the whole range.

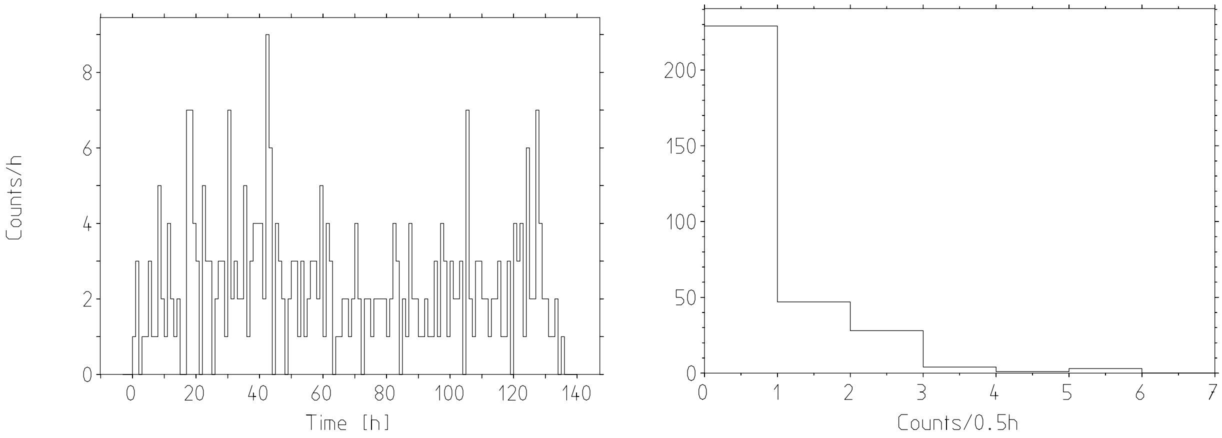

Figure 4.14: Left: rate as a function of time of the same set of data shown in fig 4.10 after applying a software threshold and the RMS cut. Since the detector was triggering in the noise, the main reduction of the mean count rate is due to the applied threshold. On the right the distribution of these events per 30 min intervals is shown.

4.1.4 Rejection of coincident background pulses

In Dark Matter detection experiments the presence of radioactive background counts is one of the most severe limiting factors. In CRESST Phase I using sapphire detectors there are no means to distinguish in a given detector a nuclear recoil event due to neutrons or WIMPs from an electron recoil event due to the presence of radioactive contaminants. However, since WIMP interaction cross sections are extremely small, they have a probability compatible with zero to induce coincident events in two or more sapphire detectors. Therefore WIMP events are expected to be in anti-coincidence with any other detector and time correlations between pulses originating in different detectors are considered for a possible reduction of the background. Besides, coincident events deposit only a ratio of their energy in each triggering detector thus contributing to the continuum of the spectrum, while the information relevant to the identification of their source is contained in the sum of the deposited energy in all coincident detectors. As a consequence all these events can be removed without subtracting any information relevant to dark matter and then be separately analysed for a better understanding of the background.

As described in 3.5 all events which trigger within half of the post trigger region from the first are recorded. In order to avoid discarding random coincidences the time difference distribution is studied. As shown in fig 4.15 a clear coincidence peak appears due to the “true” coincident events. The events from this peak are then selected and discarded, thus retaining practically all events which may have happened to be randomly coincident.

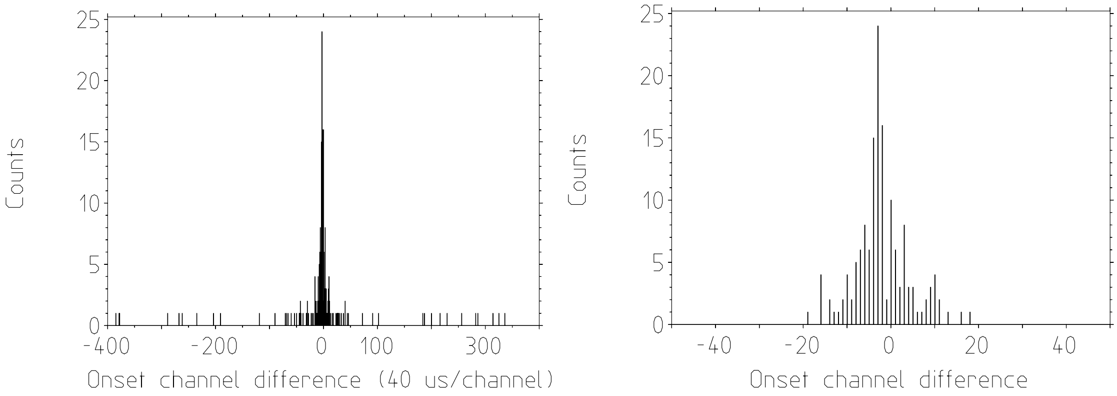

Figure 4.15: Coincident events from Run 16 (Dark Matter run). On the left side the time difference distribution (here as pulse onset channel difference) is shown. On the right side the peak selected for removing true coincidences thus still retaining random ones is blown up. It is characterised by a FWHM of about 0.4 ms and long tails (10 channels) extending to about 4 ms for very low detected energies. The cut is set at ±4 ms.

4.2 Measurements and results

4.2.1 The early problem of spurious counts

During 1999 a first series of measurement with four $4 \times 4 \times 4.1$ cm^3 crystals in low background conditions were performed. The detectors were mounted as explained in 2.2 inside the cold box facing each other with no material in between. However the measured rate was much higher than expected as shown in fig. 4.16. Its time-dependent non Poissonian behaviour clearly showed that its origin could not be attributed to radioactivity. Besides this, the absence of any true time coincidences between any of the detectors confirmed this statement. In a further run the possibility of electromagnetic interference which might heat the thermometer creating thermal signals similar in shape to particle pulses was exploited. The readout system of one detector was modified to improve the immunity to electromagnetic interferences. Electromagnetic disturbances created on purpose inside the Faraday cage showed that the detector was immune to any interference, however still providing an unchanged high count-rate.

To further investigate the origin of this count-rate, a so called "double detector" [Mei99], was implemented. As shown in fig. 4.17 it consists of a crystal with two thermometers on one surface. As a result it was found that signals detected from the two thermometers were coincident in time and they were both seeing the same energy deposition, while these signals were not coincident with the other detectors. This meant that the signals could only be due to high frequency phonons created inside the sapphire, thus excluding an external origin.

Finally, microscopic cracks in the sapphire crystals at the contact points where

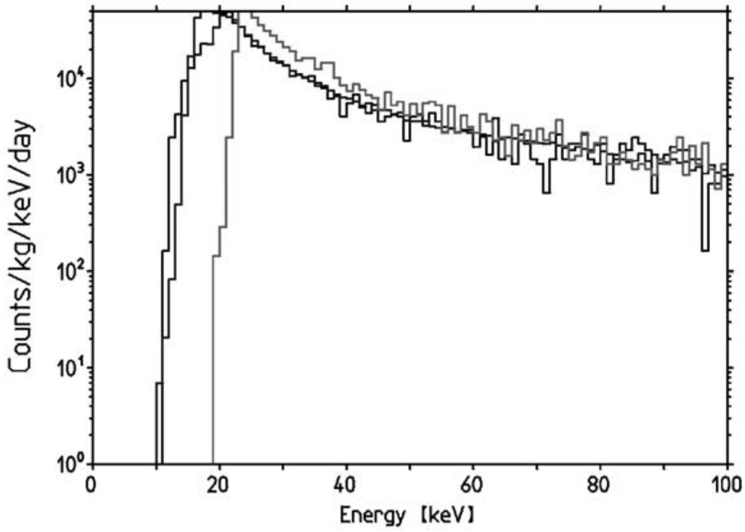

Figure 4.16: First measured spectrum in low back-ground conditions: the count rate is much higher than expected, time-dependent and non Poissonian, i.e. not caused by radioactivity.

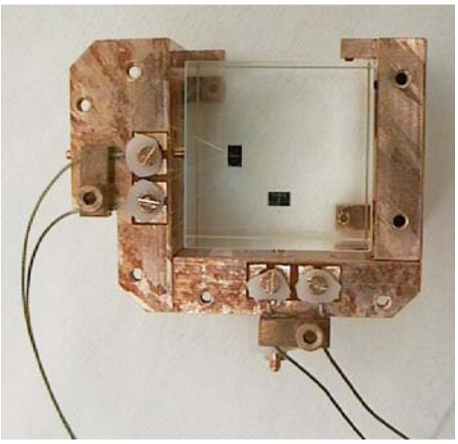

Figure 4.17: Double detector: two tungsten films are structured onto the crystal surface.

the sapphire balls support the crystal in its holder, as shown in fig. 4.18, were recognised. This led to identification of the origin of the background with structural relaxation in the crystal. Due to the almost point like contact area with the sapphire spheres, an excessive pressure was applied to these points to hold the crystal tight in their housing thus avoiding vibrations. Therefore in spring 2000, plastic stubs were used to replace the sapphire. Despite their larger contact area, they did not lead to any detectable loss of sensitivity, while the spurious background completely disappeared as will be described in the next subsection.

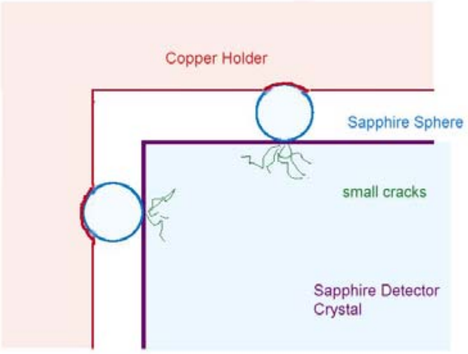

Figure 4.18: The old holding design of a sapphire crystal into the copper housing was provided by sapphire balls. These were meant to minimise the contact area in order not to cause any loss of sensitivity. However, the large pressure resulting from the force needed to tightly hold the crystals created microscopic cracks at the contact area. The structural relaxation was creating high frequency phonons producing the spurious background.

4.2.2 Run 15: a low count-rate long term run

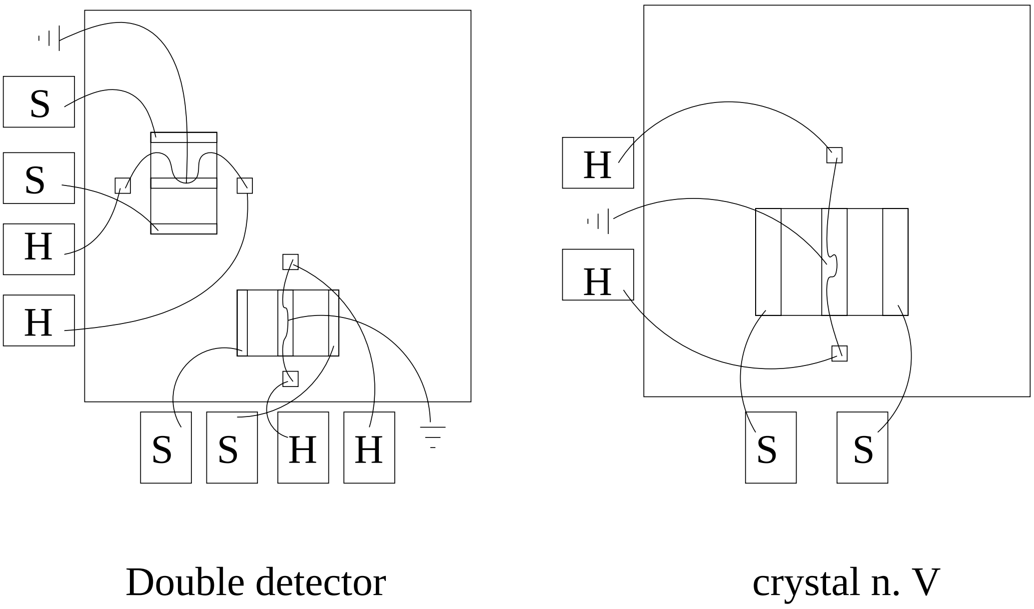

Figure 4.19: Bonding scheme for electrical and thermal connections of the two crystal implemented in Run 15.

In this run only three read-out channels were working : Ch1, 2 and 4. The SQUID read-out system for Ch. 3 is not working. The set-up is as follows:

- Crystal nr. V (see table) mounted in holder nr. V. Connected to read-out channel 1.
- Crystal nr. X, called “double” detector in holder nr. II is connected to the readout channels 2 and 4.

	Crystal V	Crystal X (double detector)
Distributor	Dörer Elektroptik Ettlinger Str. 5 76307 Karlsbad	BEC Breznikar Consulting GMBH Franz Haniel Str. 82 47443 Moers
Manufacturer	Crystal Systems Inc. Shetland Industrial Park 27 Congress Street Salem, Massachussets 01970	SCT Single Crystal Technology BV Ir. Schiffstraat 220 NL-7547 RD Endeschede
Material	Al_2O_3	Al_2O_3
Mass	262 g	262 g
Dimensions	$40{\times}40 \times 41$ mm^3	$40{\times}40 \times 41$ mm^3
Surface	2 r-plane epi-polished 4 sides optically polished	2 r-plane epi-polished 4 sides optically polished
W film evaporation	550° crystal temperature substrate heating power: 396A/2.57V÷374A/2.4V $8 \div 3.6 \times 10^{-8}$ mbar rate of deposition: 2 Å/s film thickness: 1900 Å	500° crystal temperature 423A/2.9V÷360A/2.3V $1 \times 10^{-8} \div 3 \times 10^{-9}$ mbar rate of deposition: 2.3 Å/s film thickness: 2000 Å
W thermometer size	8×9mm^2	2 thermometers 3×5mm^2

Table 4.1: Run 15: Crystal description [Mei99].

The schemes for electrical and thermal connections are shown in fig. 4.19. As described in section 3.5 the Au wire stitch bonded on the central Au pad serves as heater, while thermal contact as well as grounding is provided by a 20 μm Au wire bonded directly to the copper holder. The electrical connection is provided by Al wires bonded from Al pads on the thermometer to the SQUID contact pads. On the holder, electrically isolated Cu-Kapton-Cu pads are used.

The mixing chamber was stabilised at 30 kΩ corresponding to a temperature of about 5 mK. After recording transition curves for several bias currents for all detectors (as shown in fig. 4.20 for readout channel 1), bias currents of 4.4, 11 and 26 μA were chosen for channel 1, 2 and 4 respectively.

Ch4, characterised by a very small transition, proved to be very insensitive and with a rather low signal to noise ratio. Several attempts were performed to

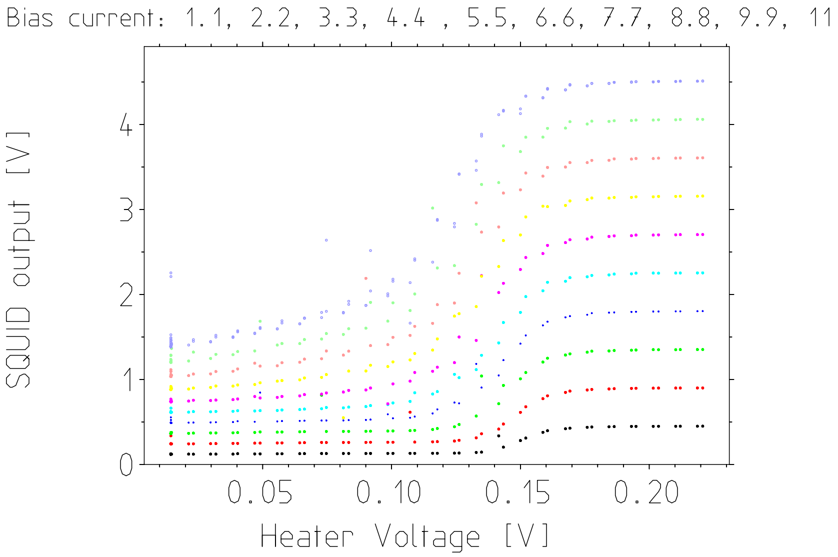

Figure 4.20: Run 15: transition curves of channel 1 for different bias current from 1.1 to 11 μA as indicated in the header on the plot.

improve its response and it was finally operated with 400 μA bias current. The achieved threshold for this channel was however about 5 keV and will not be further discussed.

Calibration

A ^{57}Co was used to calibrate the detectors (see section 4.1.1) and the method described in section 4.1.1 using standard event templates for each injected voltage amplitude was applied to determine the test pulses height. For the particle pulses a standard event was obtained by averaging pulses from the 122 keV emission line of the ^{57}Co source. The obtained response function before and after conversion to energy is shown in fig. 4.21 for both ch1 and ch2. After conversion to energy the fit of the 122 keV emission line gives the results shown in fig. (4.22). As can be observed in this figure the energy resolution is worse than expected due to an asymmetric broadening of the peak to the left side. This effect is not yet clearly understood but it is very likely that it depends on crystal properties.

The calibrated response function was then used to linearise the standard event template from the 122 keV in each time bin. This linearised template was then used to fit again all pulses in order to avoid distortion due to the changing of pulse shapes from the 122 keV energy template towards the lower energies.

A check of the calibration down to lower energy was performed as suggested in [Sis99] selecting events which are coincident in the two detectors. As results from fig. 4.23 two bands corresponding to a total energy deposition 122 keV and

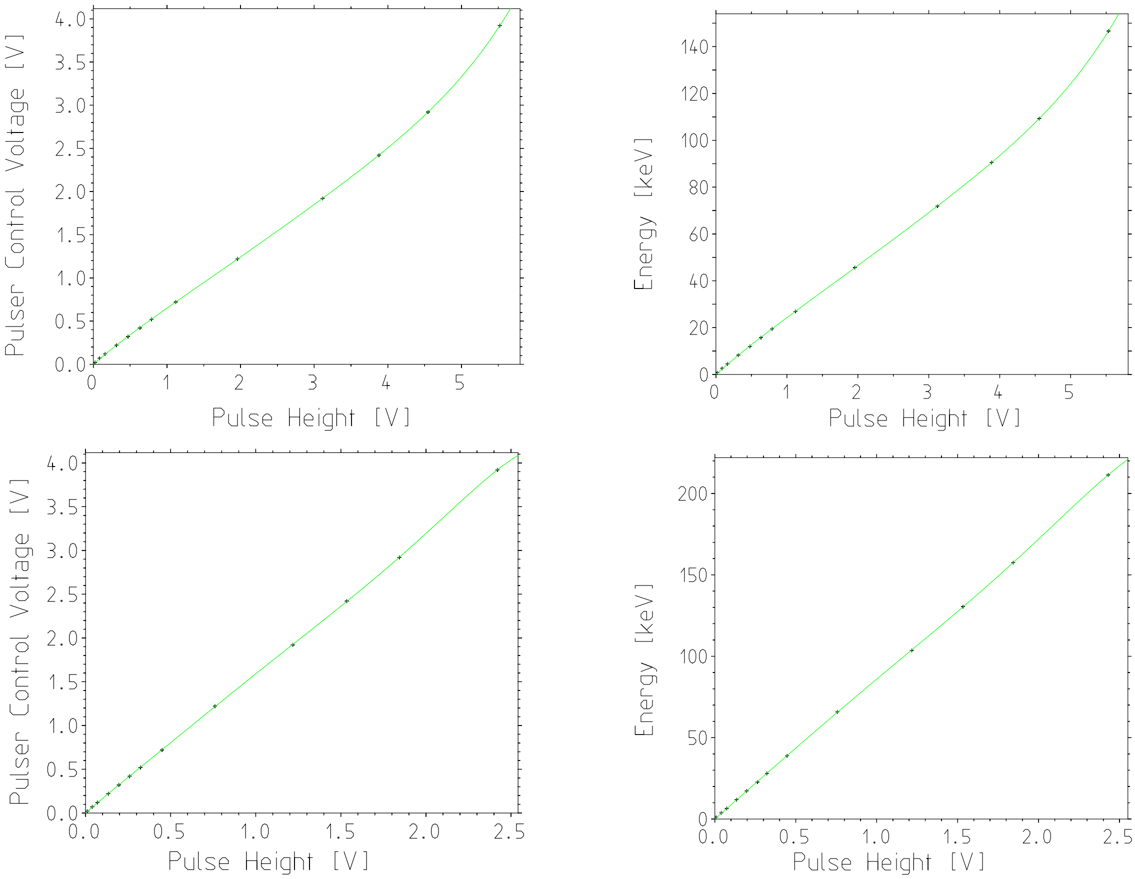

Figure 4.21: Run 15: Polynomial fits of the response function of pulser control voltage amplitude over pulse height in channels on the left side and after the conversion to energy on the right side for both ch 1 (upper figures) and ch2 (lower figures).

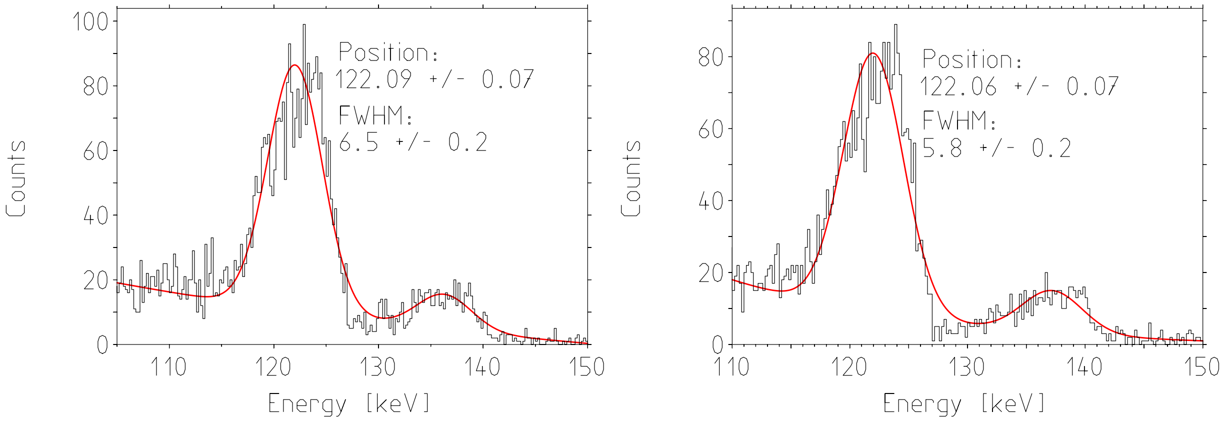

Figure 4.22: Run 15: fits of the 122 keV emission line after conversion to energy for channels 1 and 2.

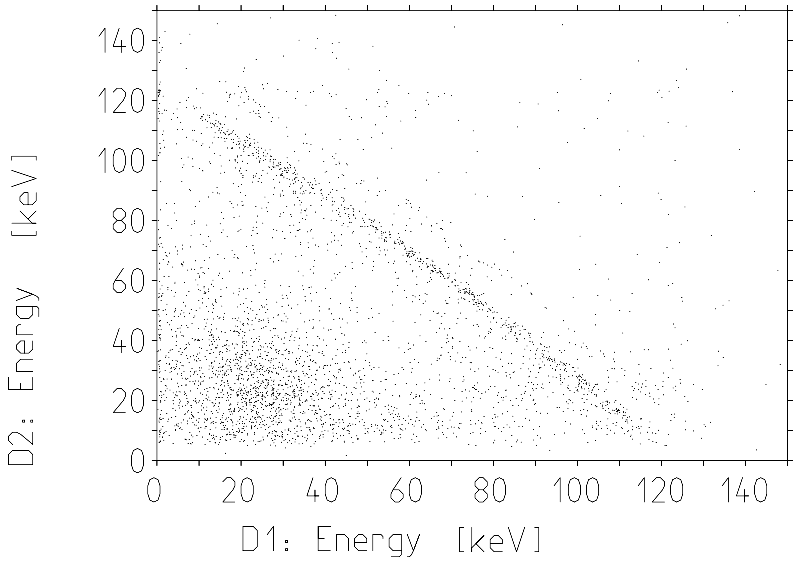

Figure 4.23: Run 15 ^{57}Co calibration: plot of the coincidence events between the two detector. On the axis the energy of channel 1 (x) and channel 2 (y) obtained by fitting converted pulses with a linearised standard event template are plotted. In this run the pulser non-linearities were not taken into account (see the discussion in the results section).

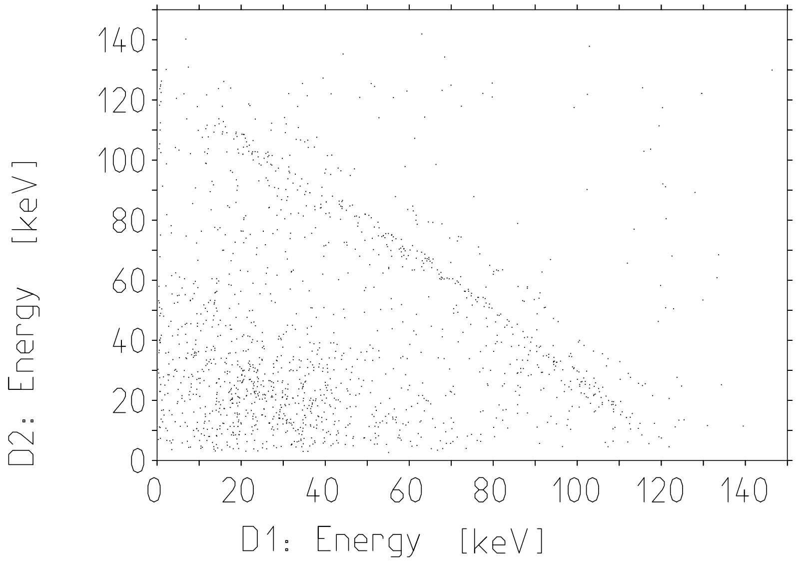

Figure 4.24: ^{57}Co calibration performed at the end of run 15. As in fig. 4.23 the plot of the coincidence events between the two detectors is shown, the method used here to calibrate this measurement is exactly the same as the one applied to the background measurement.

136 keV are visible. Any error in the extrapolation of the energy calibration via the heater pulses would result in a distortion of these bands from a straight line. Due to the geometrical arrangement of the detectors in the cryostat, this method allows to probe the energy calibration between $\sim 10 \div 112$ keV (see [Sis99]). In this plot in particular the gap in the low energy range is due to the relatively high threshold set during this recording time for channel two to avoid an excessive high rate.

After removing the source the response function is constantly monitored via injecting heat pulses (see section 3.5). Again their pulse height is determined via fitting each of them to its template. The conversion factor from pulser control voltage to energy determined with the calibration is applied. The response function is then used to convert particle pulses in each time bin and their energy is determined by fitting them with the linearised template from the calibration source. A check of this method within this run was performed applying it to a calibration measurement acquired at the end of the run. In fig. 4.24 the resulting plot of the coincident event as function of channel 1 and 2 energies is shown.

Results

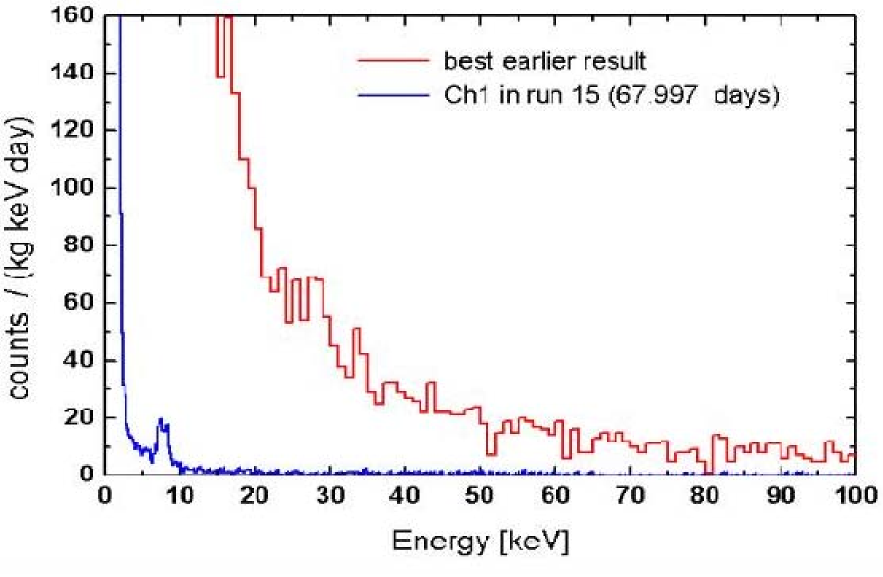

Figure 4.25: Comparison between run 15 energy spectrum and the best earlier result before substituting sapphire balls with plastic stubs for holding the sapphire in their copper housing.

Run 15 was the longest of CRESST Phase I lasting about three months acquiring $\sim$ 15 kg days of data. As introduced in section 4.2.1 and shown in fig. 4.25 it was the first run after the background problem due to crack formation had

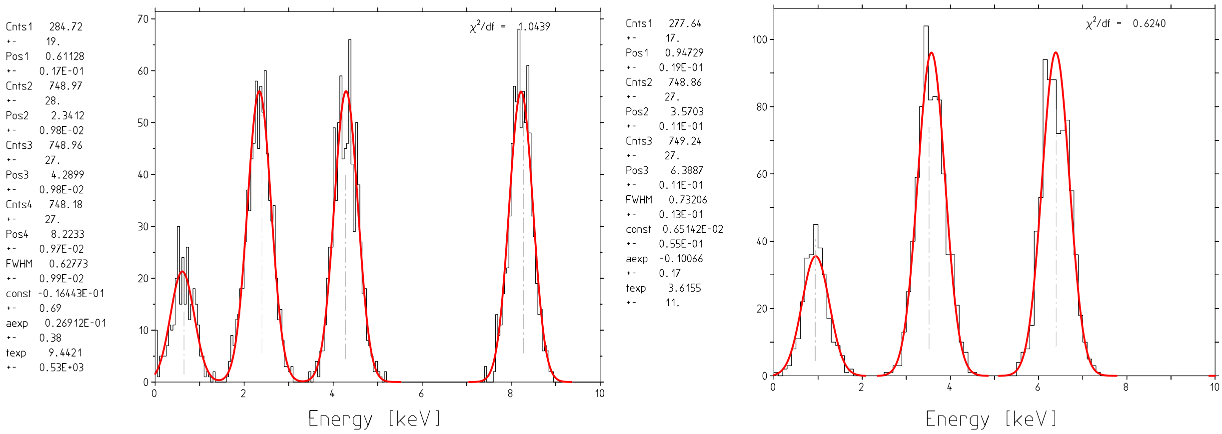

Figure 4.26: Test pulses (counts) for several injected discrete energies for channel 1 (left) and channel 2 (right). Ch. 1 triggers 100% efficient at 2.3 keV The energy resolution of channel 1 at 2.3 keV is of 600 eV. Ch. 2 triggers 100% efficient at 3.5 keV. The resolution is about 700 eV at this energy.

been solved. However, as will be shown hereafter, the achieved threshold was not yet optimal to extract Dark Matter results. Nevertheless this run was very important to successfully demonstrate the long-term stability and reliability of the CRESST set-up. Furthermore it enabled the development of analysis methods that were discussed in section 4.1 to properly understand the acquired spectrum. This study identified also a systematic error in the energy calibration due to pulser non linearities (4.1.1) which was taken into account in the subsequent Run 16 used to set Phase I Dark Matter limits.

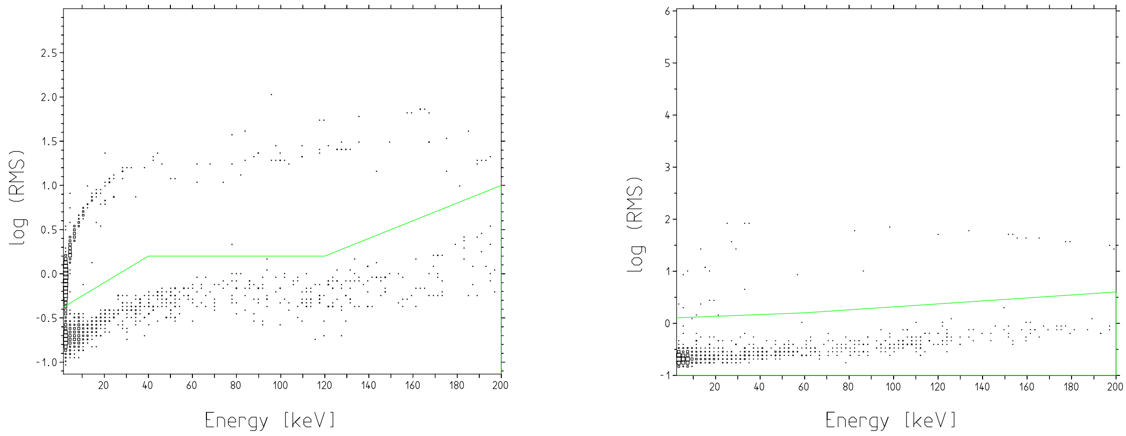

Figure 4.27: Run 15: Plot of the logarithm of the RMS deviation of data from fit for channel 1 (left side) and channel 2 (right side) obtained by fitting all recorded events with a linearised template. The template was obtained averaging for each detector 122 keV pulses from the calibration source and converting it to energy as described in the text.

In fig. 4.26 a spectrum of the lowest injected discrete test pulse energies is shown for channel 1 (left plot) and channel 2 (right plot). A trigger efficiency of 100% is reached at 2.3 keV for ch. 1 and at 3.5 keV for ch. 2. As can be observed from the response functions of these two channels shown in figure 4.21, the response function of channel two extends over a wider energy range and is much more linear than the one of ch. 1. This results in a smaller pulse shape change over the energy range and the logarithm of the RMS deviation of the pulse shape from the linearised template as shown in figure 4.27 on the right is almost constant. This is different for channel 1 as shown on the left plot of fig. 4.27. Above 120 keV the value of the deviation of the pulse shape from the template increases and the opposite happens in the low energy region. On the figure the line indicates the pulse shape cut that has been applied. Apart from the structure blown up in fig. 4.29 on the upper side, all the pulses above this line are due to interactions which lead to an energy deposition beyond the dynamic range and therefore result in events which saturate as shown in fig. 4.28.

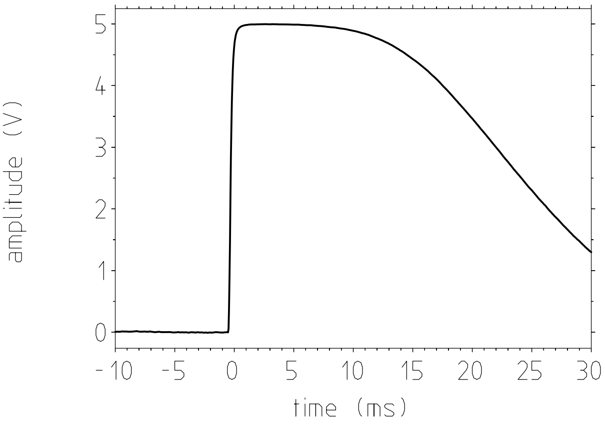

Figure 4.28: Saturated pulse shape.

The pulses leading to the structure blown up in fig. 4.29 came into existence after substituting the sapphire balls with plastic stubs. As shown in the lower plot of the same figure, all these pulses are characterised by a longer decay constant and a low energy deposition. Therefore the calculated deviation of their shape from the template results in this characteristic shape shown in the upper figure. At threshold the PSD method is not powerful enough to allow a clear discrimination and the two distributions of the RMS deviation tend to merge as shown in fig. 4.27. The hypothesis is that signals in this band are due the to heat releases from structural relaxations in the plastic support and as shown on the right side of fig. 4.29 they are regularly distributed over time.

As a next step the events in coincidence in the two detectors were removed. As described in 4.1.4 events within a ±4 ms interval in the onset channel difference distribution plot were removed. These events have been separately analysed and

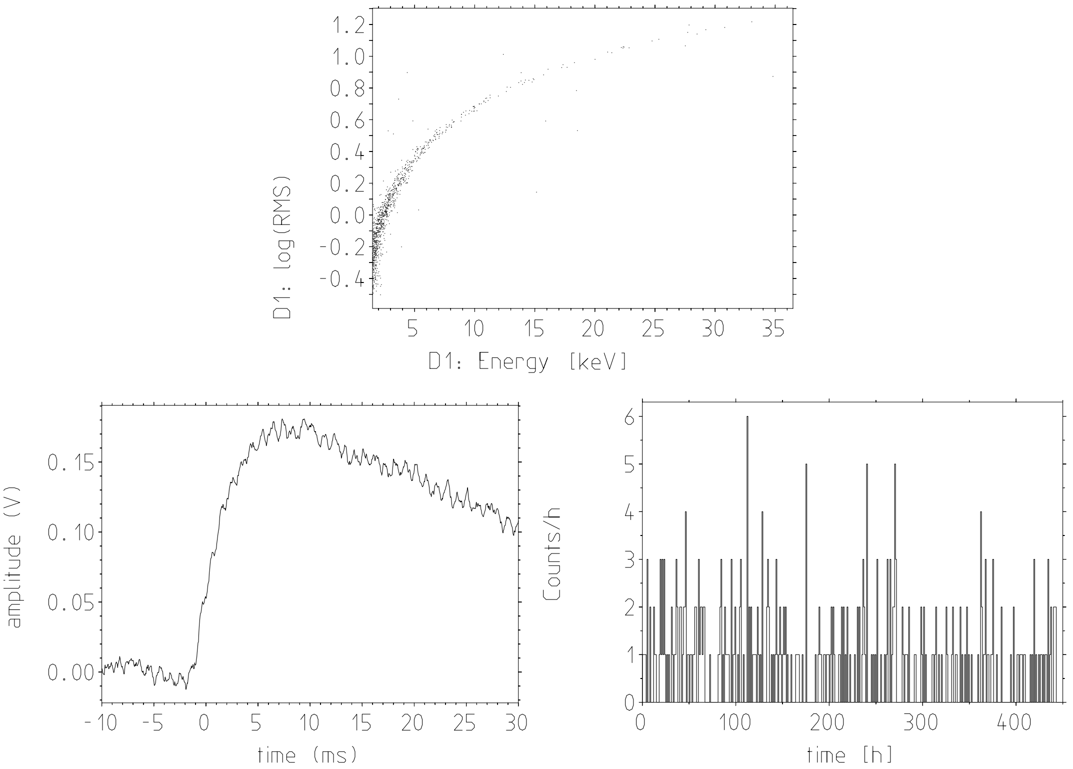

Figure 4.29: Channel 1: pulses with a longer decay constant probably due to heat releases from the plastic supports. On the upper plot their distribution in the plot of the log(RMS) deviation versus energy is blown up. On the lower left plot the typical shape of these pulses is shown while on the right side their rate as a function of time is plotted.

a plot is shown in 4.30. On these events the same threshold of 1.5 and 2.5 keV has been set for ch. 1 and 2 respectively. Also the pulse shape cut has been applied. Although in fact most of the saturated pulses are true coincident events, their pulse height does not provide sufficient information to reconstruct the deposited energy. Therefore they are misplaced in the energy spectrum as can be seen in fig. 4.27. In figure 4.30 an overview of the distribution of the coincident events over the energies of the two detectors is given and a blown up view of the points and of the low energy region is shown in the two lower plots. About 20% of the good events are coincident. Besides having low statistics, many events undergo multiple scattering, and the total energy deposition due to the sum of the coincident events does not result in any structure as in the case of the calibration measurement (4.23).

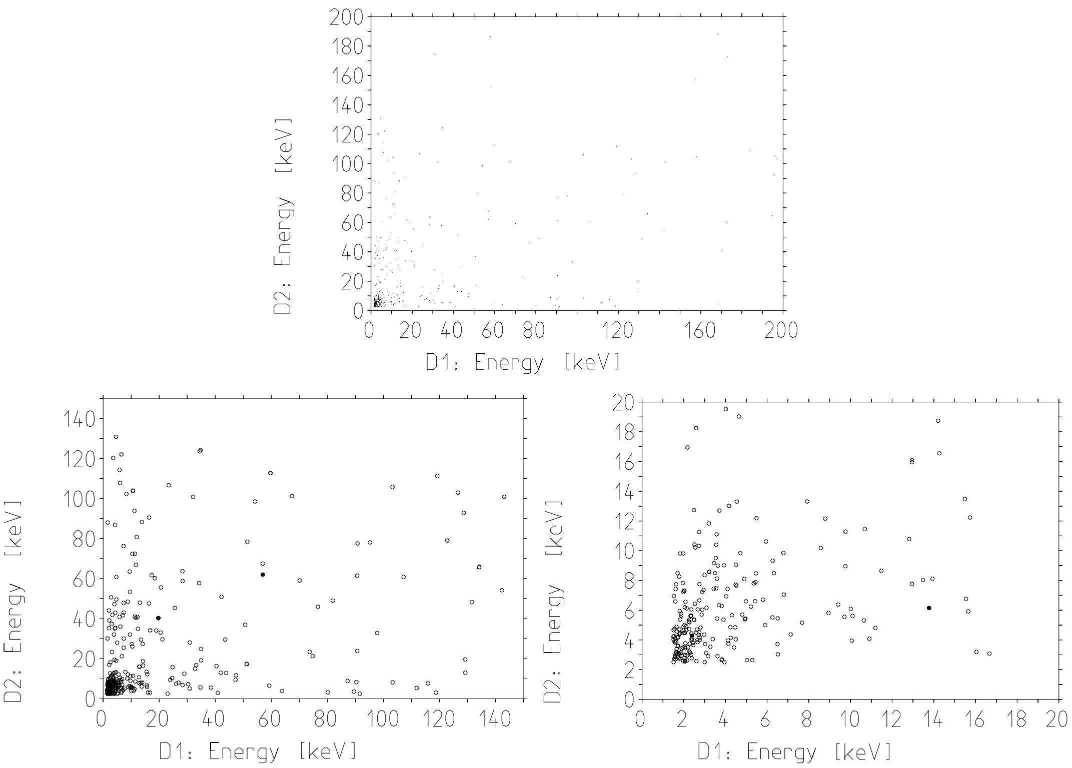

Figure 4.30: Plot of the events coincident in the two crystals over the energies of channel one (x axis) and of channel two (y axis). In the lower plots the points have been blown up for a clearer identification of any structure. However no information can be deduced about the total energy deposited in the two detectors resulting from the sum of the coincident events, not even in the lower energy region (right lower plot).

Energy spectrum

The final energy spectrum of channel 1 obtained summing up a total of 14.92 kg days live time is given in fig. 4.31 in counts/kg/keV/days and plotted with 1 keV energy binning. In the energy region between 15 to 25 keV the count rate in counts/keV/kg/days is ~ 1.4 and drops down to less than 0.4 above 50 keV. The peak in the low energy region is present in both detectors with about the same count-rate of 6 ±1 counts per crystal per day. The fitted position of this peak gives 7.9 ±0.1 keV for channel one and 7.1 ±0.1 keV for channel 2. This could be due to Copper (from the holder) or Nickel (from the wires) X-ray lines (8 and 7.4 k-shell emission lines respectively). However, a thorough check of the energy calibration at the lower energies identified a systematic error in the energy extrapolation due to pulser non-linearities (see 4.1.1). An effect of this can be shown blowing up the low energy region of the response function as in fig.4.33. In this run a correction for this error could not be implemented since the square root output of the heater module was not recorded in parallel

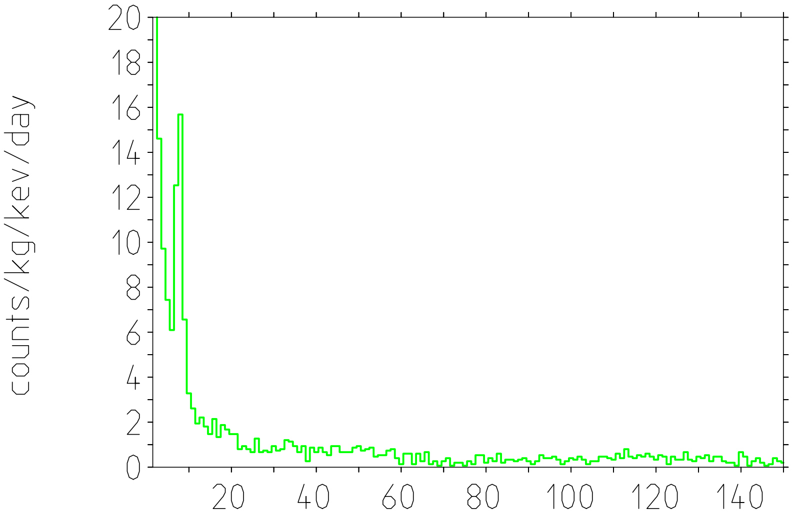

Figure 4.31: Run 15, channel 1 final energy spectrum. The data consist of 14.92 kg days live time plotted from threshold (2.5 keV) to 150 keV with 1 keV binning. Both the RMS and the coincidence cuts have been applied as described in the previous subsection.

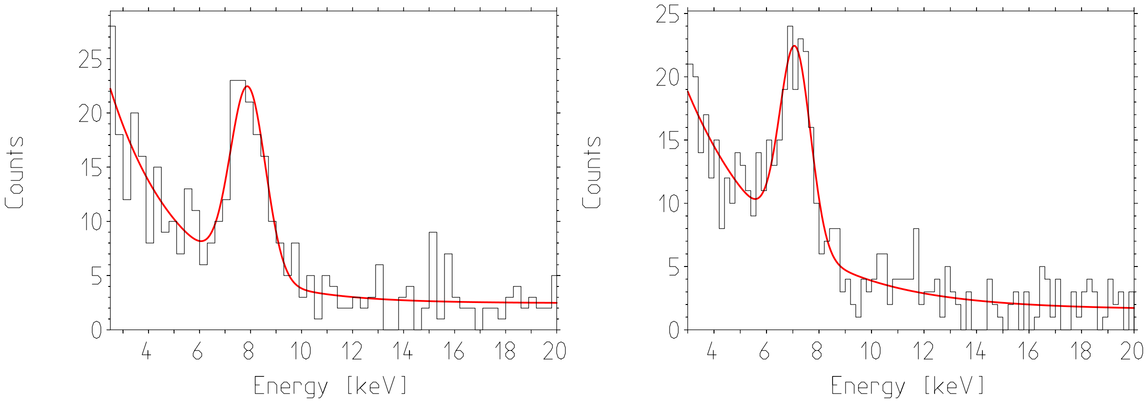

Figure 4.32: Run 15: fit of the peak on channel 1 and 2 energy spectrum on 18.4 days live time. The peak position is at 7.9 ±0.1 keV on channel 1 and at 7.1 ±0.1 keV on channel 2.

(see section 4.1.1). In this case the fit of the response was simply forced to zero. As will be shown in the subsequent measurements (section 4.2.4) the effect of this correction results in a shift of the peak position towards lower energies. Furthermore the energy resolution of the peak on both detectors is twice the one of the test pulses at the same energy (see fig.4.26), suggesting the presence of a more complicated structure. Therefore this first hypothesis about a Cu-Ni contamination was discarded.

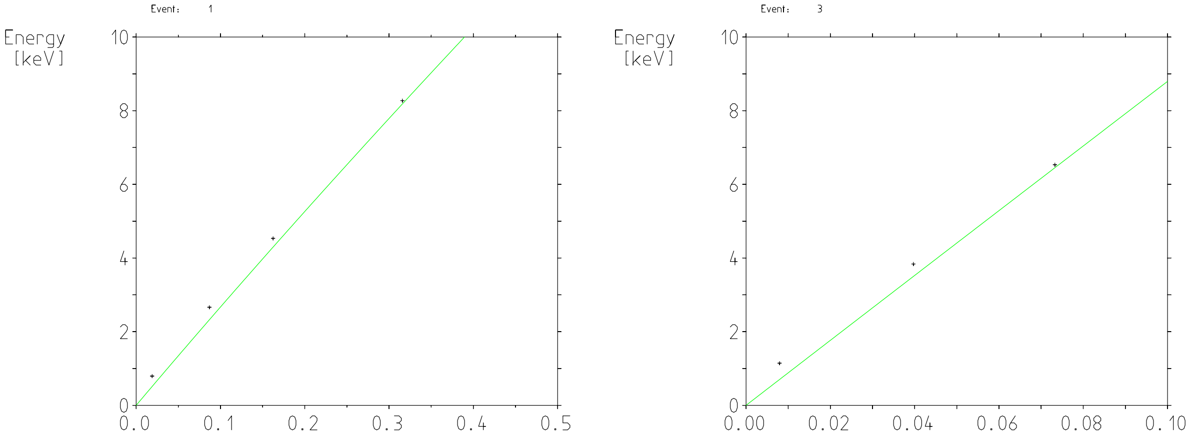

Figure 4.33: Zoom of the response functions of channel 1 and 2 (fig. 4.21 right plots) in the low energy region: the effect of the systematic error due to pulser non linearities is here visible.

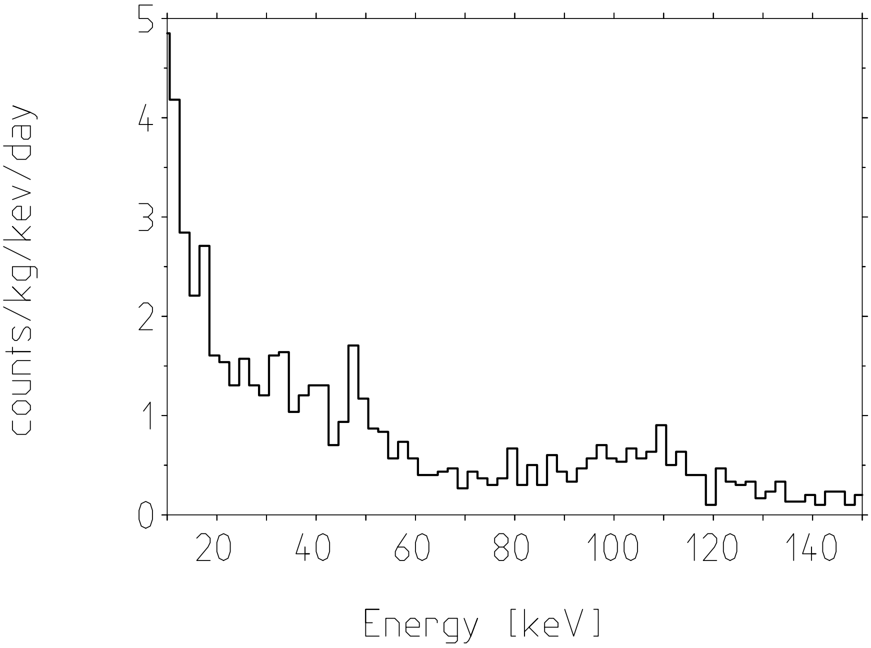

Figure 4.34: Ch2 energy spectrum selected between 10 and 150 keV and plotted with 2 keV binning.

The energy spectrum of channel 2 shows a slightly higher count-rate: about 1.8 counts/keV/kg/days in the energy region between 15 to 25 keV and 0.5 above 50 keV. The shape of the spectrum (fig. 4.34) suggests the contamination of the crystal with ^{210}Pb. The ^{210}Pb β- decay to ^{210}Bi is characterised by a 16.4 keV Q-value with 84% branching ratio and 63.5 keV Q-value with 16% branching ratio. This decay is characterised therefore by a 46.54 keV gamma emission line.

^{210}Bi beta decays (1162.1 keV Q value with 100% b.r.) to ^{210}Po which eventually decays emitting a 5.3 MeV alpha particle with 100% branching ratio. The ^{210}Po α-decay results in the ^{206}Pb daughter nucleus recoiling with an energy of 103 keV. All these features seem to be present in this spectrum and a fit of the 46 keV gamma emission line and of the 103 recoil peak is shown in fig. 4.35. The results of the fits are given in table 4.2.2.

This would translate in a measure of a Quenching Factor (see chap.1) equal to 1 in the specific case of sapphire crystals. However due the low statistic of this measurement, no strong conclusion can be drawn here.

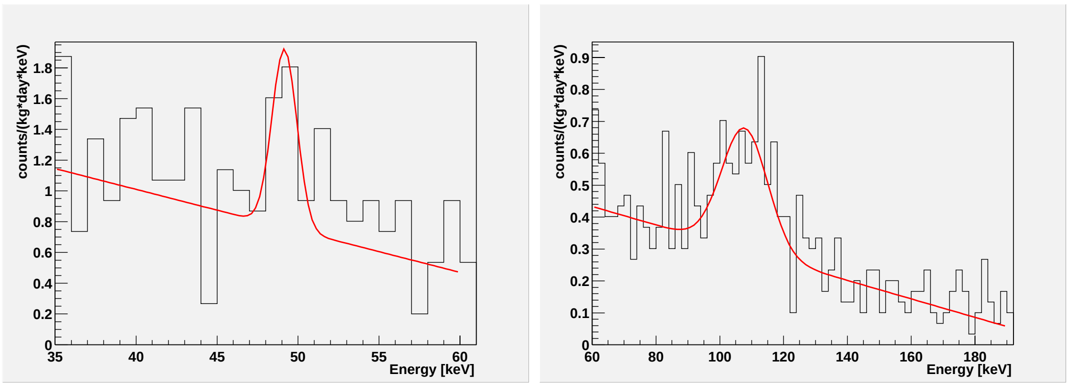

Figure 4.35: Run 15: fit of the 46.54 keV γ peak and of the 103 keV recoil feature plotted with 1 keV binning. The results of the fit are reported in table 4.2.2 for different binnings.

Table 4.2: Results of the fit of fig. 4.35

Binning	Fit position [keV]	Error	FWHM [keV]
0.2 keV	47.7	± 0.5	1.6
0.5 keV	48.3	± 0.7	1.9
1 keV	49.2	± 0.9	1.9
0.2 keV	105.5	± 7.5	24.7
0.5 keV	106.9	±4.9	21.8
1 keV	108.0	±14.8	22.1

For comparison a simulation of such a contamination with the EGS4 code [Mar00] at different implantation depths in a sapphire crystal gives the spectra shown in fig. 4.36. Dx50 corresponds to implantation depths of up to about 5 μm. The most prominent features in the spectra are the full energy peak of the 46.5 keV internal conversion level in ^{210}Bi, the 30.1 keV L1 conversion electron (emitted in 69% of internal conversion) and the 16.4 keV L1 ^{210}Bi level.

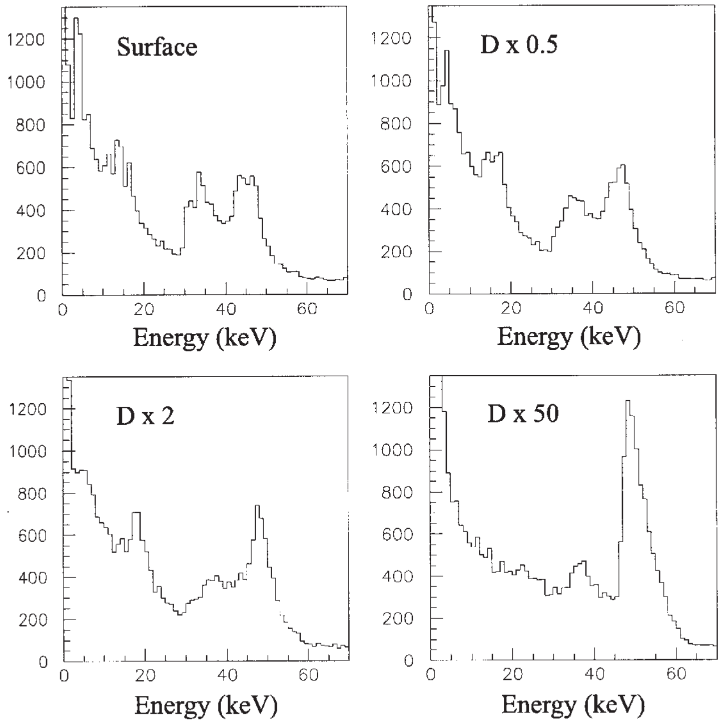

Figure 4.36: Figure taken from [Mar00]. It shows the dependence of the shape of the simulated ^{210}Pb and ^{210}Bi energy spectrum on the implantation depth of ^{210}Pb in the sapphire crystal. Increasing values of D× n correspond to deeper implantation. For the details on the resulting spectrum features see the text and the given reference.

Only in 5% of all decays, a 46.5 keV γ is emitted directly. The strong peak at 46.5 keV for the largest implantation depth means that almost all de-excitation electrons and X-rays also fully deposit their energy in the crystal. The smaller the implantation depth, the more spectral features become apparent, e.g the peak at 16.4 keV where the 30.1 keV conversion electron escapes the crystal. An additional spectral feature included in these figures is the 17 keV $\beta-$ decay of ^{210}Pb which precedes the internal conversion process. Its continuous energy distribution adds on the internal conversion spectral features, e.g. produces the asymmetric 46.5 keV peak in the last figure (lower right panel).

4.2.3 Run 16: The Dark Matter run

In this run four sapphire crystals were mounted in the cold box as follows:

- Readout Ch. 1: Crystal nr. 5 in holder nr. 5 as in Run15.
- Readout Ch. 2: double detector in holder nr. 6 as in run 15. Only one thermometer connected

- Readout Ch. 3: The SQUID chip of this channel is broken. A “dummy” detector is however implemented in order not to leave any crystal face directly exposed towards the cold box. For this purpose sapphire detector nr. 7 in holder nr. 3 has been used.
- Readout Ch.4: crystal nr. 8 in a mixture of holder nr. 7 (new one from TU-München machined out of radiopure copper) and holder nr. 2 from which the screws and the cover have been taken. For a description of this crystal see table 4.2.3. The detector has been rotated by 90 degrees with respect to its previous placing in the copper holder in order to avoid to have cracks as contact points. Out of six faces there is only one point that still has the contact on the crack, at the centre of the face. Delrin tips have been used for mounting.

	Crystal VIII
Distributor	BEC Breznikar Consulting GMBH Franz Haniel Str. 82 47443 Moers
Manufacturer	SCT Single Crystal Technology BV Ir. Schiffstraat 220 NL-7547 RD Endeschede
Material	Al_2O_3
Mass	262 g
Dimensions	$40\times40\times41$ mm^3
Surface	2 r-plane optically polished 4 sides optically polished
W film evaporation	550° crystal temperature substrate heating power: 375A/2.43V÷363A/2.39V $8 \div 2 \times 10^{-8}$ mbar rate of deposition: 2 Å/s film thickness: 1900 Å
W thermometer size	3×5mm^2

Table 4.3: Run 16: Crystal description[Mei99].

Due to the experience gained with the previous run the shaping of the trigger signal was optimised and a lower trigger threshold was obtained. Channel 1 and 4 showed the best performance and after a few days of data taking it was therefore decided to use readout channels 2 and 3 to monitor the square-rooter output of the heater module to record the injected test pulses in the detectors connected to channels 1 and 4 respectively as described in 4.1.1. These two detectors were facing each other. Data from detector nr. VIII (channel 4) which showed the lowest threshold were used to set dark matter limits, while the detector connected to channel 1 was used to remove coincident events. The bonding scheme for detector nr.VIII is shown in fig. 4.37.

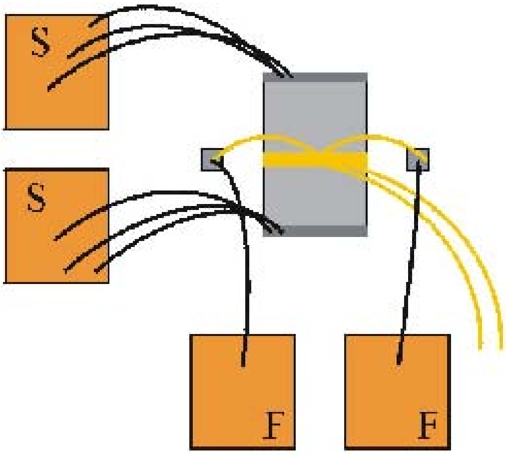

Figure 4.37: Detector nr. VIII bonding scheme.

The calibration was performed during a ten hour run with an external ^{57}Co source as in Run 15 and subsequently checked with another calibration run at the end of the data taking period. The measurement time of the background run was 138.8 hours of which 0.6 h were dead time, which corresponds to a total of 1.51 kg days of data. The result of the energy correction for the pulser non-linearities (fig. 4.38) applied to the channel 4 response function is shown in fig. 4.39. The zoom in the low energy region shows that the systematic error on the extrapolation present in Run 15 has now been corrected for.

The detector response monitored with test pulses was stable within resolution during the whole recording period. In fig. 4.40 the lowest test pulse amplitudes used to calculate the above response function are shown as function of the whole running time.

As can be observed in figures 4.40 and 4.41 the trigger efficiency for channel 4 of 100% was measured at 580 eV throughout the whole run used to set Dark Matter limits. A software threshold of 600 eV was applied.

As described in section 4.1.4 events in coincidence in two or more detectors cannot be due to WIMPs and therefore can be safely discarded. As shown in fig. 4.15 the cut was set at about ± 4 ms (±20 channels in the figure plotted over the onset channel difference) thus removing the coincidence peak in the distribution

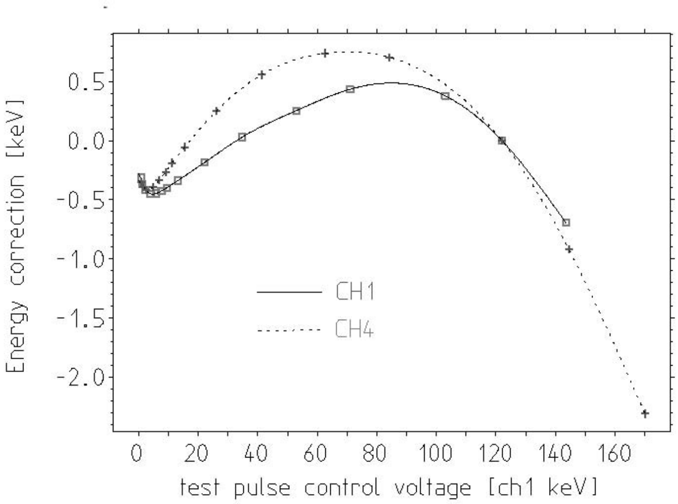

Figure 4.38: Energy correction for channels one and four.

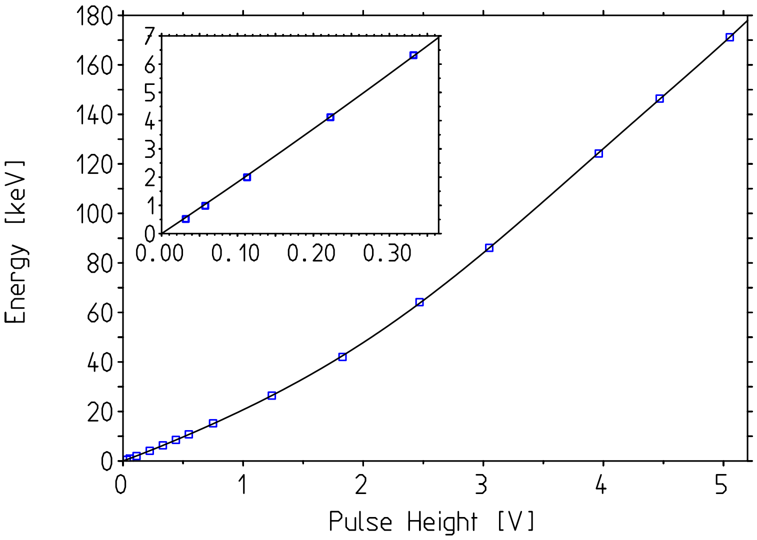

Figure 4.39: Detector nr. VIII response function after applying the energy correction as described in 4.1.1.

of the time differences. The upper histogram shown in fig.4.42 represents the raw spectrum, while the middle histogram shows the data after removing coincident events. 76 counts were removed with this cut out of 446 events from threshold to 120 keV, which translates into about 17% of all recorded data are coincident.

The PSD method described in 4.1.3 and 4.2.2 was then applied fitting all the events with the linearised template obtained by averaging and converting to energy pulses from the 122 keV calibration peak. Both saturated and noise

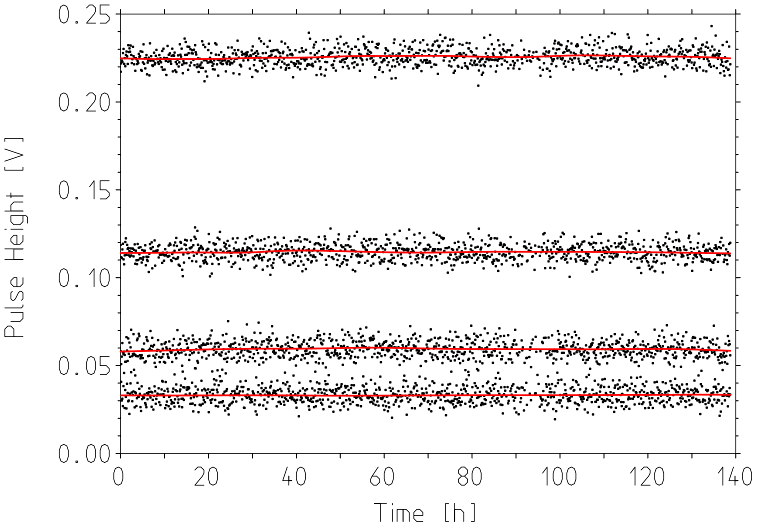

Figure 4.40: Pulse heights of heater pulses corresponding to 580, 1.04, 2.04 and 4.08 keV (see also fig.4.41). The detector is stable within the resolution before applying any linearisation.

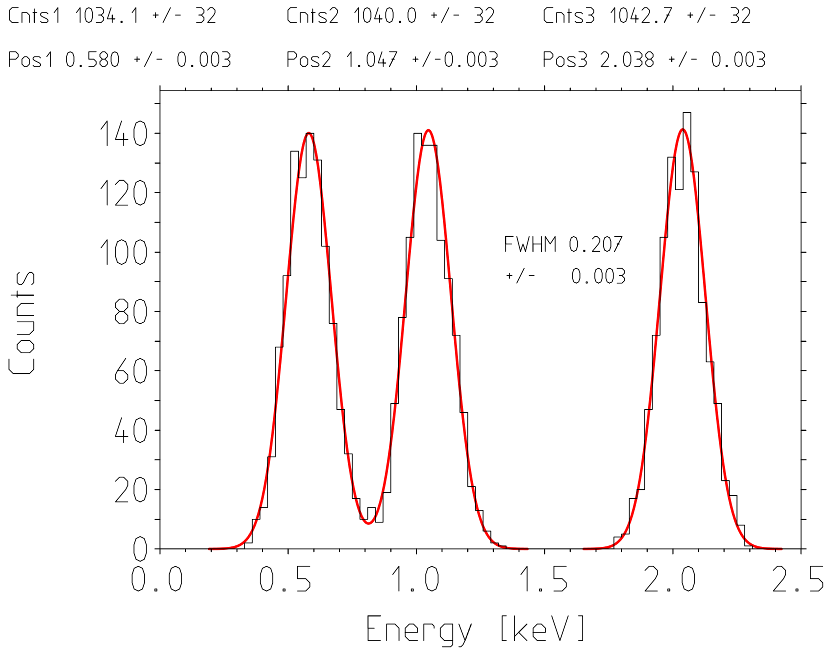

Figure 4.41: Gaussian fit of test pulses injected on detector n VIII plotted over energy. The result shows a 100% trigger efficiency for the test pulse located at 580 eV.

pulses were discarded and the cut was chosen such that the retention efficiency was 100% at all energies down to threshold. As described in section 4.1.3 and fig. 4.13, this efficiency was checked with two methods: the same cut was applied to test pulses resulting in only one out of 1032 being discarded at 580 eV; the same procedure was also applied to the calibration measurement where only 0.22% of all events were discarded. The lower histogram of fig. 4.42 shows the final result after applying both cuts. Also reverting the sequence of the cuts, the coincidence

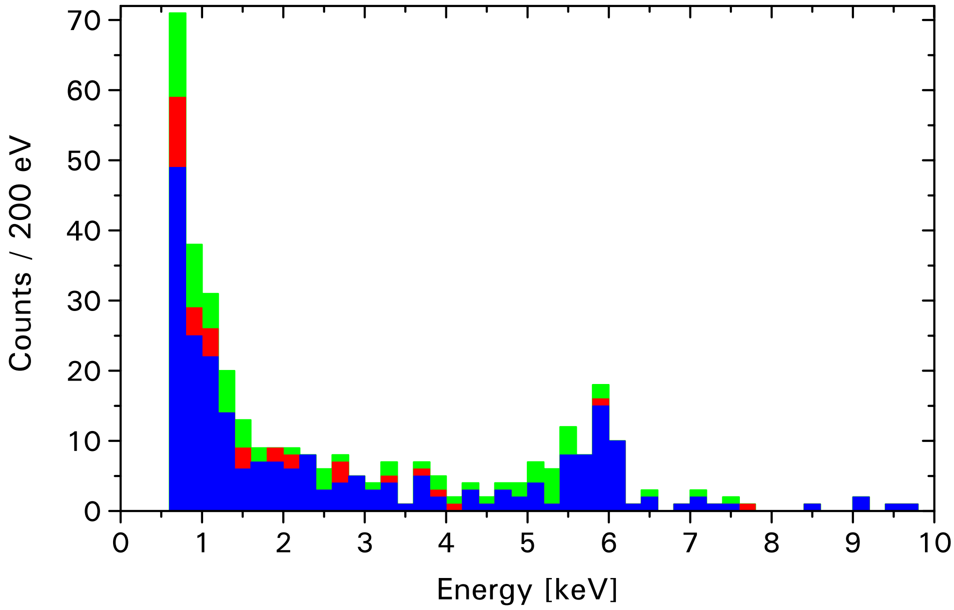

Figure 4.42: Run 16: detector nr. VIII (readout channel 4) energy spectrum. The upper histogram shows the raw data, the middle histograms results after removing events in coincidence with channel 1 (see text) and the lower histogram is the final energy spectrum obtained after applying the pulse shape cut.

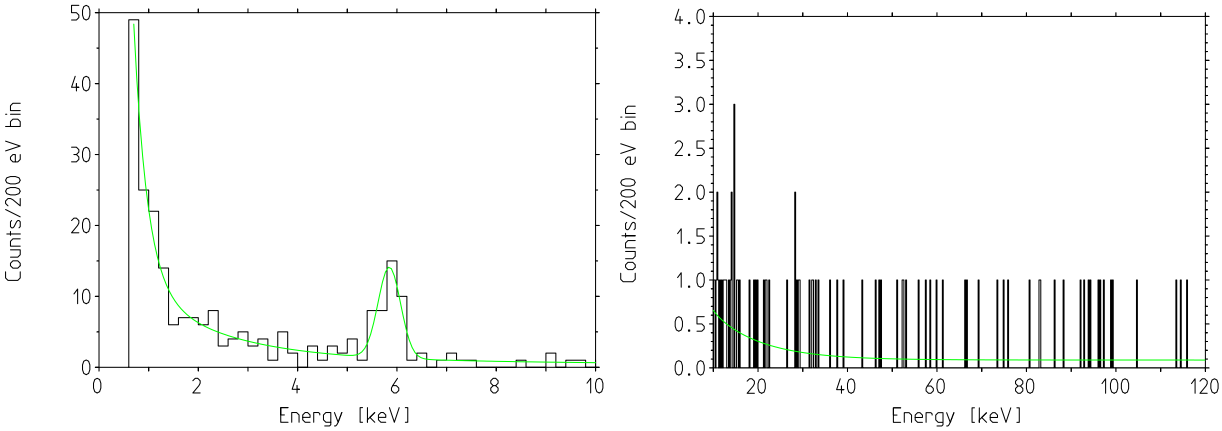

Figure 4.43: On the left side the final energy spectrum in 200 eV bins of the Dark Matter run is shown. The solid curve is an empirical fit to the experimental spectrum used to set Dark Matter limits (see 4.3). On the right side the behaviour of the count-rate in the region between 20 and 120 keV is shown.

cut again removes about 17% of the events with proper pulse shape. Having only one out of six faces facing the other crystal this result is consistent with all events being background.

The final spectrum is again shown in fig. 4.43. In the energy range between 15 and 25 keV there are 0.73 ±0.22 counts/kg/keV/day while around 100 keV the measured rate is less than 0.3 counts/kg /keV/day. The fit of the peak already present in Run 15, now corrected for the systematic introduced by the pulser is placed at 5.9 keV. The measured rate is 7±1.2 counts per crystal per day as in the previous run. Its position suggests the presence of a ^{55}Fe contamination which emits Mn X-rays at 5.9 keV and no gamma. However as already in section 4.2.2 its resolution of 520±90 eV is about twice the FWHM of test pulses at the same energy (fig.4.41) and, as will be shown in the next subsection, of a 6.4 keV line from an internal calibration source.

4.2.4 Run 17: The Calibration run

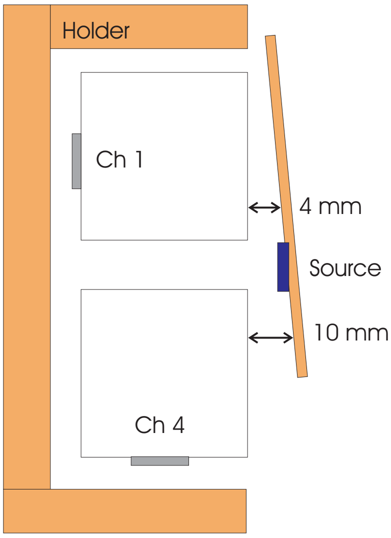

Figure 4.44: Run 17: calibration run with a weak ^{57}Co source placed inside the cold box directly facing the crystals. As shown here the two detectors used for the Dark Matter run remained unchanged in this set-up while the other two crystals where removed. At their place a low activity ^{57}Co melted in a Pd foil and glued on a copper holder was placed at a distance of about 4÷10 mm as shown in this figure.

This run was dedicated to check the reliability of the calibration method at low energies. A major effort was devoted to select a proper source characterised by a weak activity (of the order of few counts per day) and γ emission lines in the low energy range. Such a source could not be implemented in the standard position since the copper in-between would have shielded the lower energy γ

decays. Therefore a low activity ^{57}Co was eventually selected and mounted inside the cryostat directly facing the crystals as shown in fig. 4.44.

The set-up concerning readout channel 1 and 4 remained unchanged from the Dark Matter run. The other two crystals were removed to place the source and on readout channels 2 and 3 the square rooter output of the heater module was monitored. The data consist of a ten hour run with an external ^{57}Co source in standard position to calibrate conforming to the method used in the Dark matter run, and of about 50 hours recording time after removing the external source. After about 38 hours in which the pulse height response to test pulses of the same injected voltage amplitude on channel 4 was exactly the same as during calibration, the detector experienced a drift of the operating point. This is shown in fig 4.45 where the left plot shows the measured pulse height of test pulses during the recording time with the external calibration source and the right plot show the measured pulse height over time after the external source has been removed. The injected voltage amplitude is the same for the whole period, but in the last 22 hours the pulse height changes.

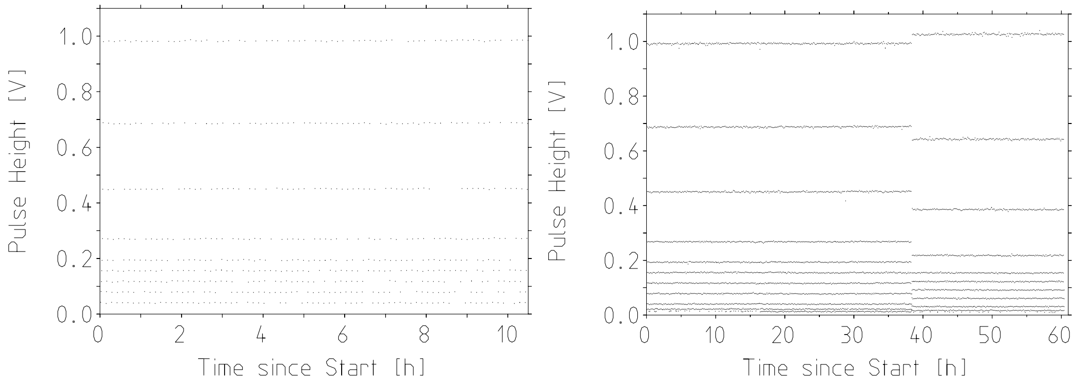

Figure 4.45: Measured pulse height as a function of time during the ten hour calibration run (upper figure), during the first 38 h measuring time (lower left plot) and in the last 22 h measuring time after a gain jump occurred (right lower figure). As can be seen here the measured pulse height for the same injected voltage amplitudes is the same in the first two figures while it changes in the last one.

The analysis was done separately for the two mentioned periods. Since in Run 16 the analysed measuring time was at the same operating point as during its calibration, the first period was used to study the systematic of the calibration method as applied in the Dark Matter run. The second period was then studied to investigate the influence of such jumps in the gain on the calibration.

As previously described each test pulse was fitted with a separate template for each amplitude, while background pulses were fitted with a linearised template averaged from events contributing to the 122 keV peak from the external source. The correction implemented for the pulser non linearity monitored during the whole acquiring period is shown in fig. 4.46.

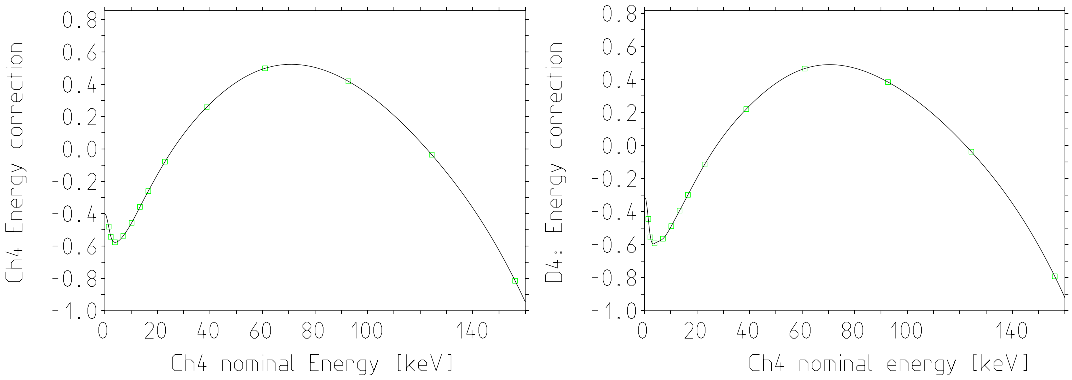

Figure 4.46: Energy correction in keV for channel 4 in the first 38 h (on the left) and after the gain jump (on the right).

After performing the whole calibration procedure the distribution of test pulses in terms of equivalent gamma energy is plotted over time in fig. 4.47. In plot 4.48 the response function for the first 38h is shown.

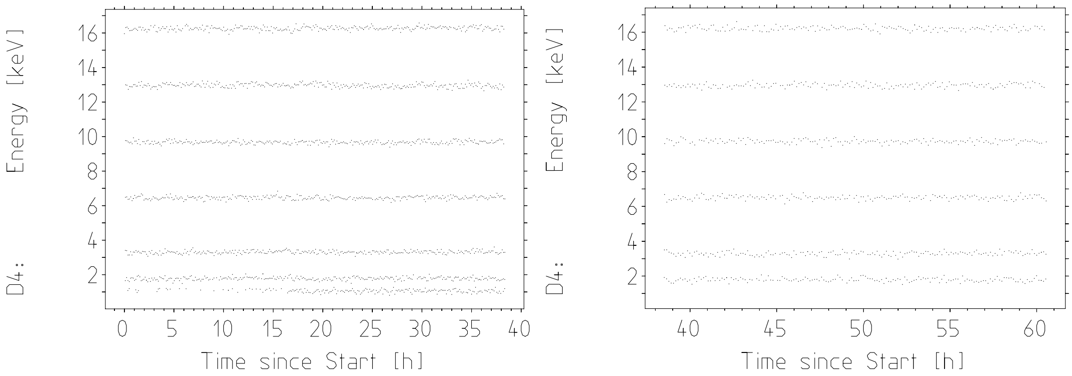

Figure 4.47: Test pulses in terms of equivalent gamma energy as function of time in the two recording periods (see text).

As introduced in section 4.1.1 fig. 4.2, besides the 122 and 136 keV γ lines, the ^{57}Co emits 14.4 keV γ and 6.4 keV Fe X-rays. These last two lines gave rise to the peaks shown in fig. 4.49 and the result of the fit for the first 38 hours is given in table 4.4.

As a result the calibration procedure puts the 14.4 and the 6.4 keV lines 5.3% and 5.4% too high (table 4.4). The energy resolution for the 6.4 KeV peak is $\Delta E = 200 \pm 50$ eV (FWHM) in agreement with the energy resolution of the heater pulses.

Dark Matter limits are mostly affected by the lower energies. However, since energies are shifted to higher values this error puts CRESST limits on the conservative side. As shown in table 4.5 this effect is more severe in case of an abrupt

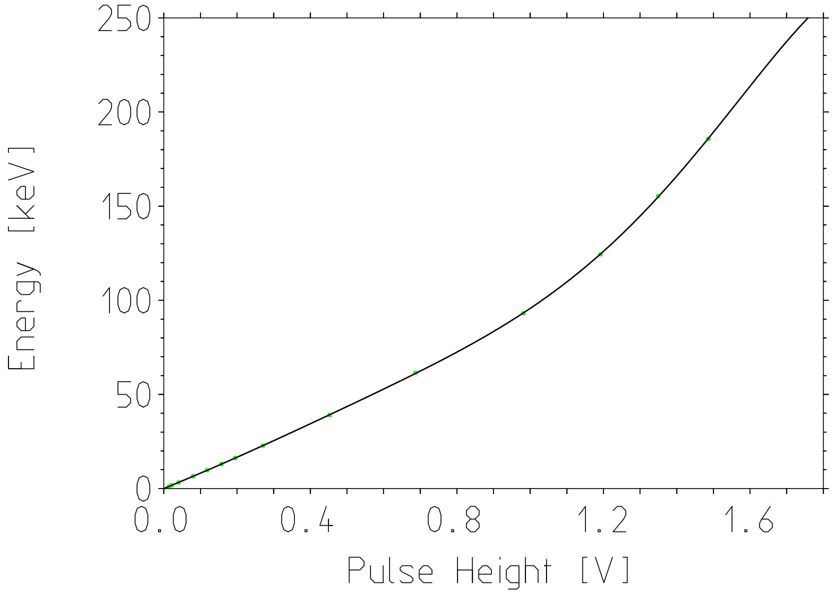

Figure 4.48: Ch 4 response function.

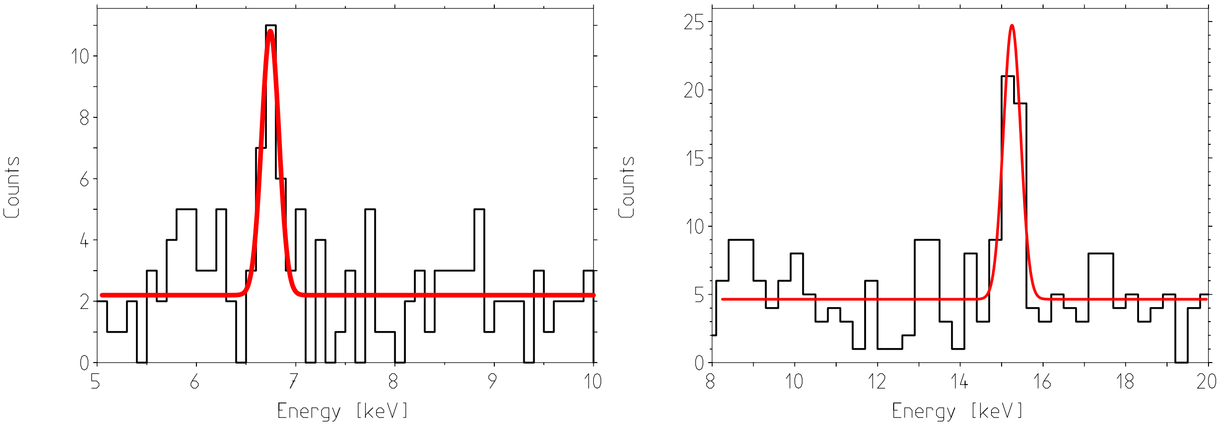

Figure 4.49: Fit of the measured energy of the 6.4 keV X-ray and 14.4 keV γ lines from the internal ^{57}Co source. The detector was calibrated with the same procedure as in the Dark Matter run.

Table 4.4: First 38.17 h period. This file has been calibrated fitting each test-pulse amplitude to its averaged standard event and it has been corrected for pulser non-linearities. The 122 keV peak results to be at 122.6±0.33keV

Fit results for 6.4 keV peak:	Fit results for 14.4 keV peak:
$6.74 - 0.05 + 0.07$ (90%C.L.)	$15.25 - 0.09 + 0.09$ (90%C.L.)

Table 4.5: Period from 38.17 h to 60.16 h. The 122 keV peak results to be at 121.47±0.37keV

Fit results for 6.4 keV peak:	Fit results for 14.4 keV peak:
7.04 −0.25 + 0.21 (90%C.L.)	15.76 −0.08 +0.08 (90%C.L.)

gain jump as it occurred in this case. The result for this measurement period is compatible within errors with the previous one.

4.3 CRESST Phase I Dark Matter limits

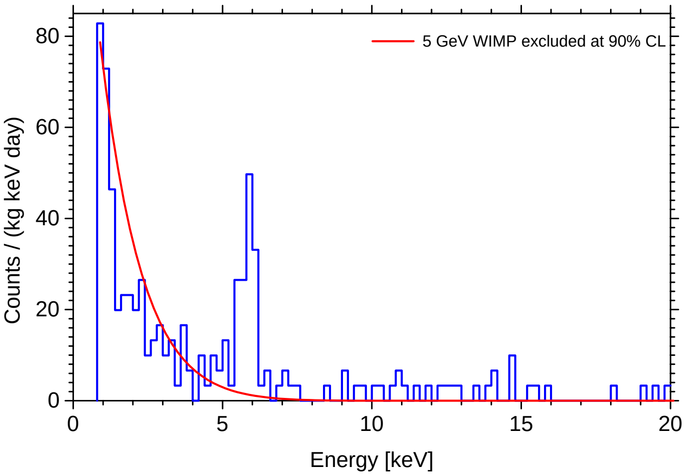

Figure 4.50: Comparison between CRESST Phase I measured spectrum and that expected for nuclear recoils caused by elastic WIMP scattering. The theoretical spectrum shown here is a 5 GeV WIMP spectrum excluded at 90% confidence level.

CRESST Phase I upper limits for the WIMP scattering cross section as a function of a WIMP mass have been obtained by comparing the measured 1.51 kg days spectrum of Run 16 (figure 4.43) with a theoretical event rate. The overview of the method applied to obtain CRESST Phase I results is given in Chap. 1.3.6. In figure 4.50 the measured energy spectrum is compared with a 5 GeV WIMP spectrum excluded at 90% confidence level.

The details for the calculation of the expected WIMP scattering recoil spectrum are given in [Ang02b] where an isothermal WIMP halo model (see section 1.3) has been assumed using a truncated Maxwell velocity distribution. As introduced in Chap. 1.3.6 this spectrum was convoluted with the experimental resolution. An energy dependent resolution formula which interpolates between the measured values at 6 keV and 122 keV $\Delta E = \sqrt{(0.519keV)^2 + (0.0408E)^2}$

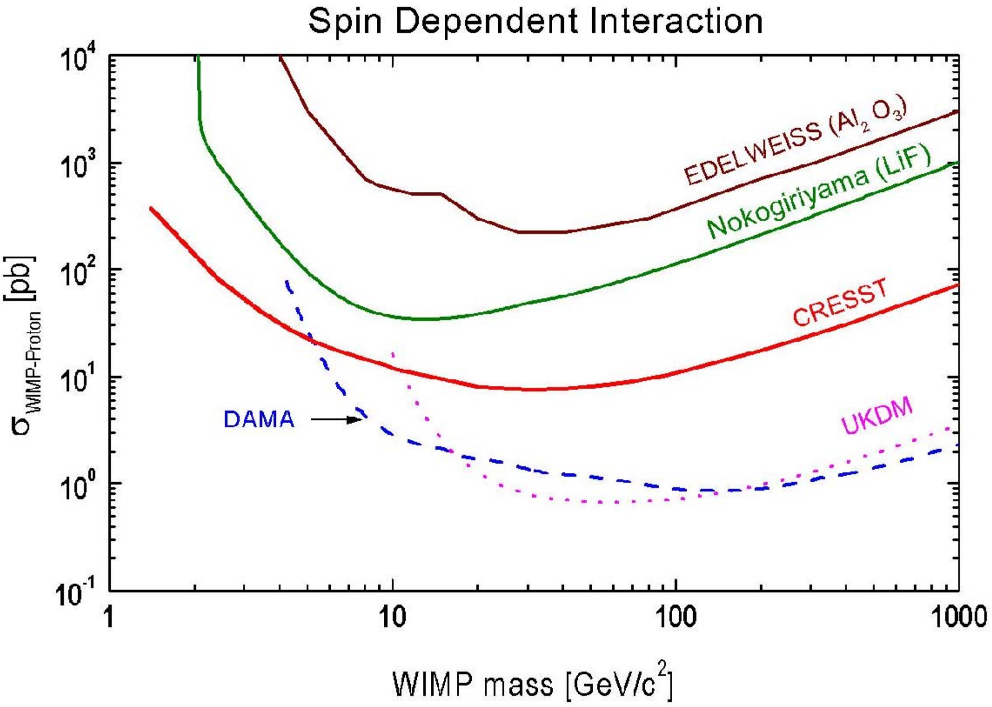

Figure 4.51: Equivalent WIMP-proton cross section limits for a spin-dependent interaction as a function of the WIMP mass. The parameters above the indicated lines are excluded at 90% C.L. CRESST limits are extracted from the 1.51 kg day measured spectrum discussed in section 4.2.3. For comparison also limits from EDELWEISS dark matter search using cryogenic sapphire detectors, from the LiF cryogenic experiment at the Nokogiriyama site, and from DAMA and UKDMC using NaI detectors (see Chap. 1.4) are shown [Ang02b].

has been used. The recoil spectrum was convoluted with a Gaussian with that FWHM and a quenching factor equal to 1 was assumed.

The Monte Carlo method described in Chap. 1.3.6 using the empirical fit of the data shown in fig. 4.43 has been applied giving the result shown in fig. 1.4. To compare the results to those of experiments using other target nuclei the resulting WIMP-nucleus cross sections have been converted in WIMP-proton cross sections.

In fig. 4.51 the obtained 90% C.L. upper limits on the σ_0 (see section 1.3) for spin-dependent WIMP interaction on Al are shown. In this plot equivalent WIMP-proton cross section limits at 90% C.L. as a function of the WIMP mass for the spin dependent case are compared with limits of EDELWEISS, DAMA and UKDMC (see section 1.4) results. As can be observed CRESST limits improve existing results for low-mass WIMPs. In fact the very low energy threshold of 600 eV achieved in the Dark Matter enabled us to explore WIMP cross section for mass range down to 1 GeV.

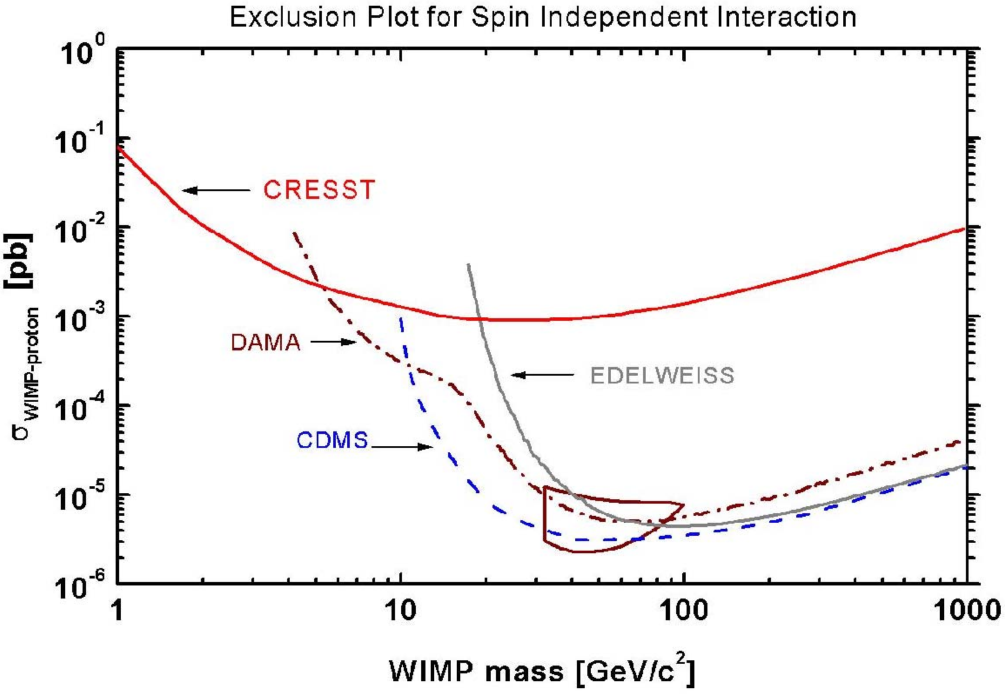

Figure 4.52: Equivalent WIMP-proton cross section limits at 90% C.L. for a spin-independent interaction as a function of the WIMP mass. For a comparison For a comparison limits from EDELWEISS using Ge detector with heat and ionisation active discrimination technique and from CDMS cryogenic detectors are shown. CDMS limits are obtained applying a statistical subtraction of the neutron background. DAMA exclusion limits with NaI are also shown and the closed contour indicates the DAMA positive evidence at 3σ C.L. from the annual modulation data.

While for the spin-dependent interaction the only contribution comes from ^{27}Al nuclei which have spin 5/2 and 100% isotopic abundance (see section 3.3), for the spin independent interaction both Al and O nuclei contribute. Due to the A^2 dependence of the cross section (section 1.3.2) the spin-independent channel is not favoured in case of a target with light nuclei as sapphire. However, as shown in fig. 4.52, CRESST Phase I is improving current best limits for WIMP masses below 5 GeV.

Chapter 5

CRESST phase II: first measurements

The main goal of CRESST Phase II is to actively discriminate electron recoils caused by ionising radiation, from nuclear recoils caused by neutrons and WIMP interactions and to provide improved sensitivity for high mass WIMPs. This can be achieved with the simultaneous measurement of the phonon and scintillation light signal using a scintillator with high mass target nuclei as absorber. As described in Chapter 3.3 a first 6 g proof-of principle detector using a $CaWO_4$ scintillating crystal and a small sapphire cryogenic detector to detect the emitted light, showed a rejection for electron recoils of better than 99.7% above 15 keV. A 300 g scintillating calorimeter has been developed for the second Phase of CRESST (see [Fra02]) and is currently operating in the Gran Sasso set-up.

In this Chapter an overview of the first measurements carried out at Gran Sasso is given. In particular a run where two sapphire detectors and a Phase II detector module were implemented is discussed. The sapphire detectors were used to check the radioactive background level after the move of the experiment to Hall A.

5.1 First Gran Sasso measurements and results

As mentioned in section 3.3 less than 2% of the energy deposited in the scintillating absorber is converted into light. Therefore the main challenge in scaling up to a 300 g detector module was the optimisation of the light collection and detection. For this purpose a very sensitive light detector had to be developed. Different types of detectors were investigated, finally achieving best results using a silicon substrate and a new thermometer design with phonon collectors. Furthermore a new holder with highly reflective inner surface shown in fig. 3.5 was developed to minimise light losses [Fra02].

For the phonon channel, the scintillating properties at low temperatures of crystals from different suppliers are under study [Don]. Another major concern is their radio purity. As mentioned in chapter 2 gamma spectroscopy is not always helpful for selecting the crystals since it does not provide any information about alpha decays and, due to the high Z of the crystal, gammas below ~100 keV, if present, are self absorbed in the crystal. Therefore only a direct test in the CRESST set-up allows a complete identification of the contaminations present in the crystal as will be discussed for Run 20.

5.1.1 Run 18

A first Phase II module was implemented in the Gran Sasso set-up before CRESST shut down for the move. Due to the short time scale a first yet unoptimised pair of detectors was used.

A $CaWO_4$ from a Hungarian supplier with a 8 × 9 mm tungsten thermometer directly evaporated onto its surface was used as absorber. The geometry and bonding scheme were the same as for the sapphire thermometers (see fig. 4.37). As mentioned in section 3.3, tungsten thermometers directly contacting the crystal showed a transition temperature of $\sim$ 40 mK. This implied a few drawbacks: the achieved threshold was rather high (about 10 keV) and the different operating temperature needed for the light detector ($\sim$ 12 mK) and the $CaWO_4$ detector rendered the stabilisation of the module more difficult. On the other hand the dynamic range was rather linear and wide, ranging from threshold up to about 3 MeV as shown in fig. 5.1.

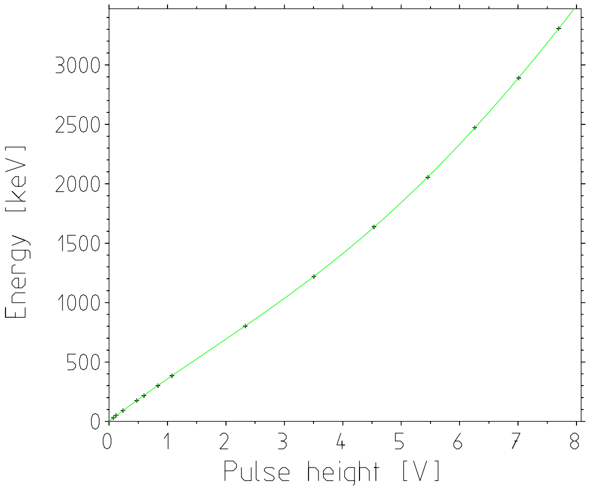

Figure 5.1: Run 18: $CaWO_4$ response function. The calibration has been performed using the 1.1 MeV gamma line from a ^{60}Co source together with the injection of test pulses. However, since the shape of test pulses is rather different from that of particle pulses (see text) the extrapolation of the calibration is unreliable.

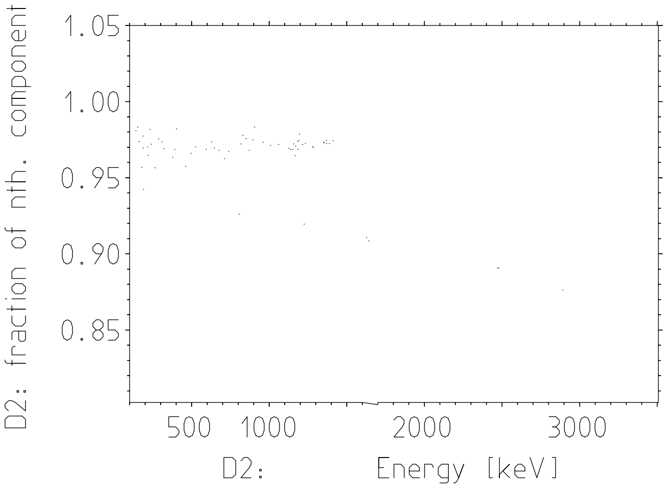

Figure 5.2: Dependence on the non-thermal component versus energy of the test pulses compared to particle events. For increasing energies the non thermal contribution to the heater pulses drops down while for particle pulses it remains constant.

The calibration of this detector was performed with the procedure described for the sapphire detectors. To calibrate the detector also at higher energies, the 1.1 MeV gamma line from a ^{60}Co source was used instead of the ^{57}Co emission lines. The injection of high energetic heater pulses to cover this wide energy range resulted in a pulse shape rather different from the particle pulses. It was observed that the higher the injected energy, the lower the fraction of the non-thermal to thermal component was. This is shown in figure 5.2. The heater injects the

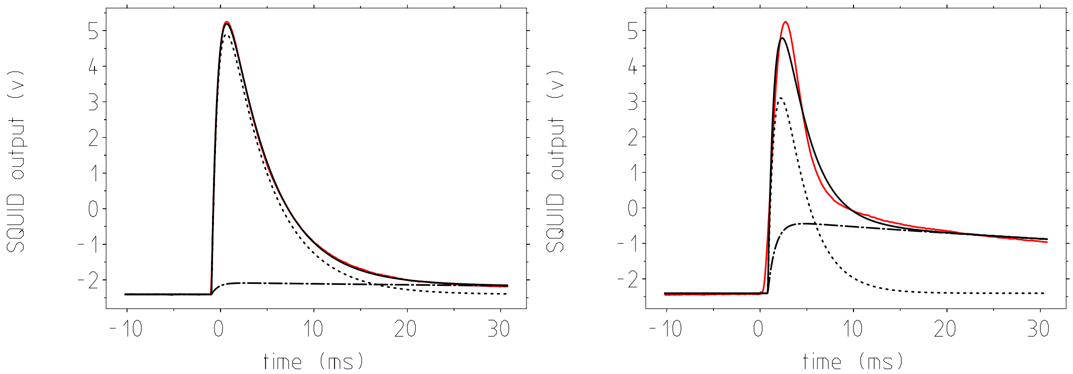

Figure 5.3: Run 18: the solid line represents the fit of a particle event of 1.1 MeV (left plot) and of a test pulse of the corresponding energy (right plot). The pulse shapes are substantially different, thus spoiling the extrapolation method of the energy calibration. The dashed dotted curve represent the thermal contribution to the signal and the dotted line the non thermal component which results to be much smaller for test pulses compared to particle events.

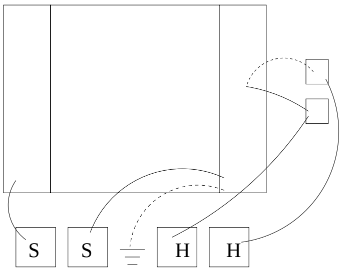

Figure 5.4: Run 18: bonding scheme of the light detector. The dotted lines indicate the gold bonding wires and the solid ones aluminium. The two squares on the bottom left are Copper Kapton isolated pads on the holder for the SQUID readout current and the two on the right serve for the heater. The two pads on both ends of the thermometer are of gold.

energy almost point-like in the centre of the film, whereas the energy input from non thermal phonons is uniform. The thermal coupling of the film is highly non linear since the power $P \propto (T^6_{electrons} - T^6_{phonons})$, where T is the temperature. The hot region of the W film near the injection point couples stronger to the substrate and thus the larger is the fraction of phonons transmitted into the absorber.

In fig 5.3 the fit of the non-thermal and thermal component is shown for a particle pulse (left plot) from the 1.1 MeV ^{60}Co gamma line and for a test pulse (right plot) of the same energy. The test pulse shape then changes with increasing energy and differs substantially from the shape of particle events, thus spoiling the extrapolation of the energy calibration.

For the light detector the detector used for the proof-of principle measurement was implemented. It consisted of a sapphire substrate of $10 \times 20 \times 0.5$ mm^3 coated on one 10×20 surface with silicon to improve the light absorption. Two small Al pads were added to the original design for the heater connections. The bonding scheme is shown in fig. 5.4. The pads on both ends of the thermometer are of gold and the two small pads for the heater are of aluminium. The dotted

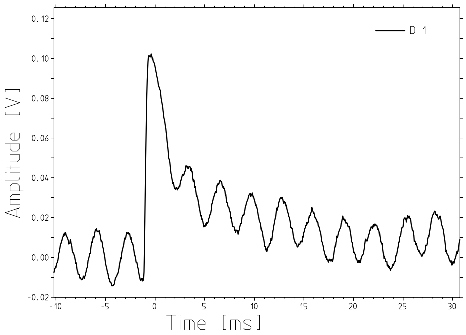

Figure 5.5: Light detector pulse corresponding to a 1.1 MeV signal on the scintillator.

lines indicate Au bonding wires while the solid ones represent Al wires. The dimensions of this thermometer were 1 × 1.5 mm. The sapphire substrate was resting on three sapphire balls and was held by two teflon springs from the top. At the contact point between the teflon and the substrate a sapphire ball was placed.

The base line of this detector showed large oscillations (see fig. 5.5) probably due to vibrations of the too long bonding wires needed to connect the thermometer to the pads on the holder. This prevented any calibration of the detector and provided no useful information in the energy region relevant to Dark Matter. Nevertheless the information about the pulse height already showed the discrimination potential of such a module. In fig. 5.6 an alpha contamination present in the crystal is clearly separated from the gamma band from the calibration source.

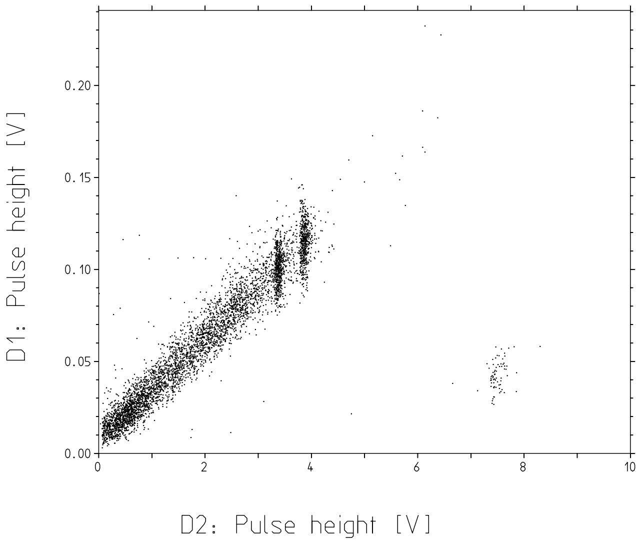

Figure 5.6: Run 18: scatter plot of a 2.5 h calibration measurement. On the x-axis is the pulse height of the phonon channel and on the y-axis is the pulse height on the light detector. The alpha population is clearly separated from the upper band from gamma and beta interactions. The two denser spots on the upper band are due to the 1.1 and 1.3 MeV gamma lines of the ^{60}Co source.

Another problem which showed up in this first run was the too high amount of teflon used for the holder. It needed a very long time to properly cool-down and even after running the detectors for several days, the measurement was disturbed from heat releases coming from the holder. For the subsequent runs the holder was completely redesigned using copper as housing as shown in fig. 3.5 and teflon only as tips (and no more sapphire balls) to tightly keep the crystal inside the holder [Fra02].

5.1.2 Run 19

In this run a different $CaWO_4$ crystal from the same Hungarian provider was tested. An Ir/Au thermometer was used for the phonon channel (see [Sta]). For the light channel a $30\times30 \times 0.5$ mm^3 silicon light detector with a 1×1.5 mm^2 tungsten standard thermometer was used. The Ir/Au thermometer showed a transition at around 20 mK. Unfortunately the thermometer was not perfectly sticking to the crystal and probably this was the main reason for the small signal to noise ratio. Therefore this detector was useless below about 500 keV. On the other hand again it showed a very linear and even wider dynamic range compared to the previous run. This is shown in fig. 5.7. A ^{60}Co source was used to calibrate the detector together with the injection of heater pulses covering the range from 500 keV up to about 6 MeV. Again the pulse shape of test pulses was rather different from particle pulses as discussed for the previous run. Due to the high noise on the baseline a proper template from particle pulses could not be constructed. Therefore pulses were averaged with the moving channel algorithm to estimate their pulse height. The resulting calibration spectrum is shown on the left plot of fig. 5.8. On the right plot the corresponding spectrum of the light detector is shown. This detector has been analysed using the template fit method. The resolution on the 1.1 and 1.3 MeV electron equivalent peaks is ~130 keV and the resolution on the baseline is ~6.5 keV.

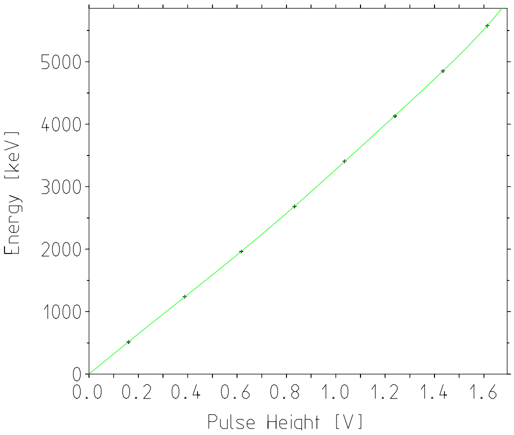

Figure 5.7: Run 19: response function of the $CaWO_4$ detector with an Ir/Au thermometer. The dynamic range is very wide. However the thermometer was not optimally sticking to the crystal giving rise to a rather low signal to noise ratio and to a different pulse shape of test pulses from particle events. Therefore also in this run the energy extrapolation is not reliable although test pulses were covering the whole range up to 6 MeV as can be seen on this plot.

A small cross talk between the heater current injected for the test pulses and the bias current was present as shown in fig. 5.9. Since the bond stitch is not really point like, the smaller the thermometer sizes are, the higher is the

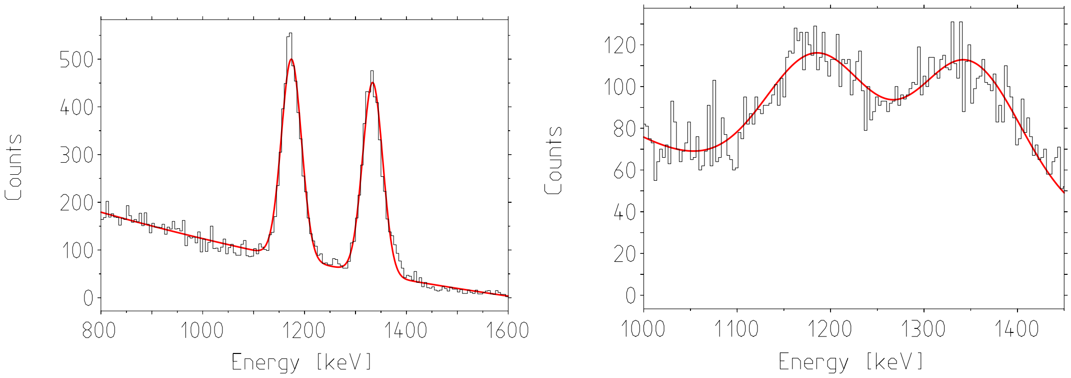

Figure 5.8: Fit of the calibration peaks from the ^{60}Co source on the phonon channel (left plot) and of the corresponding peaks on the light detector (right plot). The ^{60}Co peaks result at 1174.2 ± 0.42 keV and 1333.8 ± 0.39 keV with a FWHM of 46.5 keV on the phonon channel and at 1184 ± 3 keV and 1338 ± 3 keV on the light detector. The resolution of this detector at these energies is 126.5 ± 9 keV.

possibility of such a cross talk. The read out current runs in fact from one Al pad on the end of the thermometer to the other perpendicularly to the gold strip placed in the middle. If the bond spot is not perfectly perpendicular a voltage drop across the film can be created thus coupling the heater current into the readout circuit.To increase the sensitivity of the light detector and eliminate such problems a completely new thermometer geometry [Fra02, Pet] was developed as will be discussed in the last section of this chapter.

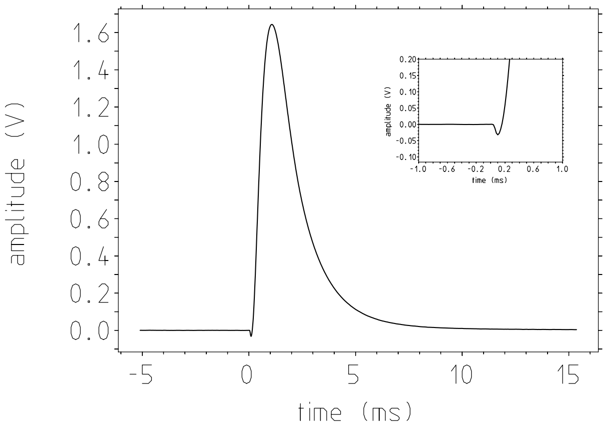

Figure 5.9: Light detector test pulse. In the insert the effect due to the cross talk is blown up.

A 13.8 h measurement was performed without source. The scatter plot of the coincident events on the phonon channel and on the light detector is shown in figure 5.10. The light emission associated with an alpha interaction results to be

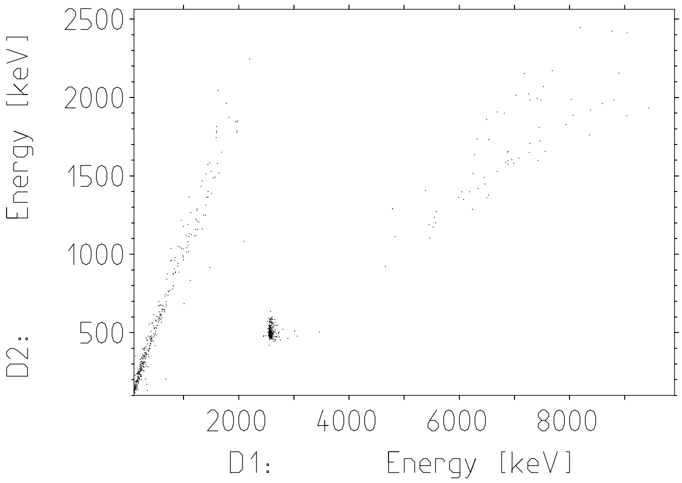

Figure 5.10: Run 19: 13.8 h background measurement. On the x-axis the energy of the phonon channel is plotted while on the y-axis the corresponding electron equivalent energy of the light detector is given. The lower band groups events originating from alpha interactions and the measured quenching factor is ∼ 5.6.

quenched by a factor ∼ 5.6. In particular an alpha contamination at an energy of about 2.6 MeV is present with a count rate of ∼ 15 counts/h. The fit of this peak is shown fig. 5.11 on the left side. On the right side the same peak as measured on the light detector is shown.

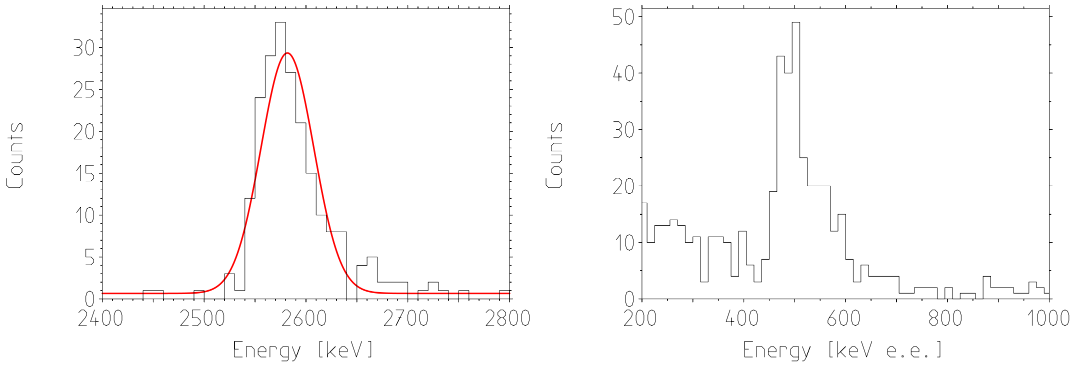

Figure 5.11: Fit of the alpha peak on the phonon detector. The fitted position results at 2580 ± 2 keV. On the right plot the corresponding peak resulting at ∼470 electron equivalent keV on the light detector is shown.

The origin of this contamination is yet unclear. It is present in all $CaWO_4$ crystal measured so far, showing different count rates. This excludes any hypothesis related to W isotopes. Run 18 in fact showed a count rate of about 30 counts/h for the same contamination. There are not many candidates that are alpha unstable having such a low Q value. The most favourable candidates are naturally occurring isotopes, ^{147}Sm, ^{186}Os and ^{174}Hf. The latter one has however an isotopic abundance of only 0.16 % and an half life of 2 × 10^{15} y. Therefore to produce a count rate of 30 counts/h a contamination of 0.22 g of this isotope in the crystal and therefore a presence of 140 g of natural Hf is required! The same applies for ^{186}Os which has 1.58 % isotopic abundance and an half life of 2 × 10^{15} y. The high amount of contaminants needed to be present in the crystal to produce such a rate completely excludes these elements as candidates. ^{147}Sm instead has an isotopic abundance of 15.0% and has shorter half life time, $t_{1/2} = 1.06 \times 10^{11}$, compared to the previous candidates. It results that 4.02×10^{16} atoms or 1.003 $\times 10^{-5}$ g of ^{147}Sm are needed in a crystal to produce a rate of 30 counts/h. This would translate in a contamination of 6.86 $\times 10^{-5}$ g of natural Sm in the crystal.

In table 5.1 a list of possible candidates is reported. However since these isotopes are not naturally occurring (except ^{147}Sm), a convincing mechanism for their production in the crystal should also be found to consider them as candidates. Numerical simulations have shown that, among others, ^{146}Gd would be produced by cosmic activation on natural W [Ram00]. This isotope decays via electron capture (EC) with a half life time of 48.3 days into ^{146}Eu, which in turn decays again via EC with 4.6 d half life time into ^{146}Sm which is alpha unstable and has a Q-vaule of 2529 KeV. This short chain ends in the stable isotope ^{142}Nd.The observed count rate is in any case too high to attribute the origin of such a contamination to cosmic activation. Since the uncertainty on the energy calibration at higher energies is rather high, ^{147}Sm remains the best candidate so far.

Table 5.1: Candidates for the alpha contamination of energy from 2 MeV to 3 MeV. The assumed count-rate for these calculations is 30 counts/h. In case the contamination is internal, CRESST detectors would measure the whole decay energy, i.e. the Q-value. In case of superficial contamination a double structure corresponding to the energy carried by the alpha and to the Q-value is to be expected [Ale97]. Half life times and energies have been taken from reference [LBN].

Isotope	Half life [y]	E_{alpha} [keV]	Q-value [keV]	Contamination [n. of atoms]	Contamination [g]
^{147}Sm	1.06×10^{11}	2233	2310	4.018×10^{16}	1.003×10^{-5} ($6.86 \times 10^{-5}$of natural Sm)
^{154}Dy	3×10^{6}	2872	2947	1.13×10^{12}	3×10^{-10}
^{150}Gd	1.79×10^{6}	2726	2809	6.78×10^{11}	1.77×10^{-10}
^{146}Sm	1.03×10^{8}	2455	2529	3.905×10^{13}	9.75×10^{-9}

5.1.3 Run 20

In this run a Phase II detector module together with the two sapphire detectors described in Chap. 4 for the Dark Matter run were implemented. The energy spectra of the two sapphire detectors were analysed in order to check any change in the radioactive background level by comparing them to the background measurements obtained for the first Phase of CRESST. This will be discussed at the end of this subsection.

For the Phase II detector module the same light detector used in run 19 together with a new $CaWO_4$ crystal from an Ukrainian supplier were employed. A 0.3 μm buffer layer of SiO_2 was evaporated on the crystal below the tungsten film lowering the transition temperature to ∼15 mK. The dimensions of the thermometer were reduced to 4×6 mm. The low T_C is expected to decrease the heat capacity and thus achieve a lower threshold. The film geometry was standard but the two Al pads evaporated at the side of the gold strip which are usually serving as heater contact pads came off while bonding at Gran Sasso. Therefore the alternative bonding scheme shown in fig. 5.12 had to be used. The gold wire was bonded from the heater copper pad on the holder to the gold strip in the middle of the thermometer and then directly to the holder. The other heater copper pad used to connect the superconducting wires to inject the current was grounded. As already mentioned, any misalignment between the gold strip and the bond stitch can give rise to a cross talk between the heater current and the bias current and this risk is increased with this kind of bonding scheme.

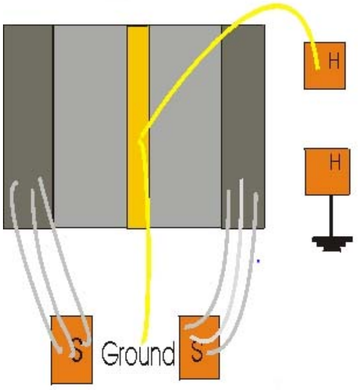

Figure 5.12: Run 20: bonding scheme for the thermometer on the $CaWO_4$ crystal. From the heater pad on the holder the gold wire is bonded to the gold strip and then directly to the copper holder. The other heater pad on the holder is grounded as well.

The detector was operated with 3 μA bias current and the corresponding transition curve is shown in fig. 5.13. The transition was highly non-linear and the operating point was chosen on the upper part of curve as indicated by the

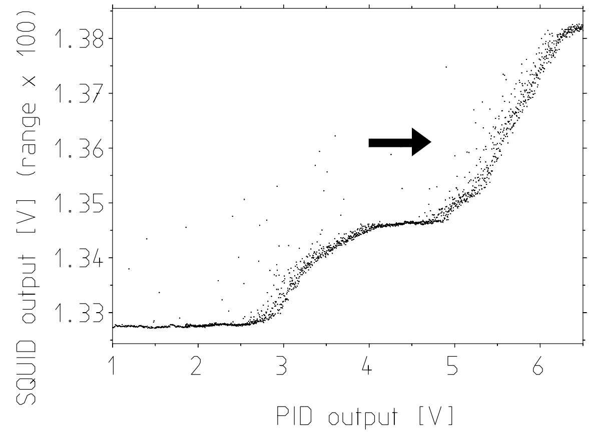

Figure 5.13: Phonon channel transition curve. The detector was operated with 3 μA bias current and the operating point was chosen in the upper part of the transition as indicated by the arrow.

arrow on the plot. With this thermometer the problem with the test pulse shape disappeared, and the fraction of the non thermal component was constant in the whole range as shown in fig. 5.14. However the dynamic range extended only to about 0.25 V measured pulse height, corresponding to about 600 keV. This is shown in fig. 5.15. All alpha events saturate, therefore a new analysis method exploiting the time duration of the pulse was developed. A template is averaged from pulses in the low energy region (in this case from the ^{57}Co peak) where the detector still is in the linear regime, i.e. until the root mean square deviation of the measured pulses from the fitted template does not start to rise with energy. As an example the logarithm of the RMS deviation of the pulses from the template

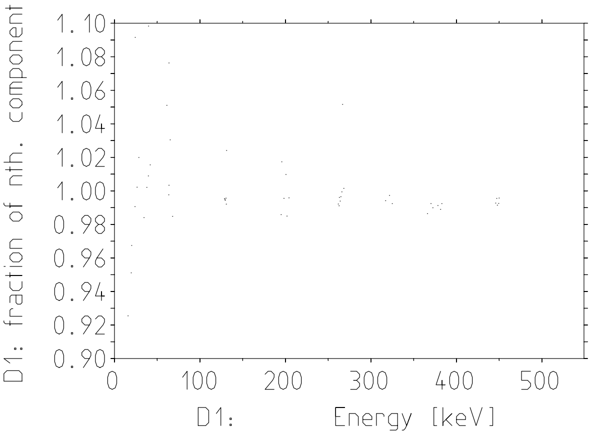

Figure 5.14: Dependence of the non thermal component versus energy for the heater pulses in the phonon channel. The non thermal fraction remains constant for the whole dynamic range and equal to the value fitted for particle pulses.

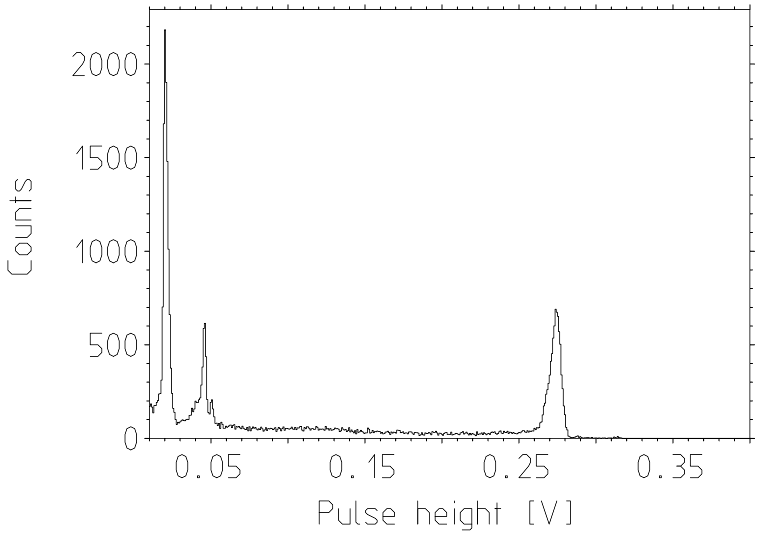

Figure 5.15: Run 20: ^{57}Co calibration measurement: measured pulse height spectrum of the phonon channel. Above 0.25 V all events are saturated. At around 0.05 V the 122 keV and 136 keV peaks from the source are visible. The higher peak at their left is the 46 keV gamma peak from a ^{210}Pb contamination present in the crystal.

for the calibration measurement of run 20 is shown in fig. 5.16. Above 0.06 V the value of the deviation is changing. Due to the non linear response the pulse shape deviates from the template shape, resulting in an increase of the RMS value with energy. For all measured pulses below this point, the fitting procedure is standard.

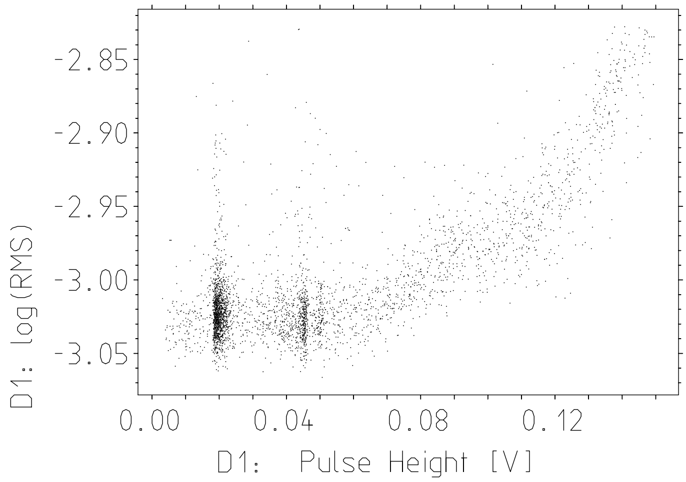

Figure 5.16: Logarithm of the RMS value of the data from the template fit over pulse height. The structure at 0.02 V is 46 keV peak from the internal ^{210}Pb contamination, while the other two are the ^{57}Co emission lines. Above 0.06 V the detector nonlinearities result in a pulse shape change and thus a change in the RMS value.

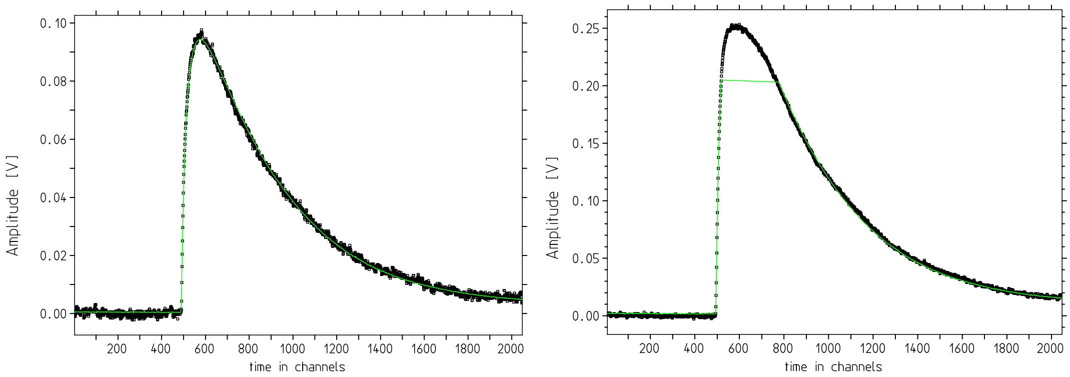

Figure 5.17: Fit of the $CaWO_4$ events with a template obtained averaging pulses from the 122 keV peak. The fit is truncated at 0.2 Volts. For pulses of amplitude below this value the fit procedure is standard (left plot). For pulses with amplitude exceeding this value, the higher part of the pulse shape is distorted due to saturation. Therefore the fit is truncated and the amplitude of the pulse is reconstructed from the template.

For all the pulses whose measured pulses height exceeds the chosen value, the fit is truncated at the chosen value as shown in fig. 5.17 and the upper part of the pulse is reconstructed from the template. This procedure gave very promising results as will be shown in section 5.2. To apply this method a longer time window which includes the decay of saturated signals needs to be recorded. Unfortunately this crystal showed a very high count rate due to contamination from the natural chains (see below) which caused pile-up problems. Therefore the longer the time window, the more severe was this problem. Eventually a record length of 2048 channels and a time base of 40 μs was chosen. Part of the needed information from the decay time was missing as can be seen in fig. 5.18. The fit was truncated

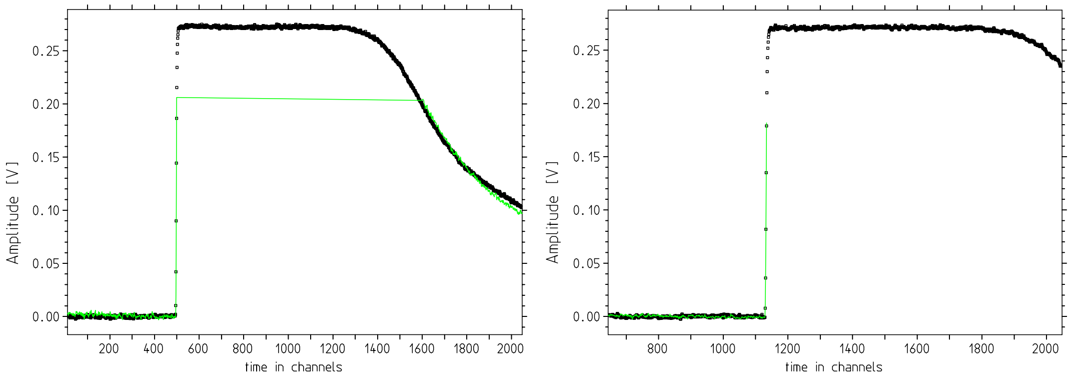

Figure 5.18: In this figure two examples of high energy events are shown. The higher the energy, the longer the time the pulse spends in the saturation region. Therefore, if the recorded time window is not large enough, the necessary information is missing and the fit procedure fails as happens in the example on the right.

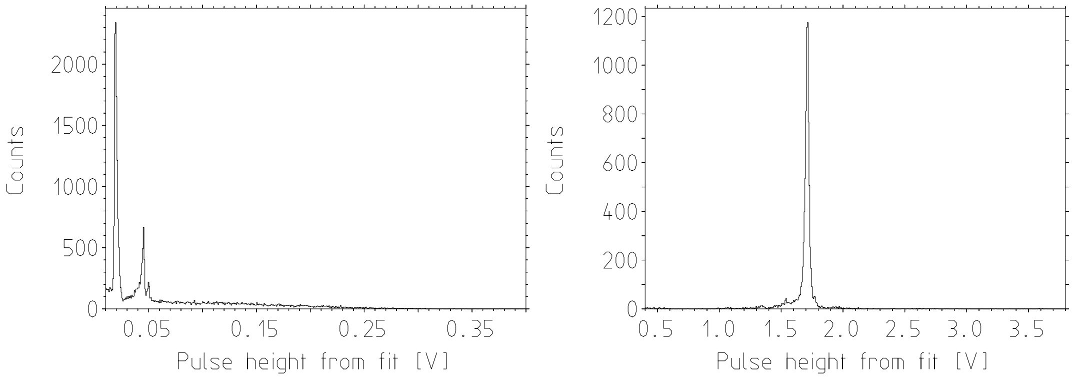

Figure 5.19: Run 20 calibration measurement shown also in fig. 5.15. Here the pulse height of the saturated pulses has been reconstructed with the truncated fit procedure. The structure at around 1.7 Volts originates from alpha contaminations from the natural radioactive chain of ^{238}U.

as high as possible, i.e. at 0.2 V just below the saturation region, however the incompleteness of information significantly worsens the energy resolution. The pulse height spectrum reconstructed with this procedure is shown in fig. 5.19. Another problem in applying this method to analyse this run was that the test pulses were injected only within the dynamic range and not in the saturation region. Therefore no real check of this procedure could be performed in this run. Furthermore the energy calibration was performed with a ^{57}Co source and due to absence of test pulses above 600 keV, the only way to extrapolate the energy calibration was to make a linear fit of the detector response as shown in fig. 5.20.

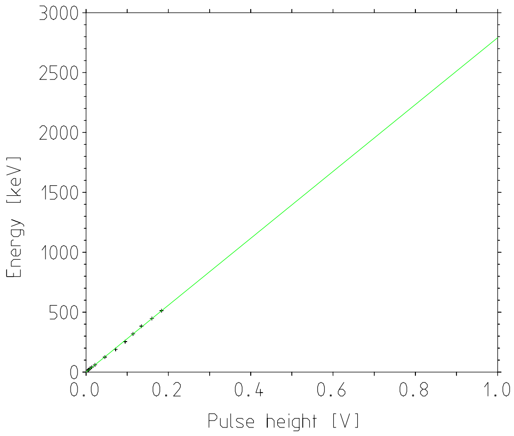

Figure 5.20: Run 20: energy versus measured pulse height. Since the test pulses are injected up to only 600 keV the extrapolation of the calibration could be performed only with a linear interpolation.

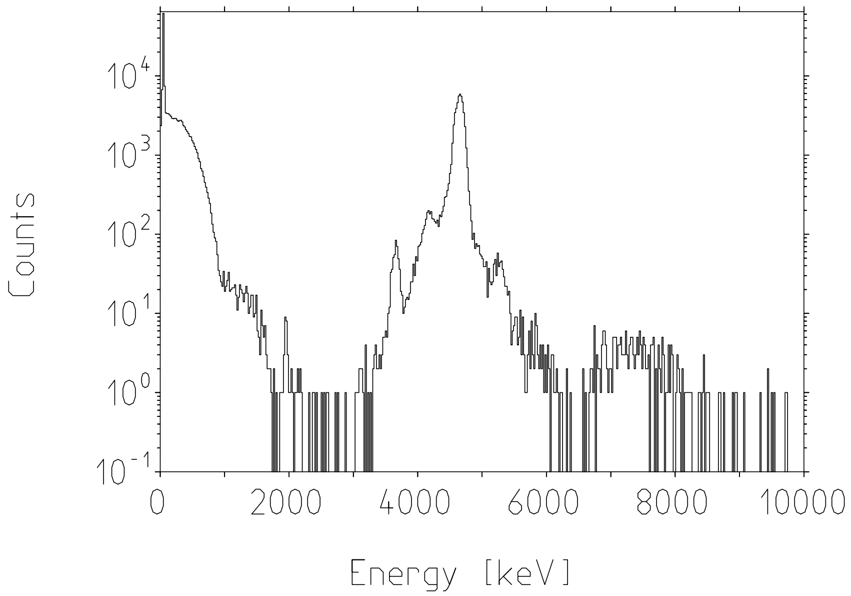

Figure 5.21: Run 20: $CaWO_4$ measured energy spectrum. A contamination of about 1.2 Bq/kg of ^{210}Pb is present inside the crystal (see text).

The energy spectrum obtained with a 59.12 h live time measurement is shown in fig. 5.21 in logarithmic scale. The crystal shows an overall count-rate of almost 1 Hz above 10 keV, of which about 0.25 Hz are due to alpha contaminations and ~0.7 Hz arise from gamma and beta interactions. The spectrum is dominated by ^{210}Pb decay features. This isotope beta decays to ^{210}Bi with a Q-value of 63 keV. The beta spectrum has an end point at 17 keV with 84% B.R. and at 63 keV with 16 % B.R. Therefore the decay is accompanied by a 46 keV gamma

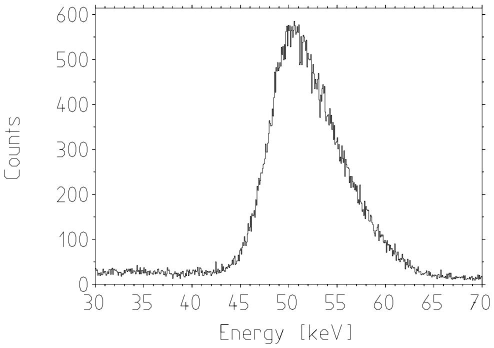

Figure 5.22: Run 20: ^{210}Pb characteristic peak measured on the $CaWO_4$. The 46 keV gamma emission line is broadened to the right side by the 17 keV end point beta spectrum.

emission, which in the spectrum results to be broadened on the right hand side by the 17 keV beta spectrum as shown in fig. 5.22. The count-rate in this peak is of about 0.28 Hz. ^{210}Bi is a pure beta emitter with the Q-value of 1.17 MeV. This beta spectrum can be observed in fig. 5.21 and again the count-rate from about 70 keV to 1.2 MeV is $\sim$ 0.3 Hz. At its right another beta spectrum is visible. This is probably due to the beta decay of $^{234(m)}$Pa (also from ^{238}U chain) whose spectrum has an end point at 2.27 MeV with 98 % B.R.. The presence of this contaminant was found also on anther CaWO$_4$ crystal produced by the same company as shown in the last table of the appendix. At about 2 MeV again the ^{147}Sm alpha peak is present but in lower amount showing only 0.4 counts/h. The energies of the alpha peak are misplaced as mentioned above. ^{210}Pb beta decays to ^{210}Bi which in turn alpha decays with 100% B.R. into ^{206}Pb with a Q-value of 5.4 MeV. Therefore it is reasonable to expect that the most intense peak on the spectrum is associated to this decay. The alpha energies are thus misplaced by about 800 keV towards lower energies. Taking this peak as reference point, the other two peaks at its left are due to the 4.27 MeV alpha decay energy of ^{238}U and the 4.8 MeV from Th230+Ra226 alpha decays, in agreement with the presence of $^{234(m)}$Pa.

Indeed assuming that the lowest peak is due to the ^{147}Sm alpha decay at 2.3 MeV and calibrating the spectrum from this line, the highest peak results at 5.4 MeV and the most resolved peak at its left results at 4.27 MeV, corresponding to the Q-value of ^{238}U decay. This is shown in fig. 5.23 and is a first confirmation of ^{147}Sm being the contaminant.

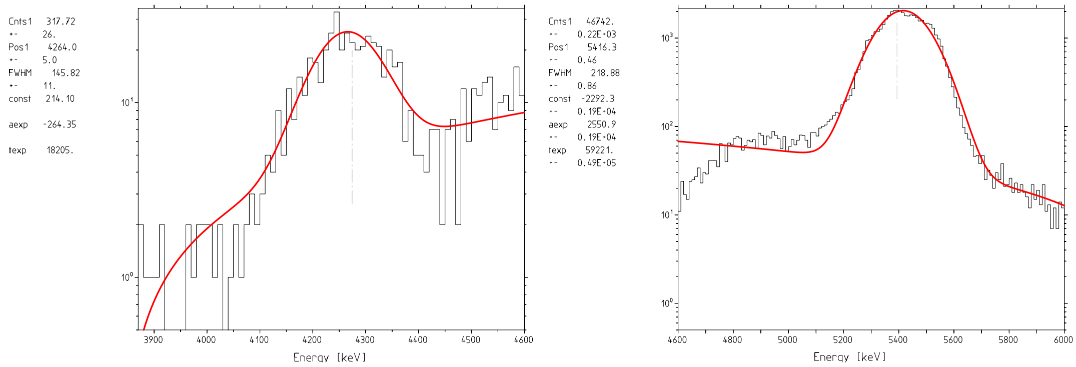

Figure 5.23: Same spectrum as shown in the previous figure, now calibrated from the 2.3 MeV alpha peak (corresponding to the Q value of ^{147}Sm alpha decay). The highest peak results at 5.416± 0.46 MeV as expected (see text) and the peak on the left results at 4.264 ± 0.5 MeV which corresponds to the Q value of ^{238}U. This is a first verification of the hypothesis of the presence of ^{147}Sm.

Finally the scatter plot of this measurement is shown in fig. 5.24. Due to the substantial pile-up several cuts on the rise time, decay time and on the baseline difference before and after the pulse have been applied. The events lying between the electron recoil band and the alpha band are due to misplaced saturated pulses due to the lack of information about their decay time.

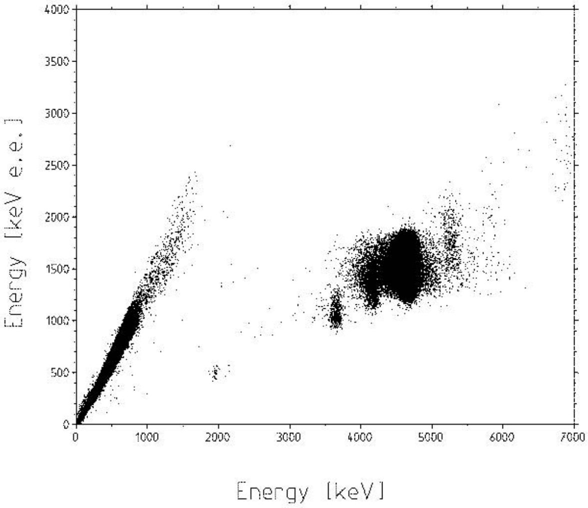

Figure 5.24: Run 20: scatterplot of the 59.12 h measurement shown in the previous pictures. Due to a substantial pile up and to the too short time window of the recorded pulses, the spectrum reconstructed using the procedure of truncating the fit (see text) has a bad energy resolution which causes an enlargement of the alpha band.

Sapphire results

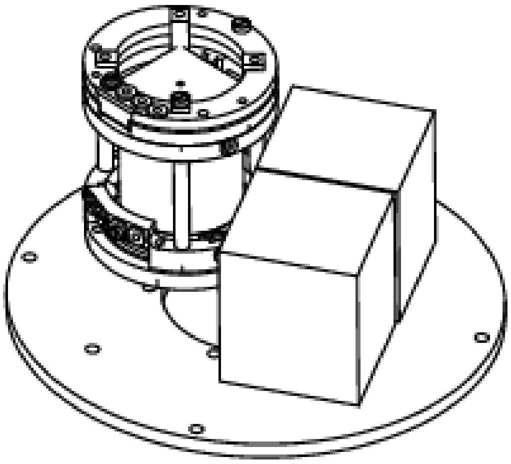

Figure 5.25: Run 20: set-up. The two cubes represent the two sapphire detectors. They are both directly facing the Phase II module.

The purpose of this measurement with the sapphire detectors was to monitor the radioactive background of the cold box after disassembling and reassembling the whole set-up for the move. However, due to the strong contamination on the $CaWO_4$ crystal, a direct comparison with the background level measured for Phase I is difficult. The two crystal were lying adjacent both facing the Phase II module as shown in fig. 5.25. Crystal V described in table 4.2.2 was connected to the read-out channel 3 and crystal VIII (table 4.2.3) was connected to channel 4. The first showed 100% triggering efficiency at 1 keV as shown in fig. 4.9 and the latter at 3.5 keV. The observed count rate after removing all true coincident events (see 4.15) and applying a PSD cut is reported in table 5.1.3 and compared with run 15 and 16 results. In the energy interval from 15 to 25 keV the count rate is a factor of 2 higher than for Phase I on both crystals. Below 10 keV the rate is similar, but always higher that in Phase I. Both detectors again show the 5.9 keV structure with the same count rate (about 7 counts/crystal/day) as before the move. This is shown in fig. 5.26. Both detectors have been calibrated with the procedure described in Chap. 4 but the test pulses were not monitored. Therefore the correction for pulser non linearities is not included and the peaks are shifted to higher energy as in run 15.

	Run 15	Run16	Run 20	
Crystal number:	V (ch1)	VIII (ch4)	V (ch3)	VIII (ch4)
kg days:	14.92	1.51	1.31	1.31
Energy interval keV	rate counts/kg/keV/day			
5 to 10	9.23 ± 0.35	7.82 ± 1.02	10.64 ± 1.27	11.43 ± 1.32
10 to 20	1.94 ± 0.11	1.72 ± 0.34	3.95 ± 0.54	2.06 ± 0.40
15 to 25	1.41 ± 0.09	0.73 ± 0.22	3.11 ± 0.48	1.29 ± 0.31
20 to 50	0.83 ± 0.04	0.48 ± 0.10	1.85 ± 0.21	1.34 ± 0.18
50 to 100	0.39 ± 0.02	0.38 ± 0.07	1.11 ± 0.13	0.88 ± 0.12
90 to 130	0.40 ± 0.02	0.21 ± 0.06	0.87 ± 0.13	0.59 ±0.10

Table 5.2: In this table the background count-rate in counts/kg/keV/day is compared for two different crystals before and after the move. As described in Chapter 4 crystal VIII was rotated in its holder (run 16) such that the teflon tips did not contact the points were microcracks had been observed, while this was not the case for crystal V in run 15. Therefore the crystals have been reused in the same conditions in order to provide a comparison as direct as possible. From 15 to 25 keV the count rate after the move a factor of 2 higher than for Phase I for both crystals. Crystal V shows a higher count rate than crystal VIII both before and after the move.

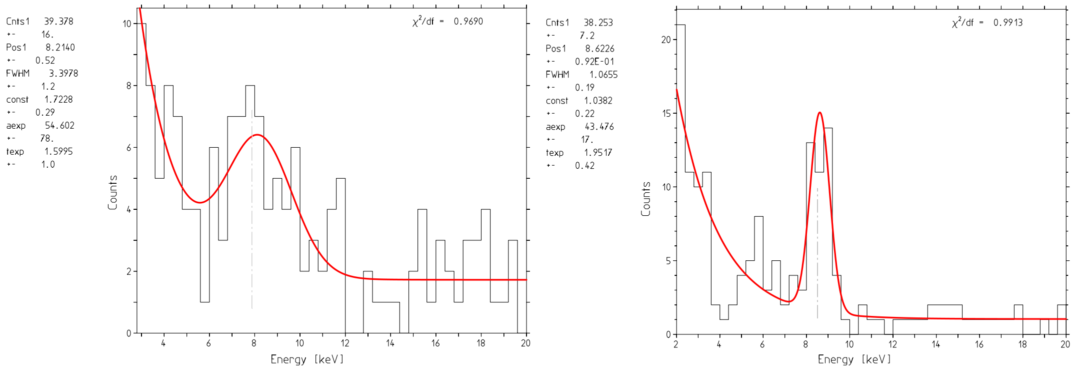

Figure 5.26: Fit of 5.9 keV line already observed in all the runs of Phase I using sapphire detectors. Again the measured count-rate is of about 7 counts/ crystal/ day as before the move.

5.2 Status

Light detector: substantial effort has been devoted to realise a more sensitive light detector [Fra02]. To increase the sensitivity, the heat capacity has been reduced while the collecting area of the thermometer has been kept constant using superconducting phonon collectors while reducing the area of the tungsten thermometer. These phonon collectors absorb the non-thermal phonon without contributing to the heat capacity of the thermometer. For phonon collectors with dimensions below 1 mm the whole energy may be transmitted to the thermometer with negligible losses [Loi99]. Therefore the thermometer design has been optimised as sketched in fig. 5.27 [Fra02, Pet]. With such a small thermometer

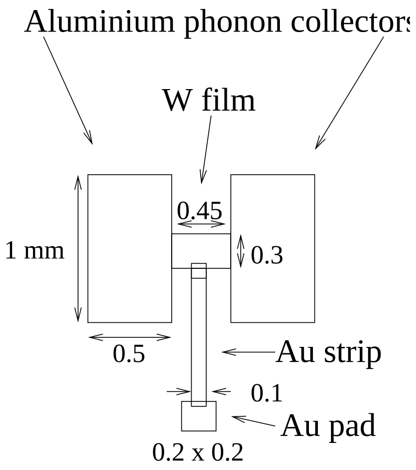

Figure 5.27: New light detector design [Pet]. The thermometer has been reduced in size and provided with superconducting phonon collector. The gold strip serves as heater and defines the coupling strength.

size, also the heater geometry had to be changed. In case of very small films in fact the gold bond wire needed for the heater and the thermal grounding would dominate the heat capacity. Also the thermal coupling strength G is determined by the bond wire and cannot be appropriately reduced. If the heat capacity is reduced and G remains constant, the relaxation time is no more long enough to integrate the energy flux of non-thermal phonons thus resulting in a loss of sensitivity. Therefore the bond wires have been replaced by a an Au film heater as shown in fig. 5.27, providing a smaller heat capacity defining at the same time a weaker coupling strength [Fra02]. In fig. 5.28 the measured pulse height from the "old" light detector is compared to the new one. The same Hungarian $CaWO_4$ crystal has been used for these two measurements carried out in Gran Sasso. As can be observed in the figure for the same measured amplitude on the phonon channel (corresponding to about 60 keV) the signal on the new light detector is about three times higher.

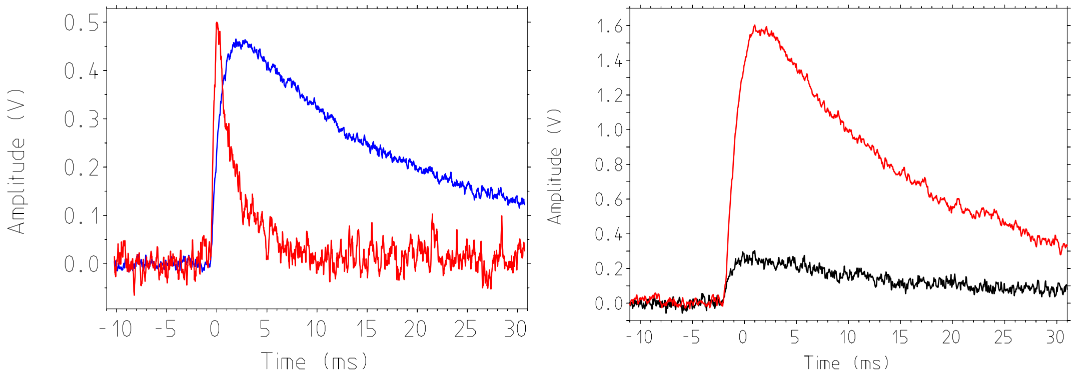

Figure 5.28: Run 21 and 22: the same Hungarian $CaWO_4$ (crystal D) has been mounted together with a light detector with the old design (left) and with the new one (right).The darker line is the measured signal on the phonon channel corresponding to about 60 keV energy deposition. On the right plot the signal on the light detector associated to the same light output is about three times higher.

$CaWO_4$: concerning the scintillator, the light output at room temperature of the different crystals has been measured [Don]. The best light output (comparable to a NaI) was obtained with the Ukrainian crystal used in run 20, which had the drawback of being highly contaminated with ^{210}Pb. The Hungarian crystals, on average more transparent and less contaminated than the Ukrainian ones, showed at least a factor of two lower light output. The reasons for this behaviour are under study. A set-up to investigate the scintillation properties of these crystals at 4 K temperature is also in preparation.

Two different new crystals from the Hungarian provider have been measured in the Gran Sasso set up and their radioactive background has been studied. In fig. 5.29 their alpha background spectrum in counts/day/kg/10keV is compared. The plot on the left, from the crystal used in both run 21 and 22 with different light detectors, shows a much lower contamination from the natural radioactive chains. The spectrum from the second crystal, discussed below, is blown up in fig. 5.30. To determine the pulse height the method using the truncated fit has been applied on both detectors. The best energy resolution obtained so far is about 13 keV at the 1.1 MeV peak from a ^{60}Co source and about 17 keV at the 2.3 MeV alpha peak (crystal D on the figures).

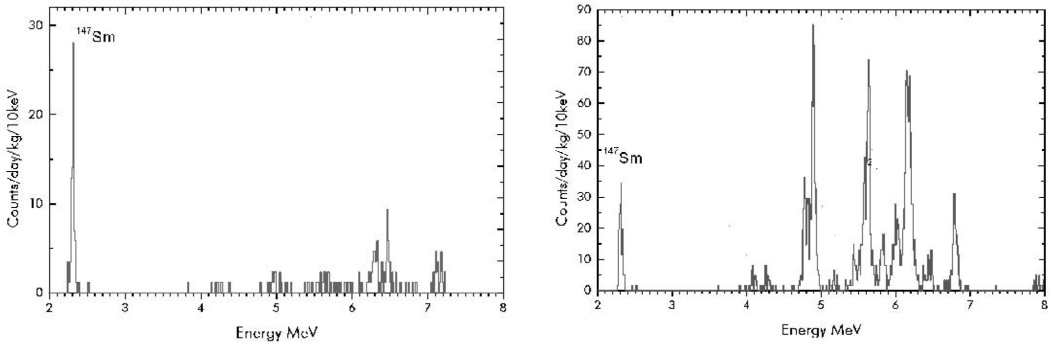

Figure 5.29: Alpha spectrum of the Hungarian crystals D (left) and B (right). Crystal B shows is contaminated with the natural chains of ^{238}U and ^{232}Th. This is shown in detail in the next figure.

On the Hungarian crystal B, alpha structures due to the ^{238}U and ^{232}Th natural chains are measured(see fig. 5.30). The contribution from the upper part of the U chain above ^{226}Ra is rather small while a contamination of about 5 mBq/kg of ^{226}Ra has been identified. ^{226}Ra has a half life of $t_{1/2} = 1620$ y while all the daughter nuclei until ^{210}Pb have much shorter life times as illustrated on the figure. Therefore they quickly reach an equilibrium state and thus decay with the same rate as ^{226}Ra. ^{210}Pb instead has a half life time of $t_{1/2} = 22$ y. Therefore the lower part of the chain below ^{210}Pb is almost absent. The measured quenching factor for the alpha contamination on this crystal is of 4.3 as shown in fig. 5.31. However this depends strongly on the correctness of the energy calibration. As discussed for the previous runs the energy extrapolation with test pulses to such high energies has not yet converged to a reliable procedure. Since there is no other convincing explanation rather than ^{147}Sm for the alpha contamination above 2 MeV, this peak has been used to calibrate both spectra. As came out already in run 20, the consistency on the expected rate and position of the identified peaks strongly favours this hypothesis.

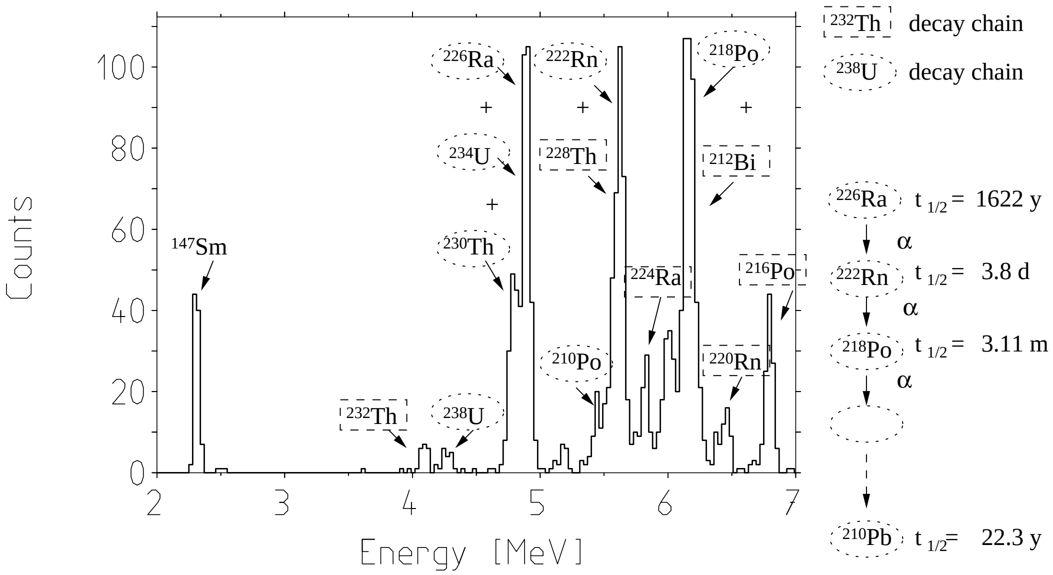

Figure 5.30: Run 22: Alpha spectrum of the Hungarian crystal B. Besides the presence of the ^{232}Th and of the upper part of the ^{238}U chains, a contamination of ^{226}Ra of about 5mBq/kg has been identified. As sketched on the right of the figure ^{226}Ra has a relatively long half life time. Therefore it quickly reaches (∼days) an equilibrium state with the daughter nuclei which then decay with the same rate of ^{226}Ra until ^{210}Pb. This has instead a half life of 22 years. Therefore the ^{210}Po peak is very small.

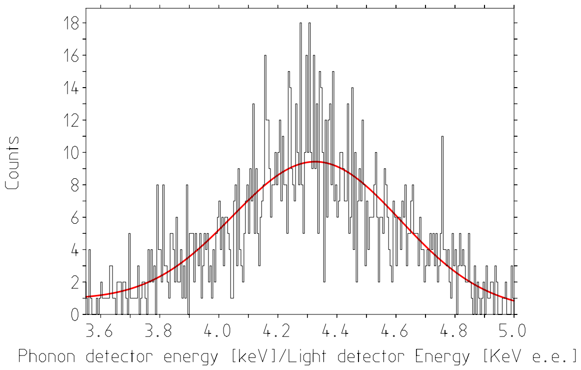

Figure 5.31: Run 22: Ratio of phonon/light energy for the alpha band. The ratio of phonon/light energy for the electron recoils is normalised to 1 and the light emission due to alpha interaction results to be quenched by a factor of 4.3.

5.3 Next steps

So far due to technical problems or to unexpectedly high background rate no Dark Matter data have been taken. A full characterisation of the detector behaviour, prior to any Dark Matter consideration, is therefore still under study. However, in the current run 22 few days of measurement have been analysed with the discovery of some events in the phonon channel with no associated light emission. These are shown in fig. 5.32 and they have a rate of about 10 counts/kg/ day.

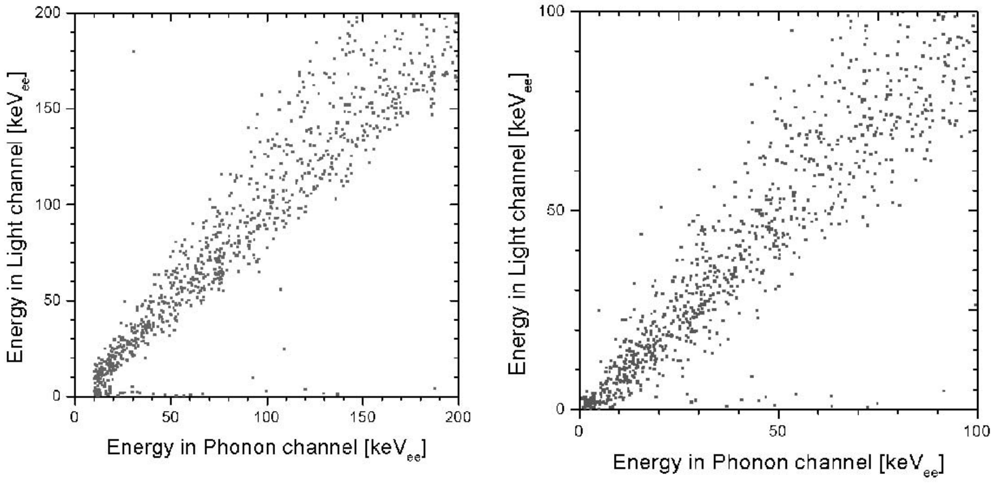

Figure 5.32: Run 22: scatter plots of the measured spectra on crystal D (left) and crystal B (right). A few events on the phonon channel resembling in shape particle events but with no light emission associated have been identified. They show a count rate of about 10 counts/kg/day. Their origin still has to be clarified. Since some damages have been observed on the crystals, very likely they result from the formation of damages in the crystal due to the mounting.

The nature of these events is yet unclear, but after the experience with the sapphire detectors (see Chap.4.2.1) it is very likely that they are caused by the holding system. In fact again some damage has been observed at the contact points with the teflon tips, and a new design for these tips has been studied. These will be implemented in the next run. In parallel, new crystal providers have been contacted and a study on the radioactive contaminants on different crystal powders used to grow them has been undertaken. Finally a calibration with a source emitting high energy gammas such as the 2.6 MeV line from ^{232}Th is planned to thoroughly study the radioactive background and a calibration procedure which allows the extrapolation to the alpha region. Though these energies are not in the region of interest for Dark Matter a complete identification of the radioactive background can be very helpful for developing methods to reduce it.

Chapter 6

Conclusions and Perspectives

6.1 Conclusions

In this work the suitability and the high potential of CRESST in the Dark Matter direct detection have been demonstrated. CRESST Phase I used 262 g sapphire crystals as a target medium and the goals of a low background, long-term stable cryogenic operation, low energy threshold and thus good sensitivity for low mass WIMPs were fully achieved. In a measurement lasting about three months and acquiring $\sim$ 15 kg days of data a low radioactive background was achieved and the long term stability of operation of CRESST detectors was demonstrated. In this run two detectors were working, showing a background of 1.94 ± 0.11 counts/kg/keV/day in the energy interval from 10 to 20 keV and dropping below 1 between 25 to 50 keV and below 0.4 above 50 keV. One detector revealed a ^{210}Pb surface contamination. A structure around 103 keV, corresponding to the energy of the nuclear recoil of ^{206}Pb daughter nucleus following the ^{210}Pb α decay, was found. This would translate in a direct measure of a quenching factor equal to 1 in the specific case of sapphire. The low statistics of this measurement however did not allow a strong conclusion. A systematic error in the energy extrapolation procedure due to pulser non-linearities was also identified in this run and a method to correct for these non-linearities was applied. The reliability of the monitoring and the calibration procedure were then investigated with a dedicated run. A low activity ^{57}Co source was mounted inside the cryostat directly facing the crystals . The 14.4 γ line and the 6.4 keV Fe X-ray line produced by this source were fitted at $15.16^{+0.09}_{-0.09}$ and $6.70^{+0.07}_{-0.05}$ keV respectively, with the fit errors corresponding to 90% C.L. This systematic shift to higher energies in the threshold region puts CRESST Phase I Dark Matter limits on the conservative side. In a very stable run of 1.51 kg days of data with a background level below 1 count/kg/keV/day above 20 keV and a very low energy threshold of 580 eV were achieved. This run was used to set Phase I Dark Matter limits. The detector was 100% efficient above a software threshold of 600 eV. A pulse shape cut with a retention efficiency of 100% for good events at all energies was applied and events in coincidence with an adjacent detector were removed. A coincidence rate of 17% was found. Considering that only two detectors were active in this run and only one face out of six was facing the other crystal, this is consistent with all events being background. The background level was below 1 count/kg/keV/day above 20 keV, falling to about 0.3 at 100 keV. Sapphire detectors are especially sensitive for low-mass WIMPs with spin dependent interaction and improve on existing limits in this region.

First measurements with the CRESST Phase II detector module were performed at the Gran Sasso set up and analysed. Despite many technical problems faced during these first tests, the module showed high discrimination potentials and alpha contaminations were clearly separated from the gamma interaction band. A fit procedure which reconstructs the pulse height of saturated pulse was investigated achieving an energy resolution of about 13 keV at the 1.1 MeV peak from a ^{60}Co source and about 17 keV at the 2.3 MeV alpha peak. The radioactive background of the measured $CaWO_4$ crystals was studied, identifying a ^{210}Pb internal contamination of about 1.2 Bq/kg on the Ukrainian crystal and a ^{226}Ra contamination of about 5 mBq/kg on a Hungarian one. The radioactive background level of the CRESST cold box after the move was also investigated using two sapphire crystals. In the energy interval from 15 to 25 keV the count rate resulted in a factor of 2 higher than for Phase I on both crystals.

6.2 Perspectives

So far due to technical problems or to an unexpectedly high count rate, no Dark Matter data have been taken. For the near future several measurement with different crystals will be performed until the module behaviour will be fully understood and a Dark Matter run will be performed.

An upgrade of the experimental set-up from 4 to 66 readout channels is then planned for next year. The number of running modules will be increased up to 33 modules for a total mass of 10 kg. All modules will fit in the present cold box without need of modifying the cryostat. The projected sensitivity of CRESST Phase II for a 10 Kg $CaWO_4$ detector and 3 years of measurement is shown in fig. 6.1.

The results discussed in this thesis showed the reliability and stability of operation of CRESST over long periods of time and the first results obtained with the Phase II detector module showed the high potential of the 300 g module. Therefore exciting physics results can be expected in the coming years.

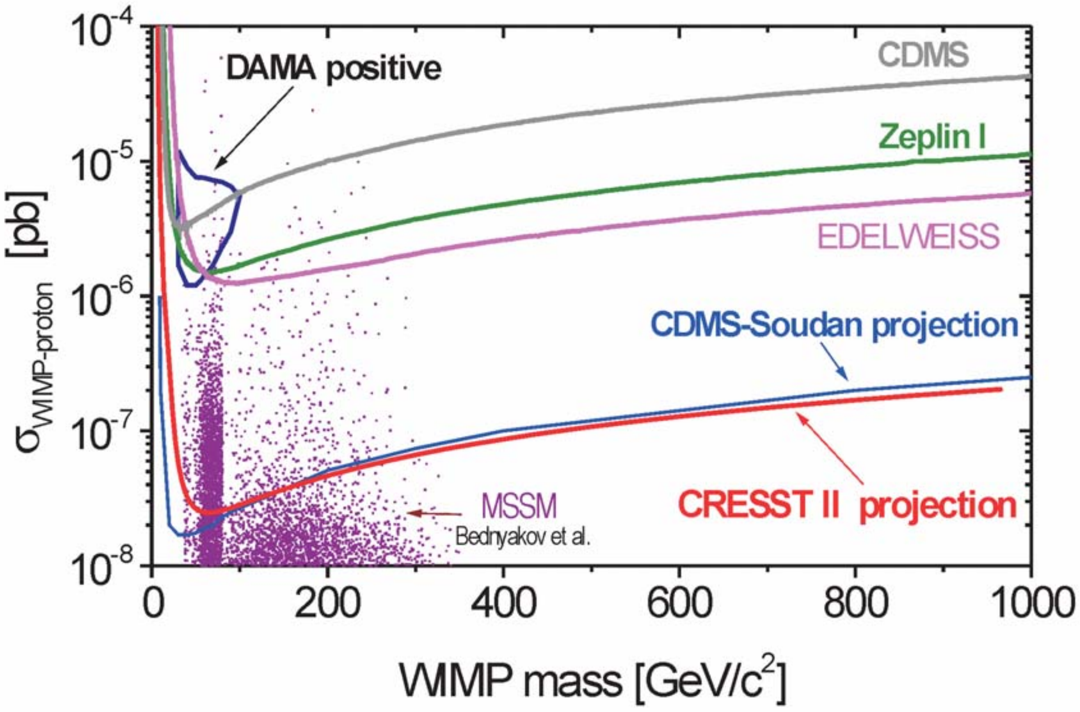

Figure 6.1: WIMP-nucleus cross section limits (90% CL) for coherent interactions as a function of the WIMP mass. CRESST II limit represents the projection expected for a background level of 1 count/keV/kg/day, a rejection efficiency of 99.7% above 15 keV and 30 kg years of measurement. For a comparison the DAMA (with the contour for positive evidence) and the most recent CDMS, ZEPLIN and EDELWEISS results (see Chap.1) are shown. The projection for CDMS in the Soudan mine is also drawn. As shown in this figure, the expected sensitivity of CRESST Phase II covers a significant part of the MSSM parameter space.

Appendix A

Sample measurements with γ spectroscopy

Table A.1: Sample: Sapphire crystal $4 \times 4 \times 4.1$ cm^3

Date of measurement: October 1998
Measurement live time: 617.60 h
Sample Mass: 262 g

Decay Chain	Energy	Element	Activity or upper limit at 95% C.L [mBq/kg]
^{232}Th	2614.47	^{208}Tl	<4.8
-	1460.75	^{40} K	<46.7
-	661.60	^{137}Cs	<2.3
^{238}U	609.31 1764.50	^{214}Bi	<3.1
-	1173.21 1332.47	^{60}Co	<1.3

Table A.2: Sample: $CaWO_4$ crystal

Date of measurement: February 1999
Measurement live time: 303.4 h
Sample Mass: 304.799 g

Decay Chain	Energy	Element	Activity or upper limit at 95% C.L [mBq/kg]
^{232}Th	583.14 911.20	^{208}Tl ^{228}Ac	<5.7
-	1460.75	^{40} K	<41.5
^{238}U	351.99 609.31 1764.50	^{214}Bi	< 9.9
-	1173.21 1332.47	^{60}Co	<1.4

Table A.3: Sample: 5 $CaWO_4$ substrate crystal , $(20 \times 10 \times 5)$ mm^3 each

Date of measurement: February 2001
Measurement live time: 572.914 h
Sample Mass: 30.5 g

Element or Decay Chain	Activity or upper limit at 95% C.L [mBq/kg]
^{232}Th	<14.7
^{238}U	< 13.5
^{40} K	213 ±90
^{60}Co	< 7.3
^{137}Cs	< 9.2

Table A.4: Sample: material for butyl o-ring

Sample: material for butyl o-ring
Date of measurement: February 2001
Measurement live time: 475.917 h
Sample Mass: 2.3 g

Element or Decay Chain	Activity or upper limit at 95% C.L [mBq/kg]
^{232}Th	149 ±35
^{238}U	362 ±41
^{235}U	<73
^{40} K	(3.4 ±0.6) Bq/kg
^{60}Co	< 72
^{137}Cs	140±50

Table A.5: Sample: commercial Aluminum foil

Date of measurement: February 2001
Measurement live time: 475.871 h
Sample Mass: 42.2 g

Decay Chain	Element	Activity or upper limit at 95% C.L [mBq/kg]
^{232}Th NOT in equilibrium	^{228}Ra	117 ±11
	^{228}Th	216±16
^{238}U NOT in equilibrium	^{226}Ra	<27.7
	^{234m}Pa	(4.0 ±0.3) Bq/kg
^{235}U		191±3
-	^{40} K	< 85
-	^{60}Co	< 4.4
-	^{137}Cs	9.9±3.7

Table A.6: Sample: 3M reflective foil for $CaWo_4$ detector module

Date of measurement: January 2002

Measurement live time: 774.118 h

Sample Mass: 52 g

Decay Chain	Element	Activity or upper limit at 95% C.L [mBq/kg]
^{232}Th		<11
	^{234}Th	<104
^{238}U	^{234m}Pa	<266
	^{226}Ra	<8
^{235}U		<7
-	^{40} K	76±34
-	^{60}Co	< 5
-	^{137}Cs	4±2

Table A.7: Sample: adhesive foil used to cover lead shield to prevent dust from contaminating the inner copper shielding; new brand

Date of measurement: January 2002
Measurement live time: 774.139 h
Sample Mass: 42 g

Decay Chain	Element	Activity or upper limit at 95% C.L [mBq/kg]
^{232}Th	^{228}Ra	78±13
	^{228}Th	48±10
^{238}U	^{234}Th	0.20±0.07
	^{234m}Pa	0.28±0.17
	^{226}Ra	0.12±0.01
^{235}U		10±3
-	^{40} K	0.60±0.11
-	^{60}Co	< 5
-	^{137}Cs	11±4

Table A.8: Sample: adhesive foil as previous table; old brand

Date of measurement: January 2002
Measurement live time: 833.257 h
Sample Mass: 26.4 g

Decay Chain	Element	Activity or upper limit at 95% C.L [mBq/kg]
^{232}Th	^{228}Ra	78±13
	^{228}Th	48±10
	^{234}Th	0.20±0.07
^{238}U	^{234m}Pa	0.28±0.17
	^{226}Ra	0.12±0.01
^{235}U		10±3
-	^{40} K	0.60±0.11
-	^{60}Co	< 5
-	^{137}Cs	11±4

Table A.9: Sample: CaWO$_4$ crystal

Date of measurement: October 2002
Measurement live time: 403.708 h
Sample Mass: 299.6 g

Decay Chain	Element	Activity or upper limit at 95% C.L [mBq/kg]
^{232}Th	^{228}Ra	<2
	^{228}Th	1.1±0.6
-	^{40} K	<16
^{238}U	^{226}Ra	< (10±3)
	^{234m}Pa	95±42
-	^{60} Co	<1
-	^{137}Cs	<2
-	^{210} Pb	<16 Bq/kg

Bibliography

[Abr02] D. Abrams et al., Exclusion Limits on the WIMP-Nucleon Cross-Section from the Cryogenic Dark Matter Search, *submitted to Phys.Rev.D*

[Alc00] C. Alcock et al., The MACHO Project: Microlensing Results from 5.7 Years of LMC Observations, *Ap. J.* **542** (2000) 281–307

[Ale97] A. Alessandrello et al., The Thermal Detection Efficiency for Recoils Induced by Low Energy Nuclear Reactions, Neutrinos or Weakly Interactive Massive Particles, *Phys. Lett.* **B408** (1997) 465–468

[Ale98] A. Alessandrello et al., Measurements of internal radioactive contamination in samples of Roman lead to be used in experiments on rare events, *Nucl. Instr. and Meth.* **142** (1998) 163–172

[Ang02a] G. Angloher, private communication, 2002

[Ang02b] G. Angloher et al., C. Cozzini, Limits on WIMP Dark Matter using Sapphire Cryogenic Detectors, *Astropart.Phys.* **18** (2002) 43–55

[Arn99] F. Arneodo et al., Neutron Background Measurements in the Hall C of the Gran Sasso Laboratory, *Nuovo Cim.* **A112** (1999) 819–831

[Arp92] C. Arpesella, In *Nuclear Physics B (Proc. Suppl.)*, volume 28A, p. 420, 1992

[Ash76] N. W. Ashcroft, N. D. Mermin, *Solid State Physics*, Holt-Saunders International Editions, 1976

[Bau99] L. Baudis et al., New Limits on Dark Matter WIMPs from the Heidelberg-Moscow Experiment, *Phys. Rev.* **D59** (1999) 022001

[Bel85] E. Bellotti et al., New Measurement of Rock Contaminations and Neutron Activity in the Gran Sasso Tunnel, *INFN/TC-85/19* (1985)

[Ben02] A. Benoit et al., Improved Exclusion Limits from the EDELWEISS WIMP Search, *Phys. Lett.* **B545** (2002) 43–49

[Ber00a] L. Bergström, Non-Baryonic Dark Matter: Observational Evidence and Detection Methods, *Rep. Prog Phys.* **63** (2000) 793–841

[Ber00b] R. Bernabei et al., Search for WIMP Annual Modulation Signature: Results from DAMA, *Phys. Lett.* **B480** (2000) 23–31

[Bet01] A. Bettini, A. Bottino, A. Di Credico, editors, *Topics In Astroparticle And Underground Physics*, volume 110. Nucl. Phys. B (Proc. Suppl.), 2001

[Bet02] A. Bettini, A. Bottino, A. Di Credico, editors, *20th International Conference On Neutrino Physics And Astrophysics (Neutrino 2002).* Nucl. Phys. B (Proc. Suppl.), 2002

[Bot97] A. Bottino et al., Exploring the Supersymmetric Parameter Space by Direct Search for WIMPs, *Phys. Lett.* **B402** (1997) 113

[Büh96] Bühler et al., Status and Low Background Considerations for the CRESST Dark Matter Search, *Nucl. Instr. and Meth.* **A370** (1996) 237

[Bur95] A. Burkert, The structure of Dark Matter Halos in Dwarf Galaxies, *Ap. J.* **447** (1995) L25–L28

[Car94] B.J. Carr, Baryonic Dark Matter, *Ann. Rev. Astron. Astrophys.* **32** (1994) 531–590

[dB02] P. de Bernardis et al., Multiple peaks in the Angular Power Spectrum of the Cosmic Microwave Background: Significance and Consequences for cosmology, *Ap. J.* **564** (2002) 559–566

[dGS] Laboratori Nazional del Gran Sasso, http://www.lngs.infn.it

[Dol99] A.D. Dolgov, Dark Matter in the Universe, *Preprint* hep–ph/9910532

[Don] J. Dončev, PhD thesis, Technische Universität München, in preparation

[Don98] F. Donato, N. Fornengo, S. Scopel, Effects of Galactic Dark Halo Rotation on WIMP Direct Detection, *Astropart. Phys.* **9** (1998) 247–260

[Eis87] M. Eisenbud, *Environmental Radioactivity*, Academic Press, Inc., 3. Edition, 1987

[Ell97] J. Ellis, K. A. Olive, M. Schmitt, Constrains on Neutralino Dark Matter from LEP 2 and Cosmology., *Phys. Lett.* **B413** (1997) 355

[Eng91] J Engel, Nuclear Form Factors for the Scattering of WIMPs, *Physics Letters B* **264** (1991) 114–119

[Eng92] J Engel, Nuclear Form Factors for the Scattering of Neutralinos, *Nucl. Physics B (Proc. Suppl.)* **28A** (1992) 310–313

[FF00] E. Figueroa-Feliciano et al., Optimal Filter Analysis of Energy Dependent Pulse Shapes and its Application to TES Detectors, *Nucl. Instr. and Meth.* **A 444** (2000) 453

[For02] N. Fornengo, Candidates for Non-Baryonic Dark Matter, *Preprint* **hep-ph/0201156 v2** (2002)

[Fra02] T. Frank, *Development of Scintillating Calorimeters for Discrimination of Nuclear Recoils and Fully Ionizing Events*, PhD thesis, Technische Universität München, 2002

[Fre88] K. Freese, J. Frieman, A. Gould, Signal Modulation in Cold Dark Matter Detection., *Phys. Rev.* **D 37** (1988) 3388

[Fre99] W.L Freedman, Determination of Cosmological Parameters, *Preprint* astro-ph/9905222

[Gab96] A. Gabutti, M. Olechowski, S. Cooper, S. Pokorski, L. Stodolski, Light neutralinos, *Astropart. Phys.* **6** (1996) 1

[Gai90] T. K. Gaisser, *Cosmic Rays and Particle Physics*, Cambridge University Press, 1990

[Gat86] E. Gatti, P. F. Manfredi, Processing the Signals from Solid-State Detctors in Elementary -Particle Physics, *Riv.Nuovo Cim.* **9N1** (1986) 1–146

[GB99a] J. Garcia-Bellido, Astrophysics and Cosmology, *Casta-Papiernicka 1999, High-energy physics* **ESHEP 99** (1999) 109–186

[GB99b] J. Garcia-Bellido, The Origin of Matter and Structure in the Universe, *Phil.Trans.Roy.Soc.Lond.* **A357** (1999) 3237–3257

[Glu73] M. Gluyas, F. D. Huges, B.W. James, The Elastic Constants of Calcium Tungstate, *J. Phys. D: Appl. Phys.* **6** (1973) 2025–2037

[Gre02] A. M. Green, Calculating Exclusion Limits for WIMP Direct Detection Experiments without Background Subtraction, *Phys. Rev.* **D65** (2002) 023520

[Gro00] D. E. Groom et al., Global Cosmological Parameters: H_0, Ω_M, and Λ., *European Physical Journal* **C 15** (2000) 1

[Heu95] G. Heusser, Low Radioactivity Background Techniques, *Ann. Rev. Nucl. Part. Sci.* **45** (1995) 543

[IEE86] IEEE Nuclear and Plasma Sciences Society, Test Procedures for Germanium Gamma Ray Detectors, ANSI/IEEE Std 325–1986, Institute of Electrical and Electronics Engineers, New York, 1986

[Jun96] G. Jungman, M. Kamionkowski, K. Griest, Supersymmetric Dark Matter, *Phys. Rep.* **267** (1996) 195

[Kam98] M. Kamionkowski, A. Kinkhabwala, Galactic Halo Models and Particle Dark-Matter Detection, *Phys. Rev. D* **57** (1998) 3256

[Kha02] S. Khalil, C. Munoz, The Enigma of the Dark Matter, *Contemp. Phys.* **43** (2002) 51–62

[LBN] USA LBNL, Berkeley, Sweden Lund University, The Lund/LBNL Nuclear Data Search, http://nucleardata.nuclear.lu.se/nucleardata/toi/

[Lew96] J. D. Lewin, P. F. Smith, Review of Mathematics, Numerical Factors, and Corrections for Dark Matter Experiments based on Elastic Nuclear Recoil, *Astropart. Phys.* **6** (1996) 87

[Loi99] M. Loidl, *Diffusion und Einfang von Quasiteilchen*, PhD thesis, Ludwig-Maximilians-Universität München, 1999

[Loi02] M. Loidl, Experimental Particle Dark Matter Search, *Preprint* astro-ph/0207308

[Mar00] J. Marchese, *Background Studies for the CRESST Dark Matter Search*, PhD thesis, University of Oxford, 2000

[Mei99] O.J. Meier, *Aktives thermisches Feedback für massive Tieftemperaturdetektoren*, PhD thesis, Technische Universität München, 1999

[Meu99] P. Meunier et al., Discrimination between Nuclear Recoils and Electron Recoils by Simultaneous Detection of Phonons and Scintillation Light, *Appl. Phys. Lett.* **75(9)** (1999) 1335

[Mil83] M. Milgrom, A Modification of the Newtonian Dynamics as a Possible Alternative to the Hidden Mass Hypothesis, *Ap. J.* **270** (1983) 365–370

[Mor01] A. Morales, In *Nuclear Physics B (Proc. Suppl.)*, volume 110, pp. 39–54, 2001

[Nav96] J.F. Navarro et al., The Structure of Cold Dark Matter Halos, *Ap. J.* **462** (1996) 563–575

[Oli97] K.A Olive, Primordial Nucleosynthesis and Dark Matter, *Preprint* **astro-ph/9707212** (1997)

[Pac96] B. Paczynski, Gravitational Microlensing in the Local Group, *Ann. Rev. Astron. Astrophys.* **34** (1996) 419–460

[Pet] F. Petricca, PhD thesis, Ludwig-Maximilians-Universität München, in preparation

[Pre93] H. W. Press et al., *Numerical Recipes in C: the Art of Scientific Computing*, Cambridge University Press, Cambridge, 2. Edition, 1993

[Pri96] J.R. Primack, In A. Deckel, J. P. Ostriker, editors, *Formation of Structure in the Universe*, p. 1, Proceedings of Jerusalem Winter School, 1996. Cambridge University Press

[Pri97] J.R. Primack, In H.V. Klapdor–Kleingrothaus, Y. Ramachers, editors, *Dark Matter in Astro– and Particle Physics*, p. 127, Singapore, 1997. World Scientific Publ.

[Pri00] J.R. Primack, Cosmological Parameters, *Nuclear Physics B (Proc. Suppl.)* **87** (2000) 3–12

[Prö95] F. Pröbst et al., Model for Cryogenic Particle Detectors with Superconducting Phase Transition Thermometers, *J. of Low Temp. Phys.* **100** (1995) 69

[Raf97] G.G. Raffelt, Dark Matter: Motivations, Candidates and Searches, *Preprint* hep-ph/9712538

[Raf00] G.G. Raffelt, Axions and other very light Bosons, *Eur.Phys.J.* **C** (2000) 298–305

[Ram99] Y. Ramachers, Non-Baryonic Dark Matter Searches, *Preprint* astro–ph9911260

[Ram00] Y. Ramachers, Background Considerations for CRESST: Cosmic Activation, 2000, CRESST Internal Preprint

[Ram01a] Ramachers, 2001, private communication

[Ram01b] Y. Ramachers, Dark Matter, *Europhys.News* **32** (2001) 242–244

[Ram02a] Y Ramachers, Modulation analysis methods for WIMP direct detection, *Astropart. Phys.*, accepted for publication

[Ram02b] Y. Ramachers, In *Nuclear Physics B (Proc. Suppl.)*, 2002, to appear

[Ros00] L. Roszkowski, In *Nuclear Physics B (Proc. Suppl.)*, volume 87, pp. 21–30, 2000

[RR93] M. Rowan-Robinson, *Cosmology*, Oxford University Press, Oxford, 3. Edition, 1993

[Sad99] B. Sadoulet, Deciphering the nature of dark matter., *Rev. Mod. Phys.* **71** (1999) 2

[San96] R. Sanders, The Published Extended Rotation Curves of Spiral Galaxies: Confrontation with Modified Dynamics, *Ap. J.* **473** (1996) 117

[Sch97] S. Schindler, Ω_m - Different Ways to determine the Matter Density of the Universe, *Preprint* **astro-ph/9707212** (1997)

[Sis99] M. Sisti, *CRESST – a Cryogenic Experiment for Dark Matter Search*, PhD thesis, Ludwig-Maximilians-Universität München, 1999

[Smi90] P. F. Smith, J. D. Lewin, Dark Matter Detection, *Phys. Rep.* **187 No. 5** (1990) 203–280

[Spi00] M. Spiro, E. Aubourg, N. Palanque-Delabrouille, Search for Galactic Dark Matter, *Physica Scripta* **T85** (2000) 254–258

[Spo02a] N. Spooner, In *Proc. School on Neutrino Particle Astrophysics, Les Houches, France.*, 2002, to appear

[Spo02b] N.J.C. Spooner, editor, *4th International Workshop On The Identification Of Dark Matter.* World Scientific Ltd., 2002

[Sta] M. Stark, PhD thesis, Technische Universität München, in preparation

[The96] P. Theodorson, *Measurement of Weak Radioactivity*, World Scientific, 1996

[Tov00] D.R. Tovey et al., A New Model Independent Method for Extracting Spin-Dependent (Cross Section) Limits from Dark Matter Searches, *Physics Letters B* **488** (2000) 17–26

[Tur00a] M.S. Turner, Dark matter and Energy in the Universe, *Physica Scripta* **T85** (2000) 210–220

[Tur00b] M.S. Turner, The Dark Side of the Universe: from Zwicky to Accelerated Expansion, *Physics Reports* **333-334** (2000) 619–635

[Whi95] D.A. White, Fabian A.C., Einstein Observatory Evidence for the Widespread Baryon Overdensity in Clusters of Galaxies, *Mon. Not. R. Astron. Soc.* **273** (1995) 72–84

Acknowledgments

I thank Prof. Dr. Walter Blum for giving me the possibility to accomplish this work within CRESST group at Max Planck Institut für Physik in Munich.

I am specially grateful to Dr. Franz Pröbst who constantly supported and supervised this work. I benefited greatly from his in-depth knowledge of physics, his intuition and his enormous experience in research. From him I (hopefully) learned to work in a scientific rigorous way. The opportunity he gave me to work in Gran Sasso at the experimental site was invaluable and opened my eyes to scientific research. I also cannot thank him enough for always taking time for answering any question, even though he was overwhelmed by work. Dafür herzlichen Dank.

Dr. Wolfang Seidel, the Oxford and MPI technicians who made CRESST move from Hall B to Hall A possible, deserve a special thank. Thank to their precious and huge effort, the cryostat worked at the very first cool-down after the move. Without them no Phase II measurements would have taken place yet.

Vielen Dank to all the members of the Cryodetector Group at MPI in Munich. Besides the lively and stimulating atmosphere within the scientific work, they were all very friendly far beyond a mere working situation. First of all, I would like to thank my favourite officemate Dr. Torsten Frank. Besides being favourite he is also my only officemate, but this is just a detail :-). He rendered my stay here in Munich in and outside the institute very pleasant and was always available to show around the Munich Kneipe whenever any friend of mine came for visit. Therefore he also has the honorific charge of *local organising committee* which he always covered with “spontaneous enthusiasm”. So, thank you Torsten. Actually he wanted two full pages of thanks just for him, but he did not pay me enough!! Special thanks also to Dr. Gode Angloher who guided me into the secrets of Bavarian culture. I will never forget when he introduced me to König Ludwig. Some people may think that he drawn some time ago in a lake, but no!, he is safe and sound and sings “Griechscher Wein” with full voice in the most characteristic Stüberl of Munich. Dr. Peter Christ I thank for sharing with us his passion for music which I enjoyed at his concerts. Stefan Rutzinger for preparing nice italian coffee, turning my slow motion in some effective work. Mr. Antonio Bento I thank 66 times. Why? Well this is a little “secret” within our group! Hans Seitz I thank for always practising his perfect Italian and his cooking abilities bringing often nice cakes. By the way, he was not the only practising on this. Thank also to Jelena Doncev, Federica Petricca and again Peter for the delicious cakes. I could not decide so far who was the best... could you please have another try?? So brsvztxw Jelena (this means: “thank you for the cake, it was really good” in her special language without vowels) e grazie a Federica also for the nice, though tuff, time during Gran Sasso shifts and her moral support during writing. Thanks also to Sergey Uchaikin for having always some funny tales, Dieter Hauff, Dr. Leo Stodlosky for the interesting discussions and all the MPI group. Thank you.

Mille grazie also to all the Assergiti and friends in Gran Sasso: Alba, Elisa, George, Laslo, Nicola, Matthias J., Mariaelena, Paolo... Thanks also to Carlo Bucci for his support in Gran Sasso and Dr. Matthias Laubenstein for performing the radioactivity measurements on Germanium detectors. Special thanks also to Dr. Yorck Ramachers. He constantly gave me precious support and advice on this work (e non solo :-)), transmitting me his remarkable enthusiasm for the Dark Matter field. His constant presence at the Gran Sasso site and his endeavour to run the experiment made all this measurements possible. Grazie.

Finally I would like to thank the whole Oxford group, in particular Dr. James Marchese. I benefited a lot from his background studies for CRESST.

Last but not least I would like to thank my family, my friends in Italy, especially Paola and Daniela, and my friends here in Munich especially Valeria, Johaness and Ana. All of them gave me support and nice time. Grazie a tutti.